

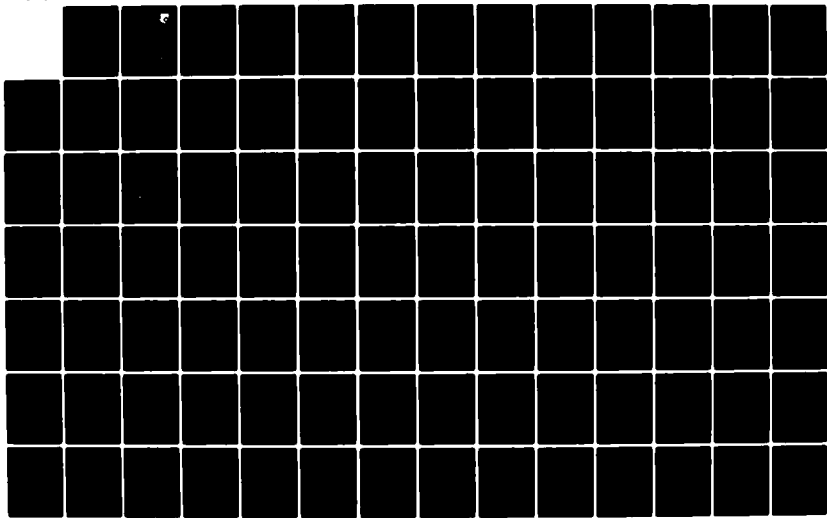
AD-A128 417

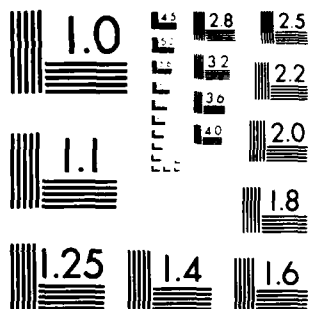
LUMINESCENCE AND ELECTRICAL CHARACTERIZATION OF ION  
IMPLANTED Si:TL(U) AIR FORCE INST OF TECH  
WRIGHT-PATTERSON AFB OH SCHOOL OF ENGI... O F SWENSON  
NOV 82 AFIT/DS/PH/82-1 AFWAL-TR-82-4115 F/G 20/12

1/3

UNCLASSIFIED

NL





MICROCOPY RESOLUTION TEST CHART  
NATIONAL BUREAU OF STANDARDS 1963-A

AFWAL-TR-82-4115

5

AD A128416



LUMINESCENCE AND ELECTRICAL CHARACTERIZATION OF ION IMPLANTED SI:TL

Orven F. Swenson, Captain

November 1982

Final Report for Period January 1980 - January 1982.

*Superseded  
AD-A118120*

Approved for public release; distribution unlimited.

DTIC FILE COPY

DTIC  
ELECTE  
MAY 20 1983  
S B D

MATERIALS LABORATORY  
AIR FORCE WRIGHT AERONAUTICAL LABORATORIES  
AIR FORCE SYSTEMS COMMAND  
WRIGHT-PATTERSON AIR FORCE BASE, OHIO 45433

83 05 19 202

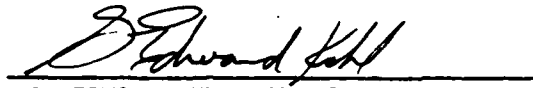
NOTICE

When Government drawings, specifications, or other data are used for any purpose other than in connection with a definitely related Government procurement operation, the United States Government thereby incurs no responsibility nor any obligation whatsoever; and the fact that the government may have formulated, furnished, or in any way supplied the said drawings, specifications, or other data, is not to be regarded by implication or otherwise as in any manner licensing the holder or any other person or corporation, or conveying any rights or permission to manufacture use, or sell any patented invention that may in any way be related thereto.

This report has been reviewed by the Office of Public Affairs (ASD/PA) and is releasable to the National Technical Information Service (NTIS). At NTIS, it will be available to the general public, including foreign nations.

This technical report has been reviewed and is approved for publication.

  
PATRICK M. HEMENGER  
Project Monitor

  
G. EDWARD KUHL, Chief  
Laser & Optical Materials Branch  
Electromagnetic Materials Division

FOR THE COMMANDER

  
MERRILL L. MINGES, Chief  
Electromagnetic Materials Division  
Materials Laboratory  
AF Wright Aeronautical Laboratories

"If your address has changed, if you wish to be removed from our mailing list, or if the addressee is no longer employed by your organization please notify AFWAL/MLPO, W-PAFB, OH 45433 to help us maintain a current mailing list".

Copies of this report should not be returned unless return is required by security considerations, contractual obligations, or notice on a specific document.

UNCLASSIFIED

SECURITY CLASSIFICATION OF THIS PAGE (When Data Entered)

REPORT DOCUMENTATION PAGE		READ INSTRUCTIONS BEFORE COMPLETING FORM
1. REPORT NUMBER AFWAL-TR-82-4115	2. GOVT ACCESSION NO. AD A128417	3. RECIPIENT'S CATALOG NUMBER
4. TITLE (and Subtitle) LUMINESCENCE AND ELECTRICAL CHARACTERIZATION OF ION IMPLANTED SI:TL	5. TYPE OF REPORT & PERIOD COVERED Final January 1980 - January 1982	
	6. PERFORMING ORG. REPORT NUMBER AFIT/DS/PH/82-1	
7. AUTHOR(s) Orven F. Swenson, Captain	8. CONTRACT OR GRANT NUMBER(s)	
9. PERFORMING ORGANIZATION NAME AND ADDRESS Air Force Institute of Technology (AFIT-EN) Wright-Patterson AFB, Ohio 45433	10. PROGRAM ELEMENT, PROJECT, TASK AREA & WORK UNIT NUMBERS 2306Q106	
11. CONTROLLING OFFICE NAME AND ADDRESS Materials Laboratory (AFWAL/MLPO) Air Force Wright Aeronautical Laboratories (AFSC) Wright-Patterson AFB, Ohio 45433	12. REPORT DATE November 1982	
	13. NUMBER OF PAGES 137	
14. MONITORING AGENCY NAME & ADDRESS (if different from Controlling Office)	15. SECURITY CLASS. (of this report) Unclassified	
	15a. DECLASSIFICATION, DOWNGRADING SCHEDULE	
16. DISTRIBUTION STATEMENT (of this Report)  Approved for public release; distribution unlimited.		
17. DISTRIBUTION STATEMENT (of the abstract entered in Block 20, if different from Report)		
18. SUPPLEMENTARY NOTES  Approved for public release, IAW AFR 190-17.		
19. KEY WORDS (Continue on reverse side if necessary and identify by block number)		
Ion Implants	Luminescence	Defects
Silicon	Hall-Effect	Anneal
Thallium	Rutherford Backscattering (RBS)	Bound Exciton
Si:Tl	Secondary Ion Mass Spectrometry (SIMS)	
Mobility	Ionization Energy	
20. ABSTRACT (Continue on reverse side if necessary and identify by block number)		
<p>Ion implanted Si:Tl was characterized by luminescence, Hall-effect, Rutherford Backscattering (RBS), and Secondary Ion Mass Spectrometry (SIMS). This is the first reported luminescence study of an implanted dopant in silicon. The same sharp line defects were produced by the Tl heavy ion implants as identified in previous light ion studies. The defects produced by the ion implantation were removed and the Tl activated by a two-step anneal procedure. A high quality annealed implant layer was produced from which the</p> <p style="text-align: right;">(continued on back)</p>		

DD FORM 1 JAN 73 1473 EDITION OF 1 NOV 68 IS OBSOLETE

UNCLASSIFIED

SECURITY CLASSIFICATION OF THIS PAGE (When Data Entered)

UNCLASSIFIED

SECURITY CLASSIFICATION OF THIS PAGE (When Data Entered)

four excited states of the Tl bound exciton no-phonon could be resolved. An unidentified bound exciton peak related to the Tl acceptor was observed for the first time in both ion implanted and bulk grown Si:Tl. Temperature dependent Hall-effect measurements were made on the implant layers which indicate that Hall-effect measurements made only at room temperature are not valid in general for silicon implant layers. The Hall data and luminescence data both indicate that the concentration of activated Tl increases with increasing second anneal temperature. The Hall-mobility varied as  $T^{-2.4}$  for implanted Si:Tl in the temperature range 135-165 K. The ionization energy was determined to be 229 meV by Hall-effect measurements in the compensated temperature region. ←

UNCLASSIFIED

SECURITY CLASSIFICATION OF THIS PAGE (When Data Entered)

FOREWORD

This report was prepared by Captain Orven F. Swenson. The work was performed in support of WUD No. 48, "Electro-Optical Materials," and JON 2306Q106.

This report was submitted as the thesis requirement for the Degree of Doctor of Philosophy to the School of Engineering of the Air Force Institute of Technology and was published as AFIT report AFIT/DS/PH/82-1.

The author thanks the members of the Materials Laboratory who supported this study and Dr. P. M. Hemenger for the use of his Hall-effect apparatus and for his encouragement and insight throughout the effort.

He acknowledges Dr. R. G. Wilson of Hughes Research Laboratories for ion implanting the Si:Ti and providing the SIMS data. Dr. G. Carter, Dr. C. E. Christodoulides, and Dr. A. Ali of the University of Salford, Salford, England, are also acknowledged for providing the RBS data.

The author is also indebted to Dr. T. E. Luke for his encouragement and guidance during the completion of this study and to Dr. R. L. Hengehold for supporting the research effort.

DSIC  
COPY  
REPRODUCTION

Accession #	
AFIS	✓
AFIC	
AFIC	
AFIC	
By	
Distribution	
Available to	
Dist	Special
A	

## TABLE OF CONTENTS

SECTION	PAGE	
I	INTRODUCTION	1
	1. Objective of the Research	2
	2. Overview of the Research	2
II	BACKGROUND	4
	1. Ion Implantation	4
	a. Range Distribution	4
	b. Radiation Damage	7
	c. Implant Damage Annealing	8
	2. Sample Preparation for this Research	9
	a. Sample Implantation	9
	b. Two-step Annealing	9
	c. Sample Cleaning and Cutting	12
	d. Electrical Measurement Samples	13
	e. Bulk Doped Reference Samples	13
III	LUMINESCENCE	15
	1. Silicon Luminescence	15
	a. Luminescent Mechanisms	15
	b. Previous Results for Si:Tl	19
	2. Luminescence System	19
	3. Reference Luminescence Results	22
	a. Substrate Luminescence	22
	b. Bulk Doped Si:Tl Luminescence	22
	4. Implanted Si:Tl Luminescence	30
	a. Unannealed Implanted Samples	30
	b. Two-step Annealed Samples	35
	c. Tl BE Luminescence in Implanted Si	44
	d. BE Excited States	48
	5. Comparison with Previous Studies	48

## TABLE OF CONTENTS (Cont'd)

SECTION	PAGE
IV ELECTRICAL MEASUREMENTS	52
1. Surface Hall Effect Measurements	52
a. The van der Pauw Technique	52
b. The Reverse-Biased p-n Junction	57
c. Measurements as a Function of Temperature	60
d. Previous Electrical Measurements	65
2. The van der Pauw System	68
3. Hall-effect Results	68
a. Substrate Donor Concentration	68
b. Figures of Merit	69
c. Sheet Hole Concentration	76
d. Hall Mobility	81
e. Ionization Energy	81
4. Comparison with Previous Studies	89
a. Ionization Energy of Ion Implanted Silicon	90
b. Electrical Measurements on Si:Tl	92
V RBS AND SIMS	93
1. Rutherford Backscattering and Channeling	93
a. Depth Sensitivity	94
b. Lattice Disorder	97
c. Impurity Atom Detection	100
d. Previous RBS Studies of Si:Tl	102
e. RBS Results	104
2. Secondary Ion Mass Spectrometry	110
VI CONCLUSIONS	113
VII RECOMMENDATIONS	117
1. Implanted Si:Tl	117
2. Implant Technique	118
REFERENCES	119

## LIST OF ILLUSTRATIONS

FIGURE		PAGE
1.	Projected Range	5
2.	Beam Channeling when the Incident Beam is Parallel to a Major Crystallographic Direction	5
3.	Van der Pauw Pattern	14
4.	Photoluminescence from 70 Ohm-cm Silicon Substrate Material at 10 and 15 K	17
5.	Schematic Diagram of Luminescence System	20
6.	System Response to a Blackbody Radiator at 1050 K and the Corresponding Correction Factor	23
7.	Photoluminescence of the Silicon Substrate at Temperatures from 10 K to 30 K	24
8.	Photoluminescence Spectrum of Bulk Grown Si:Tl	25
9.	Photoluminescence Spectra of the Tl BE Taken at Temperatures from 10 K to 30 K	27
10.	Photoluminescence Spectra of Tl BE at 10 K and Excitation Powers Ranging from 251 mW to 29 mW	28
11.	Comparison of Photoluminescence Associated with Isoelectronic BE and with the Tl BE	29
12.	Photoluminescence Spectra of the Isoelectronic BE Taken at Temperatures from 15 K to 60 K	31
13.	Photoluminescence Spectra of the Isoelectronic BE for Excitation Powers Ranging from 297 mW to 29 mW	32
14.	High and Low Resolution Cathodoluminescence of Unannealed Implanted Si:Tl at 24 K	33
15.	Temperature Dependent Cathodoluminescence of Unannealed Implanted Si:Tl	36
16.	Cathodoluminescence from Laser Annealed Si and Unannealed Implanted Si:Tl	37
17.	Photoluminescence from Ion Implanted Si:Tl at 15 K and 30 K after a 550°C Anneal	38

## LIST OF ILLUSTRATIONS (Cont'd)

FIGURES		PAGE
18.	Photoluminescence from Ion Implanted Si:Tl at 30 K after Anneals at 550°C, 550°C + 650°C, 550°C + 750°C, and 550°C + 950°C	39
19.	Photoluminescence from Ion Implanted Si:Tl at 15 K and 30 K Showing the BE(NP): FE(TO) Ratios as a Function of Second Anneal Temperature	41
20.	Cathodoluminescence from Single-Step 850°C Annealed Si:Tl for a Focused and Defocused Beam	42
21.	Cathodoluminescence from Single-Step 950°C Annealed Si:Tl for Two Positions and With the Beam Defocused	43
22.	Photoluminescence Spectra of Fully Annealed Silicon Ion Implanted with $10^{14}$ Tl Ions/cm <sup>2</sup> at 560 keV	45
23.	High Resolution Luminescence Spectrum Taken at 10 K of Annealed Silicon Ion Implanted with $10^{14}$ Ions/cm <sup>2</sup> at 560 keV	46
24.	Thallium Associated Luminescence at 15 K from Ion Implanted Silicon. The FE Spectrum of Figure 7 Has Been Subtracted from the Combined FE and BE Spectrum of Figure 24	47
25.	High Resolution Spectra of the BE(NP) Line in Ion Implanted Si:Tl Showing Four Thermalizing Lines	49
26.	Configurations Used for van der Pauw Measurements	53
27.	Electrical Connections for a Reverse-biased Implant Layer	59
28.	Computer Plots Generated Using Equation 23 and Equation 24	63
29.	Carrier Concentration of the Substrate Including the Charge Balance Equation Fit, Solid Line	70
30.	Leakage Current Percent and $R_a/R_b$ Values for a Good Sample	72
31.	Leakage Current Percent and $R_a/R_b$ Values for a Leaky Sample	73
32.	Leakage Current for a Good Sample	74
33.	Leakage Current for a Leaky Sample	75

FIGURE	LIST OF ILLUSTRATIONS (Cont'd)	PAGE
34.	Sheet Carrier Concentration Versus Inverse Temperature for a Good Sample	77
35.	Sheet Carrier Concentration Versus Inverse Temperature for a Leaky Sample	78
36.	Sheet Carrier Concentration Variations with Second Anneal Temperature	79
37.	Sheet Carrier Concentration at 200 K as a Function of Inverse Second Anneal Temperature	80
38.	Sheet Carrier Concentration Variations with Dose and Implant Energy	82
39.	Hall Mobility Temperature Dependence	83
40.	Conductivity Mobility Temperature Dependence	84
41.	Fit of the Sheet Carrier Concentration in the Compensated Temperature Region	86
42.	Sheet Conductivity Temperature Dependence	88
43.	Typical Backscatter Yields in Silicon	95
44.	Typical RBS Configuration	96
45.	Glancing Angle, High Resolution RBS Configuration	98
46.	The {110} Plane of Silicon Showing the Locations Seen by a Channeled Probe Beam Along the Major Crystalline Directions $\langle 110 \rangle$ , $\langle 111 \rangle$ , and $\langle 100 \rangle$	101
47.	Low Angle Exit Aligned $\langle 100 \rangle$ RBS Spectra from (100) Silicon Implanted with $1 \times 10^{14}$ Tl/cm <sup>2</sup> at 280 keV	105
48.	Aligned $\langle 100 \rangle$ RBS Spectra from (100) Silicon Samples Implanted with $1 \times 10^{14}$ Tl/cm <sup>2</sup> at 280 keV and then Annealed	107
49.	Low Angle Exit Aligned $\langle 100 \rangle$ RBS Spectra from (100) Silicon Samples Implanted with $1 \times 10^{14}$ Tl/cm <sup>2</sup> at 280 keV and then Annealed	109

LIST OF ILLUSTRATIONS (Concluded)

FIGURE		PAGE
50.	SIMS Depth Profile from Unannealed Silicon Implanted with $4.0 \times 10^{13}$ T1/cm <sup>2</sup>	111
51.	SIMS Depth Profile from (111) Silicon Implanted with $4.0 \times 10^{13}$ T1/cm <sup>2</sup> and then Annealed at 800°C for 20 Min	112

## LIST OF TABLES

TABLE		PAGE
1	Samples Used in This Study	10
2	Energies of the T1 Associated Luminescence Lines	26
3	Defect Luminescence	34
4	Substrate Concentrations	69
5	$R_a/R_b$ Ratios and Mobility Temperature Dependence	85
6	Ionization Energies	87
7	Ionization Energies Determined for Implants	90
8	RBS Results	108

## SECTION I

## INTRODUCTION

Extrinsic silicon has recently received renewed interest as an infrared detector material for Air Force applications. This is the result of a desire for arrays of detectors of a material which allows the incorporation of the signal processing electronics on the detector chip. Such a material would avoid the requirement for separate detectors and electronics and for the interconnects between them. The existence of a highly developed technology for the fabrication of integrated electronics on silicon is the main point in favor of using silicon for these detector arrays. For this application, a silicon dopant is required which is photosensitive within the desired spectral range, has a sufficiently high quantum efficiency, and permits the highest possible temperature for photon background limited operation.

Thallium provides a near ideal match to the 3-5 micron spectral window in the atmospheric absorption (Reference 1). Also, thallium has a high theoretical detectivity, a high theoretical background-limited operating temperature (90 K), and a low diffusion coefficient compared to the 30 other dopants in silicon screened by Sclar for possible use in the 3-5 micron range. Its only identified drawback is that for doping techniques attempted so far the thallium solubility in silicon is limited to the  $10^{15}$  -  $10^{16}$   $\text{cm}^{-3}$  range (Reference 1).

Interest in thallium doped silicon (Si:Tl) has been minimal due to the low Tl solubility,  $3.7 \times 10^{17}$   $\text{cm}^{-3}$  at 1105°C (Reference 2). This low solubility has made optical measurements difficult and has resulted in Tl being the least optically studied group IIIA impurity in silicon (Reference 3). Also, the low concentration of acceptors attainable has resulted in very high resistivity which has hindered electrical measurements. Because of its high potential, further research was needed to determine the suitability of Si:Tl as a detector material. Ion implantation provided an alternative to the largely unsuccessful conventional techniques of growing appropriately doped Si:Tl.

## 1. OBJECTIVE OF THE RESEARCH

The purpose of this research was to investigate the properties of ion implanted Si:Tl for application as a detector material in the 3-5 micron spectral range. The important parameters considered were the concentration of electrically active thallium impurities, the mobility of the doped material, the ionization energy of the acceptor, and the optically active concentration of Tl. In order to fully characterize Si:Tl, these properties were measured for various Tl concentrations and annealing parameters.

Prior electrical and optical measurements had been made on melt-grown (Reference 4-7) and diffused (References 3 and 4) Si:Tl material. These techniques have the disadvantage that only very low concentrations of Tl can be introduced into silicon, less than  $5 \times 10^{16} \text{ cm}^{-3}$  to date. Also, the final Tl concentration is difficult to control by these methods and the concentration of Tl cannot be varied from wafer to wafer by the melt-growth technique. However, an efficient method by which to introduce precisely determined amounts of impurities into a material is ion implantation (Reference 8). This technique permits the selection of the impurity concentration to be studied for each silicon wafer and also produces higher impurity concentrations than are available by other doping techniques. Therefore, ion implantation was selected as the primary method of preparing samples for this research. The theory of ion implantation and the specifics of the sample preparation are given in Section II.

## 2. OVERVIEW OF THE RESEARCH

Luminescence was used to monitor the defects introduced by the implantation and the optical activation of the Tl dopant. Luminescence has not been previously used to study implanted dopants in Si. It turns out to be an ideal method for this since the annealing of defects introduced by the implantation can be studied at the same time as the optical activation of the dopant. The defects introduced were found to be the same as in previous work implanting light ions. A new Tl related peak was discovered in the Tl bound exciton spectrum. This was confirmed by

luminescence from a bulk grown Si:Tl sample. The results of these measurements are presented and discussed in Section III.

The electrical properties of Si:Tl were determined using the van der Pauw technique for Hall-effect measurements. Since the electrical characteristics vary with depth, this has not been a very effective method for studying implant layers. However, this study shows that the ionization energy and mobility can be determined for implant layers by making temperature dependent measurements in compensated temperature regions. The implant layer was electrically isolated from the substrate by a p-n junction formed by implanting p-type into n-type Si. It is shown that the leakage current through the p-n junction formed by the implant layer and the  $R_a/R_b$  ratios should be monitored when using this technique. The sheet carrier concentration was used to qualitatively evaluate the effects of sample orientation, energy of the implant, and thermal anneal temperatures. The first Si:Tl ionization energy and mobility results determined from Hall-effect measurement of ion implanted layers are reported. Hall-effect theory and results are given in Section IV.

Rutherford Backscattering (RBS) and Secondary Ion Mass Spectrometry (SIMS) results are included in Section V. They confirm that Tl is contained in the regrown Si after annealing and that the disorder created by implantation is nearly all removed.

## SECTION II

## BACKGROUND

## 1. ION IMPLANTATION

Ion implantation is a method of selectively introducing atoms into the surface layer of a solid by bombardment with energetic ions (References 8 and 9). Since the number of implanted ions is controlled by the implant system rather than the physical properties of the substrate, species can be studied which cannot be introduced into semiconductors by conventional means such as diffusion. The important parameters for implanted semiconductors are the range distribution of the implanted atoms, the amount and nature of the lattice disorder created, the lattice location of the implanted atoms and ultimately the electrical characteristics of the implant layer after subsequent annealing (Reference 8).

## a. Range Distribution

The position where an implanted ion comes to rest is a function of its energy on impact. The total distance it travels through a solid is called its "range" and the projection of this distance onto the direction of incidence is called (Reference 9) the "projected range" (see Figure 1).

When the impinging ion is aligned with a major crystallographic direction (typically (111), (110), or (100)) it sees an open "channel" in the lattice (see Figure 2). Since it suffers only minor glancing collisions as it travels down the channel, it will penetrate much farther into the crystal than an ion incident along a random direction. By purposely misaligning the beam from the major crystallographic directions, the ion beam will see a nearly random target. This was the case for all samples used in this study. For this case with no channeling, the range distribution is roughly Gaussian and can be characterized by a mean projected range  $R_p$  and a standard deviation  $\Delta R_p$  from this mean (Reference 8).

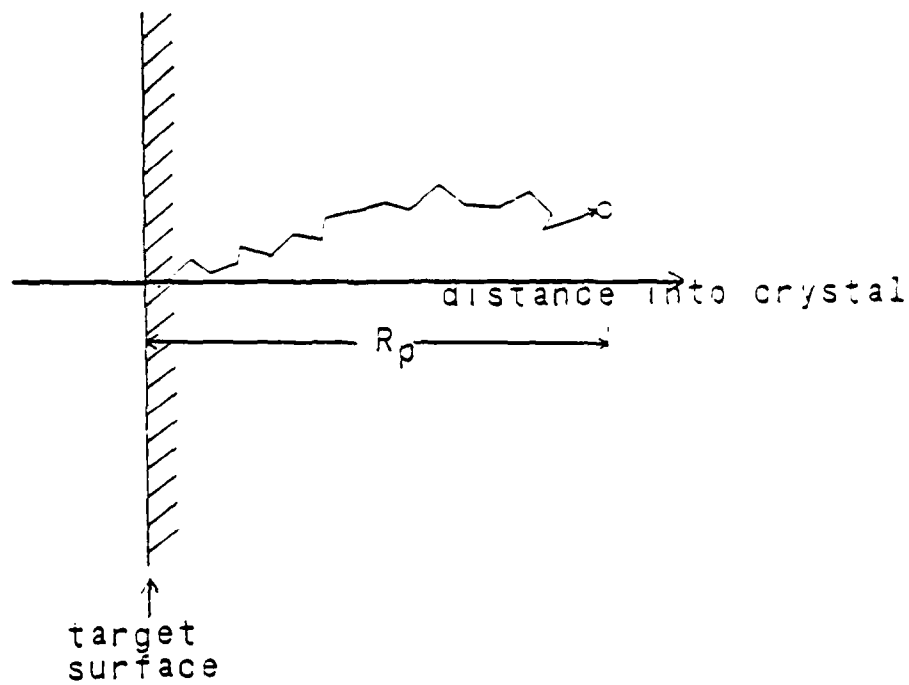


Figure 1. Projected Range

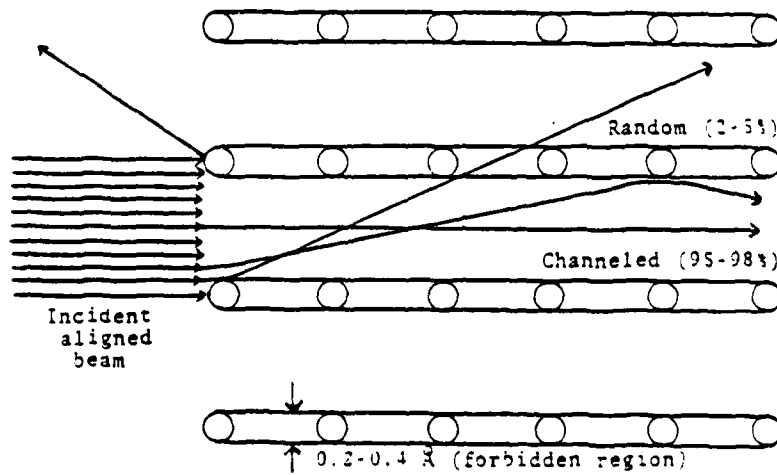


Figure 2. Beam Channeling when the Incident Beam is Parallel to a Major Crystallographic Direction

The concentration of impurities as a function of depth will then be given approximately by

$$N(x) = \frac{N_i}{\sqrt{2\pi} \Delta R_p} \exp\left[-\frac{(x - R_p)^2}{2(\Delta R_p)^2}\right] \quad (1)$$

where  $N_i$  is the implant dose (ions/cm<sup>2</sup>). The peak concentration  $N_{\max}$  of the implanted species can be estimated by (Reference 9).

$$N_{\max} \approx \frac{0.4 N_i}{\Delta R_p} \quad (2)$$

In practice, it is nearly impossible to avoid all effects of channeling in a crystalline in a crystalline target, because atoms entering in a random direction can be deflected into a channeled direction. These few "channeled" atoms form a deep "tail" beyond  $R_p$  and become important when considering the electrical characteristics of the implant layer. For example, the electrical characteristics of the implanted p-n junction are determined by the implantation profile in the region where the dopant concentration is comparable to the background level in the substrate (Reference 8). If the p-n junction occurs in the tail region, then rather than being abrupt as desired, the junction will be extended and will be adjoined by high resistivity regions on both sides which will strongly influence the electrical characteristics as shown in Section IV.

Lindhard, Scharf and Schiott (LSS) developed a theory to predict the range distribution of implants. This theory is thoroughly discussed by several authors (References 8-11) and has been shown to match experiment quite well. Tables have also been compiled giving  $R_p$  and  $\Delta R_p$  calculated from LSS for most implants in silicon. The values for Tl implants in Si at the energies used in this study are given below (Reference 12).

Implant Energy	Projected Range	Standard Deviation
280 keV	869 Å	213 Å
560 keV	1516 Å	366 Å

## b. Radiation Damage

One of the severest limitations of ion implantation is the crystal disorder or radiation damage resulting during the implantation process. Radiation damage occurs when an energetic particle imparts enough energy to a lattice atom to displace it from its normal site.

An implanted ion loses energy by two processes (Reference 13): (1) Excitation of the orbital electrons of the ion and lattice atoms resulting from inelastic collisions with the atoms and (2) elastic collisions involving the screened nuclei of the ion and atoms. Only the latter nuclear collisions create lattice disorder around the ion track resulting in radiation damage effects (Reference 8). The energy required to displace an atom from its normal lattice site is known as the displacement energy. The implanted ion makes very many violent collisions with the atoms of the crystal before it comes to rest. Each displaced atom will act as a secondary projectile if it receives energy greater than its displacement energy, which results in a cascade process of damage production (Reference 13). Disorder studies (Reference 11) of 200 keV Tl implants in Si show  $17,000 \pm 1,500$  Si displacements per incident Tl ion. For high doses, these cascade clusters overlap resulting in an amorphous layer. Common usage of "amorphous" in implantation studies refers to a noncrystalline region in which there is no long-range crystallographic ordering. However, this region may contain close-range order similar to that in crystalline Si. For 200 keV Tl implants in Si, an amorphous layer is formed (Reference 11) for doses greater than  $4 \times 10^{13}$  ions/cm<sup>2</sup>.

The amorphous zone can be epitaxially regrown by annealing to again form single crystal Si. Different defect structures dominate in the implant region depending on the anneal temperature. The divacancy is particularly important in room temperature implanted material since it is stable up to about 550 K (Reference 13). Divacancies can have several charge states  $V_2^+$ ,  $V_2^0$ ,  $V_2^-$  and  $V_2^{=}$ . In addition, a number of more complicated defects are believed to involve clustered defects and multiple vacancies. The various defects caused by implantation occur at depths less than or approximately equal to the ions depth into the material (Reference 13).

### c. Implant Damage Annealing

Annealing is the heat treatment of an implanted sample to regrow the crystalline structure of the substrate. Early Si ion implantation studies typically used isochronal anneals (often 10 min anneal periods) at consecutively higher temperatures. The amorphous implanted layer was found to reorder at 570°C (Reference 8). More recent studies (Reference 14) of self-implanted (Si implanted into Si) amorphous silicon show that at 550°C the amorphous layer thickness decreases linearly with time and the recrystallized layer grows epitaxially on the underlying crystal substrate. This is not the case however for higher temperature one-step anneals, where low solubility species (In, Sb and Pb) implanted in (111) Si have shown polycrystal formation when annealed directly to temperatures above 750°C (Reference 14). Once the polycrystals are formed, the grain boundaries provide short-circuit paths for migration of the implanted species out of the substrate. Also, for shallow implants, the impurity atoms migrate to the surface by way of extended defects during annealing. However, for In in Si, all the deep implants (340 keV) are retained after a 550°C anneal (Reference 15).

Another factor in annealing of implant layers is the directional dependence of regrowth rates, which have been shown to be much slower for (111) Si than for (100) Si. The regrowth rate for (100) self-ion bombarded substrates is about 80 Å/min at 550°C while for (111) substrates it is approximately 3 Å/min (Reference 15). Also, the regrowth on (111) Si is nonuniform in time and the interface is irregular (Reference 14). For the slower regrowth on (111) Si, the competition from nucleation of polycrystallites is much more severe than for the rapid epitaxial growth on (100) substrates. One-step annealing of (111) material at a temperature above 550°C results in considerable residual disorder, supposedly due to extended defects which arise from non-epitaxial regrowth. The residual disorder should be considerably reduced by first annealing at 550°C for a time sufficiently long for the layer to regrow epitaxially, then annealing at high temperature to remove the defects in this regrown layer (Reference 15).

Based on these results, Blood (Reference 15) et al. used a two-step method which significantly increased the percentage of implanted In and Sb retained in Si after annealing. Their first anneal was at 550°C for a time long enough for the layer to completely regrow epitaxially followed by a 940°C anneal to remove the defects in the regrown layer. They reported substitutional concentrations of implanted In in Si in excess of the solid solubility by using this process.

## 2. SAMPLE PREPARATION FOR THIS RESEARCH

### a. Sample Implantation

Samples were implanted by Hughes Research Laboratory. Both (100) and (111) Si wafers cut from the same 70 ohm-cm n-type boule were used for comparison between the two orientations. Only deep implants of 280 and 560 keV were used in order to reduce surface effects and the migration of Tl out of the Si. The wafers were implanted with Tl in a random direction at room temperature with doses of  $10^{13}$ ,  $10^{14}$ , and  $10^{15}$  Tl ions/cm<sup>2</sup>. The implant energies and doses for samples reported are given in Table 1.

### b. Two-Step Annealing

The implanted samples in this study were annealed using the two-step method reported by Blood (Reference 15) et al. The first temperature of 550°C was maintained for times sufficient to guarantee the complete regrowth of the layer using the direction dependent growth rates given above followed by a 30 min anneal at 940°C. Some samples were also single-step annealed at only 800°C for comparison. Also, various temperatures were used for the second anneal step to check for defects and activation. The anneal conditions for all samples reported are given in Table 1.

Samples were annealed in flowing argon in a temperature controlled Lindberg Heaviduty SB furnace. The anneal temperature was monitored with a Pt vs Pt-13% Rh thermocouple. The samples were sandwiched between

TABLE 1  
 SAMPLES USED IN THIS STUDY

Sample	Implant Energy (keV)	Dose Ions/cm <sup>2</sup>	Substrate Orientation	550°C Anneal	Second Anneal	Maximum Leakage Percent <200 K
Luminescence						
301	280	10 <sup>14</sup>	(111)	6 h	923°C 30 min	
303	280	10 <sup>14</sup>	(111)	6 h	940°C 30 min	
310	560	10 <sup>14</sup>	(100)	2 h	940°C 30 min	
406	Unimplanted	--	(111)	--	--	
407	Unimplanted	--	(100)	--	--	
438	280	10 <sup>14</sup>	(100)	1 h	950°C 1 h	
440	280	10 <sup>14</sup>	(100)		650°C 1 h	
441	280	10 <sup>14</sup>	(100)	1 h	850°C 1 h	
442	280	10 <sup>14</sup>	(100)	1 h	--	
443	280	10 <sup>14</sup>	(100)	1 h	750°C 1 h	
445	280	10 <sup>14</sup>	(100)	--	850°C 1 h	
446	280	10 <sup>14</sup>	(100)	--	950°C 1 h	
cs-6	bulk grown	4.48x10 <sup>16</sup> Tl/cm <sup>3</sup>	--	--	--	
cs-13	bulk grown	9.50 x10 <sup>15</sup> Tl/cm <sup>3</sup>	--	--	--	
Electrical						
285	Unimplanted	--	(111)	--	--	
286	Unimplanted	--	(111)	--	--	
287	Unimplanted	--	(111)	--	--	
449	280	10 <sup>14</sup>	(100)	6 h	940°C 30 min	1.0%
450	280	10 <sup>14</sup>	(100)	6 h	940°C 30 min	0.4%
457	280	10 <sup>14</sup>	(111)	14 h	940°C 30 min	1.3%
471	560	10 <sup>14</sup>	(111)	14 h	940°C 30 min	0.3%
472	560	10 <sup>14</sup>	(111)	14 h	940°C 30 min	3.8%
473	560	10 <sup>14</sup>	(111)	--	800°C 20 min	11.5%

TABLE 1 (Concluded)

Sample	Implant Energy (keV)	Dose Ions/cm <sup>2</sup>	Substrate Orientation	550°C Anneal	Second Anneal	Maximum Leakage Percent <200 K
Electrical						
522	280	10 <sup>13</sup>	(111)	14 h	940°C 30 min	37.8%
526	560	10 <sup>15</sup>	(111)	14 h	940°C 30 min	0.5%
532	280	10 <sup>13</sup>	(100)	6 h	940°C 30 min	23.5%
538	560	10 <sup>15</sup>	(100)	6 h	940°C 30 min	7.5%
539	560	10 <sup>14</sup>	(100)	6 h	850°C 30 min	5.8%
540	560	10 <sup>14</sup>	(100)	6 h	550°C 30 min	23.4%
548	560	10 <sup>14</sup>	(100)	6 h	745°C 30 min	10.3%
549	560	10 <sup>14</sup>	(100)	6 h	850°C 30 min	3.9%
550	560	10 <sup>14</sup>	(100)	6 h	745°C 30 min	21.0%
RBS						
293	280	10 <sup>14</sup>	(100)	--	--	
300	280	10 <sup>14</sup>	(111)	--	--	
307	560	10 <sup>14</sup>	(100)	--	--	
345	560	10 <sup>14</sup>	(111)	--	--	
393	280	10 <sup>14</sup>	(100)	1 h	--	
394	280	10 <sup>14</sup>	(100)	1 h	940°C 30 min	
397	280	10 <sup>14</sup>	(111)	6 h	--	
398	280	10 <sup>14</sup>	(111)	6 h	940°C 30 min	

ultra-high purity silicon wafers and held in a quartz boat. The samples were placed in the argon flow at least 30 minutes before entering the furnace and remained in the argon flow at least 30 minutes after removal from the furnace.

c. Sample Cleaning and Cutting

Samples were cleaned before each anneal and between each processing step in the application of electrical contacts to insure no contaminants were present. The following procedure was used:

1. Pre-wash
  - a. Rinse in 65°C trichloroethylene
  - b. Rinse in room temperature acetone
  - c. Rinse in 60° isopropyl alcohol
2. Boil in the following solution for 15 minutes at 30°C:  
5 parts distilled H<sub>2</sub>O  
1 part H<sub>2</sub>O<sub>2</sub> 30% unstabilized  
1 part NH<sub>4</sub>OH 27% solution
3. Boil in the following solution for 15 minutes at 30°C:  
5 parts distilled H<sub>2</sub>O  
1 part H<sub>2</sub>O<sub>2</sub> 30% unstabilized  
1 part HCl 37% solution
4. Rinse in distilled H<sub>2</sub>O

Samples for luminescence were cut with a diamond impregnated wire saw while mounted with the implanted side down in black wax. Electrical samples were cut with an ultrasonic cutter.

#### d. Electrical Measurement Samples

Samples for electrical measurements were cut in a van der Pauw (VDP) pattern with an ultrasonic cutter. Implanted layers were electrically isolated from the substrate by a p-n junction formed by implanting p-type Tl into n-type Si. The implanted wafers were first annealed at 550°C and then mounted with the implanted side down in black wax on plate glass. The VDP samples were then cut ultrasonically in the "clover leaf" shape shown in Figure 3 using SiC grit. The cut edges were then etched for one minute in CP4 (HNO<sub>3</sub> and HF) to remove sharp edges and pits caused by the ultrasonic cutting which might contribute to the leakage current through the junction. The etching was done with the wafer still in the black wax which prevented etching the implanted layer. A contact was then sparked on the back with Sb (Reference 16). The sample was removed by melting the wax and cleaned with the procedure outline above. The sample was then etched in a 10% solution of HF to remove SiO<sub>2</sub> layer from the implanted region. Gold wires were then soldered to each of the four implanted legs and to the contact sparked on the back.

The samples were screened with 2- and 3-point probes before mounting them in the Hall-effect apparatus. The 2-point probe was used to check that the contacts were ohmic and the 3-point probe tested the p-n junction between each of the four legs and the backside contact.

#### e. Bulk Doped Reference Samples

Two bulk grown Si:Tl crystals were used for reference in the luminescence study which allowed comparison with previous studies. These samples were grown by temperature gradient transport from a solution consisting of Si dissolved in a tin-thallium liquid-metal solvent (Reference 17) by Honeywell Corporate Physical Sciences Center. Sample cs-6 was grown from an 86:14 Tl to Sn ratio at 1370°C and sample cs-13 was grown from a 50:50 Tl to Sn ratio at 1335°C. Hall analysis (Reference 18) using an ionization energy of 0.246 eV and an empirical Hall scattering factor gave the following concentrations: cs-6

( $4.48 \times 10^{16}$  Tl/cm<sup>3</sup>,  $1.09 \times 10^{15}$  B/cm<sup>3</sup>,  $1.59 \times 10^{15}$  unknown acceptors/cm<sup>3</sup>, and  $9.50 \times 10^{14}$  donors/cm<sup>3</sup>) and cs-13 ( $9.50 \times 10^{15}$  Tl/cm<sup>3</sup>,  $1.73 \times 10^{15}$  B/cm<sup>3</sup>,  $6.54 \times 10^{14}$  unknown acceptors/cm<sup>3</sup> and  $1.76 \times 10^{15}$  donors/cm<sup>3</sup>). The concentration of Sn in sample cs-13 was measured (Reference 19) to be  $6 \times 10^{19}$  Sn/cm<sup>3</sup> by <sup>119</sup>Sn Mossbauer spectroscopy. The samples were etched in 5 parts HNO<sub>3</sub> to 3 parts HF and rinsed in deionized water before mounting in the He dewar.

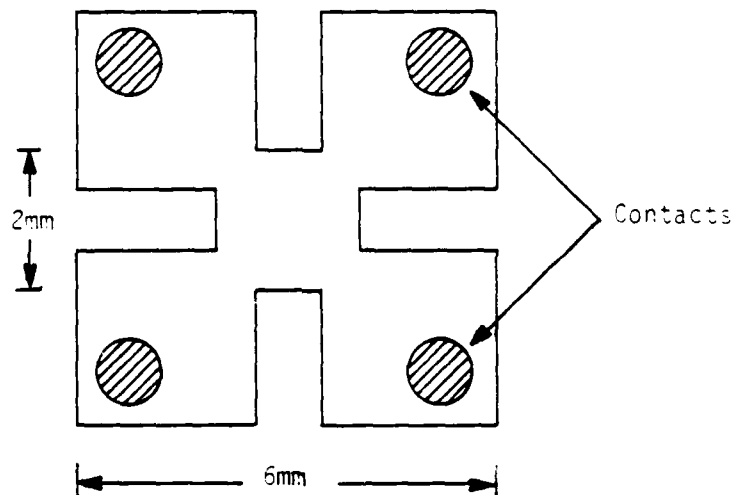


Figure 3. Van Der Pauw Pattern

## SECTION III

## LUMINESCENCE

## 1. SILICON LUMINESCENCE

Luminescence has been used to study dopants in bulk grown silicon and to study radiation defects in ion implanted silicon. Luminescence associated with group IIIA dopants in silicon was reported as early as 25 years ago (References 20-23). More recently, extensive studies have been conducted on the shallow group IIIA dopants (References 24-29) and on indium (References 27-32) in silicon. However, only three publications have reported luminescence from the deepest group IIIA acceptor, thallium (References 4, 27, and 33) in silicon. Until now, luminescence of doped silicon has been limited to bulk grown and diffused crystals, although luminescence has been shown to be an excellent technique for monitoring implant defects and studying the effects of various annealing methods. The luminescence studies reported in the literature on implanted silicon (References 34-42) are only on the defects and not on the implanted species. Since luminescence is so effective both in studying dopants and defects in Si, it seems an ideal monitor for implant layers from initial implant through the final anneal process. However, this has not been done before this study.

## a. Luminescent Mechanisms

Luminescence in intrinsic silicon is the result of radiative recombination of free excitons (FE) (References 23 and 43). Because Si has an indirect bandgap, the recombination must take place in conjunction with the emission of a momentum conserving phonon (Reference 44). The emitted photon has energy

$$E = E_{\text{gap}} - E_x - \sum_i E_i p_i \quad (3)$$

where  $E_{\text{gap}}$  is the bandgap energy,  $E_x$  is the ground state binding energy of the exciton, and  $E_{p_i}$  is the energy of an emitted phonon. An intrinsic Si luminescence spectra is shown in Figure 4. The dominant lines are associated with exciton decay assisted by the emission of a transverse (TA), longitudinal optical (LO), or transverse optical (TO), phonon (Reference 45). For low enough temperatures and high enough excitation energies, luminescence from electron-hole droplets (Reference 46) (EHD) is also seen in Si. The luminescence spectra obtained at 10 K show the EHD peaks in Figure 4.

When Si is doped, the impurities provide traps where excitons can be bound. Lampert (Reference 47) first suggested the existence of bound exciton (BE) complexes and derived the limiting binding energies of some of the simpler complexes by analogy with different charge states of the hydrogen atom and molecule (Reference 45). The energy of a photon emitted due to the recombination of a BE is given by

$$E = E_{\text{gap}} - E_x - E_{\text{bx}} - \sum_i E_{p_i} \quad (4)$$

where  $E_{\text{bx}}$  is the localization energy of the bound exciton. From Equation 3 and 4,  $E_{\text{bx}}$  is determined by the difference between the BE lines and their corresponding FE components. The first observation of the BE was in Si by Haynes (Reference 21), who found for shallow donors or acceptors,  $E_{\text{bx}} \approx 0.1 E_i$ , where  $E_i$  is the ionization energy of the donor or acceptor.

If the exciton were bound to an ionized acceptor, i.e. an immobile three-particle complex consisting of the negative acceptor ion, a hole, and an electron, then  $E_{\text{bx}}$  would be approximately equal to  $E_i$  rather than  $0.1 E_i$ . The exciton-impurity binding should therefore be viewed as a four-particle complex consisting of an electron bound to a negative acceptor ion by a hole pair bound (References 21 and 45). The BE transition  $A^0X \rightarrow A^0$  observed in p-type Si is diagrammed below (Reference 42)

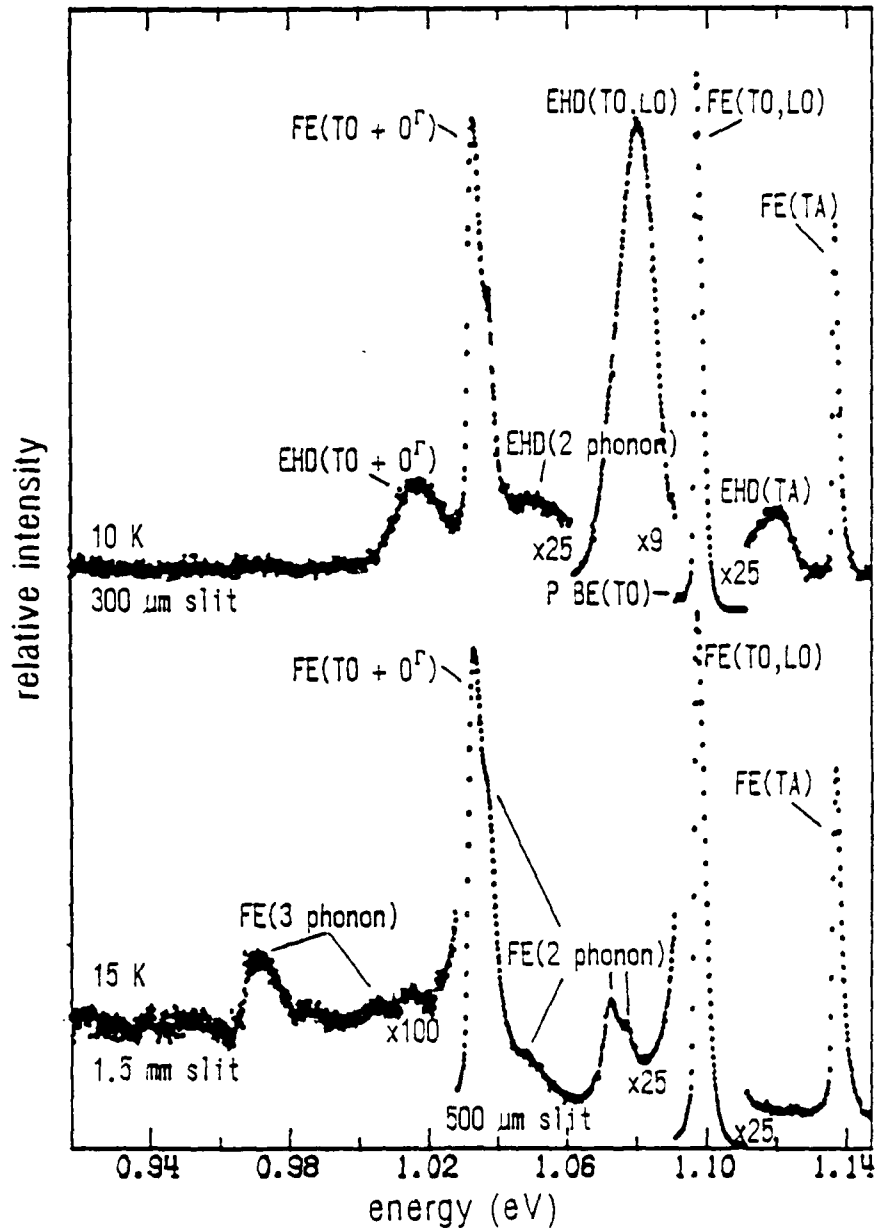
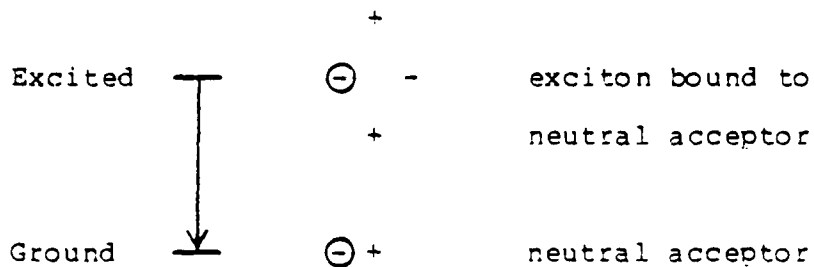


Figure 4. Photoluminescence from 70 Ohm-cm Silicon Substrate Material at 10 and 15 K (Intensity not Corrected)



where  $\ominus$  represents an acceptor  $+$  represents a hole, and  $-$  represents an electron.

Momentum may be conserved for bound exciton transitions through coupling to the impurity atom in addition to the emission of phonons (Reference 45). A no-phonon (NP) transition is therefore found in BE spectra which is not possible for FE recombination. The ratios of the intensities of the no-phonon and momentum conserving phonon assisted luminescence peak increases monotonically with the localization energy of the BE (Reference 45).

Particle irradiation of Si suppresses the normal FE or BE luminescence and defect related luminescence is observed instead (References 34-41). This defect luminescence is characterized by dominant NP peaks due to electronic transitions at defects and by the associated lower energy peaks resulting from phonon cooperation in the transitions (Reference 38).

Electron-beam excitation (cathodoluminescence) and optical excitation (photoluminescence) are commonly used techniques (Reference 48) for the production of high densities of electron-hole pairs (excitons) to be studied by their recombination radiation. In cathodoluminescence a beam of primary electrons of energy less than 100 keV is focused on the surface of the crystal. Each primary electron ultimately produces many thousands of secondary electron-hole pairs. In photoluminescence, a laser or intense lamp beam is focused on the surface of the crystal with an electron-hole pair produced for each absorbed photon. Although the mechanisms for producing the excitons are different, the

resulting recombination mechanisms are the same; therefore, cathodoluminescence and photoluminescence results are equivalent except for the depth at which the luminescence originates.

b. Previous Results for Si:Tl

The first luminescence from Si:Tl was reported by Vouk and Lightowers (Reference 4). Their three samples had very low Tl concentrations,  $4 \times 10^{14} \text{cm}^{-3}$  for the bulk doped sample and  $3 \times 10^{15} \text{cm}^{-3}$  and  $2 \times 10^{16} \text{cm}^{-3}$  for the diffused samples. Study of the bulk doped sample was difficult due to FE and EHD interference, and the diffused samples contained considerable B contamination. The only Tl related features detected were the BE(NP) and BE (TO) transitions. The Tl BE(NP) was resolved into a thermalizing triplet structure. The BE localization energy was determined to be 43.8 meV.

Elliott (Reference 33) et al. observed the BE(NP) with both absorption and luminescence. Their sample contained  $3 \times 10^{16} \text{cm}^{-3}$  Tl. They observed four thermalizing lines in the spectra by both techniques. They also determined a BE localization energy of 44.2 meV. Thewalt (Reference 49) et al. also studied bulk grown Si:Tl with a concentration of  $5 \times 10^{16} \text{cm}^{-3}$  Tl. They however studied lines associated with isoelectronic BE's rather than the Tl BE spectra. The samples were treated by heating and quenching to produce the intense isoelectronic bound exciton like luminescence.

## 2. LUMINESCENCE SYSTEM

Both photo- and cathodo- luminescence systems, which yield the same results, were used in this study. Cathodoluminescence was used for the earlier work. The equipment configuration was the same as for the photoluminescence, Figure 5. The electron gun was variable from 4-15 kV and has a maximum beam current of 3u A. The high voltage supply was equipped with a photo-isolator allowing beam shaping by a pulse generator. To improve the signal-to-noise ratio of the detection system, the beam was pulsed with a square wave of 40 Hz. The cathodo-

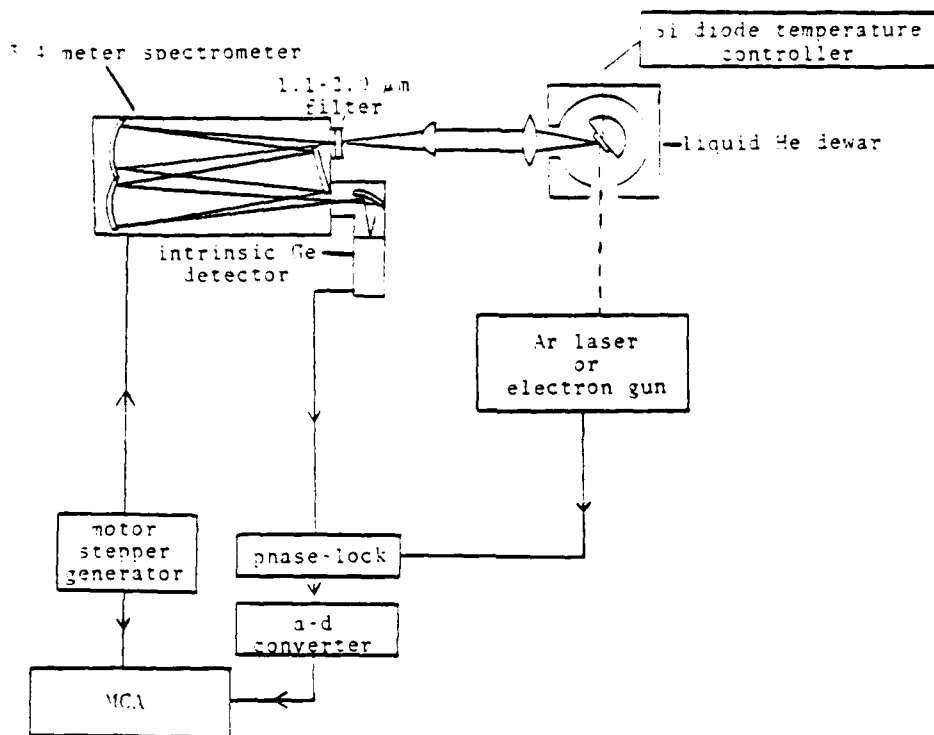


Figure 5. Schematic Diagram of Luminescence System

luminescence system was equipped with focusing, astigmatism, and deflection coils for easy manipulation of the electron beam. The samples were mounted with clips on a copper block attached to a Heli-tran. The sample block has a  $45^\circ$  face to permit sample excitation by a vertically accelerated beam of electrons and horizontal collection of the emitted luminescence. The temperature was monitored with a Lake Shore Si diode, DT-500KL, embedded in the copper block and controlled by a Lake Shore controller connected to a heating coil on the copper block. The samples and electron gun were maintained in a diffusion pumped vacuum system with the pressure maintained below  $10^{-6}$  Torr during operation. The maximum power on the sample was 45 mW which was not sufficient for high resolution spectra from Si:Tl.

Photoluminescence was used during the latter part of the study due to the higher excitation powers available. The photoluminescence spectra were obtained by illuminating the samples with the  $4880 \text{ \AA}$  line of a Spectra Physics 164 Ar-ion laser mechanically chopped at 53 Hz. The infrared lines of the Ar discharge were filtered out with an Optics Technology #700 low pass filter. The filtered and chopped beam was variable up to 360 mW as measured with a Scientech 362 power meter. The photoluminescence samples were mounted on the copper tail of a Janis flowing helium cryostat equipped with quartz windows. The temperature control was the same as in the cathodoluminescence system.

The emitted radiation was collected and analyzed in the same manner for both systems. The front-surface luminescence was collected by a spherical quartz lens located a focal length away from the sample, and the collimated light was then focused onto the entrance slit of a Spex 1702 spectrometer with a quartz cylindrical lens. Both 600 grooves/mm and 1200 grooves/mm diffraction gratings were used. The dispersed light was focused with a spherical mirror onto an ADC model 403 intrinsic germanium photodetector. The signal was processed with an Ithaco 353 phase-lock amplifier, digitized with an HP 2212 analog to digital converter, and then stored in a multi-channel analyzer (MCA). The spectrometer and MCA were simultaneously driven by a stepper-motor pulse generator.

The data were computer analyzed and plotted. The spectra were corrected for transmission losses and detector response using a blackbody as the reference. The spectral response to the blackbody and the corresponding correction function are shown in Figure 6. An argon lamp or the 11,078.868 Å line of the laser Ar discharge was used for wavelength calibration.

### 3. REFERENCE LUMINESCENCE RESULTS

The luminescence from implanted Si:Tl samples was found to be dominated by the FE spectra from the substrate. In order to establish which part of the spectra was associated with the Tl implants, the unimplanted substrate material and bulk grown Si:Tl were also examined by luminescence.

#### a. Substrate Luminescence

The recombination luminescence at 15 K from the 70 ohm-cm substrate material used for the implant studies is shown in Figure 4. The FE phonon replicas have been labeled after Vouk and Lightowers (Reference 43). The second plot shows the same sample as the first with the same excitation power but at 10 K. The phonon replicas of the EHD recombination are clearly evident in the lower temperature spectra. The excitation threshold for EHD formation in intrinsic Si depends on temperature and excitation pulse length (Reference 50). The temperature dependence of the EHD formation in the substrate material is shown in Figure 7 at the same resolution used for most of the Si:Tl spectra. No EHD recombination was seen in any of the Tl doped samples at temperatures down to 4.2 K.

#### b. Bulk Doped Si:Tl Luminescence

Two bulk grown Si:Tl samples were used, see Section II, subsection 2d. The luminescence spectrum from sample cs-13 is shown in Figure 8. Readily identified peaks are the BE no-phonon (NP) transition

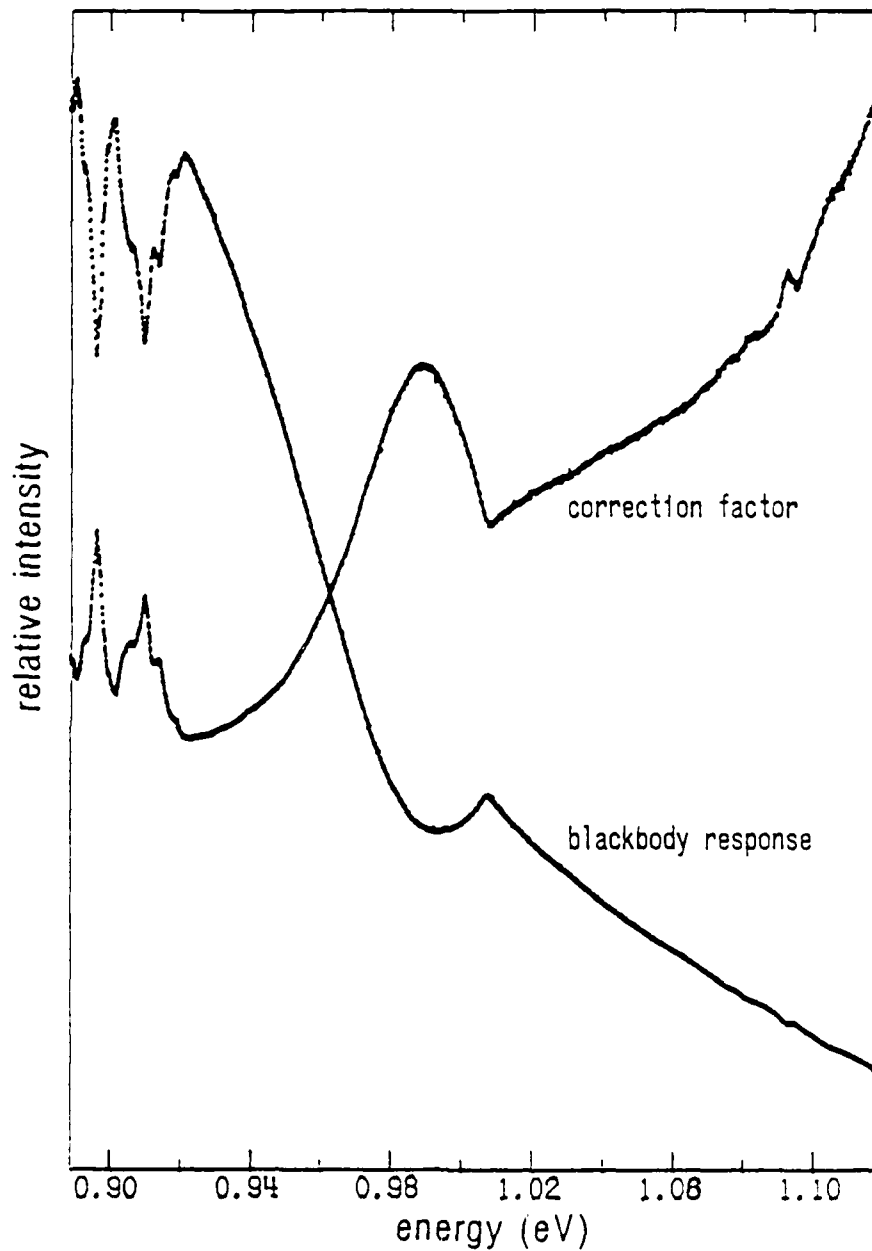


Figure 6. System Response to a Blackbody Radiator at 1050 K and the Corresponding Correction Factor

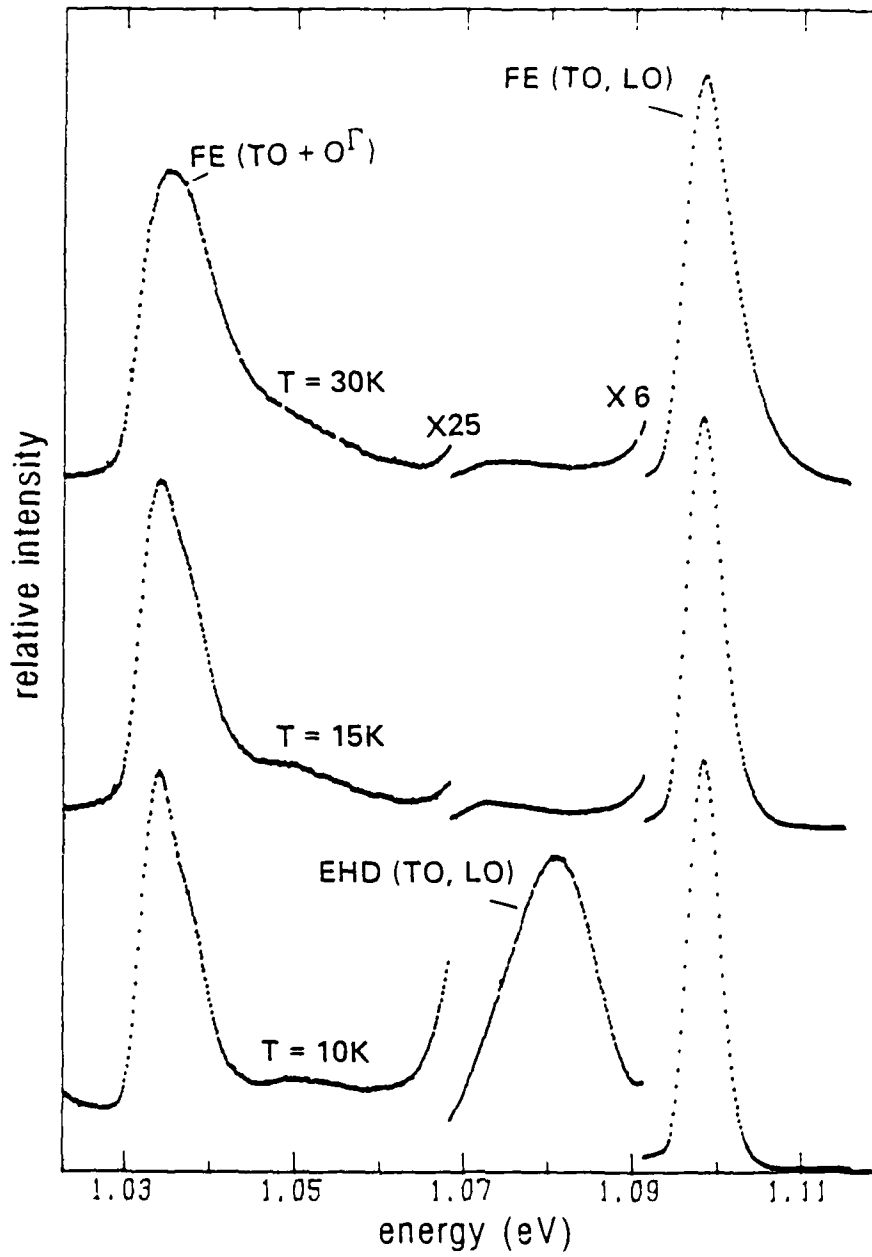


Figure 7. Photoluminescence of the Silicon Substrate at Temperatures from 10 K to 30 K. Sample 407.

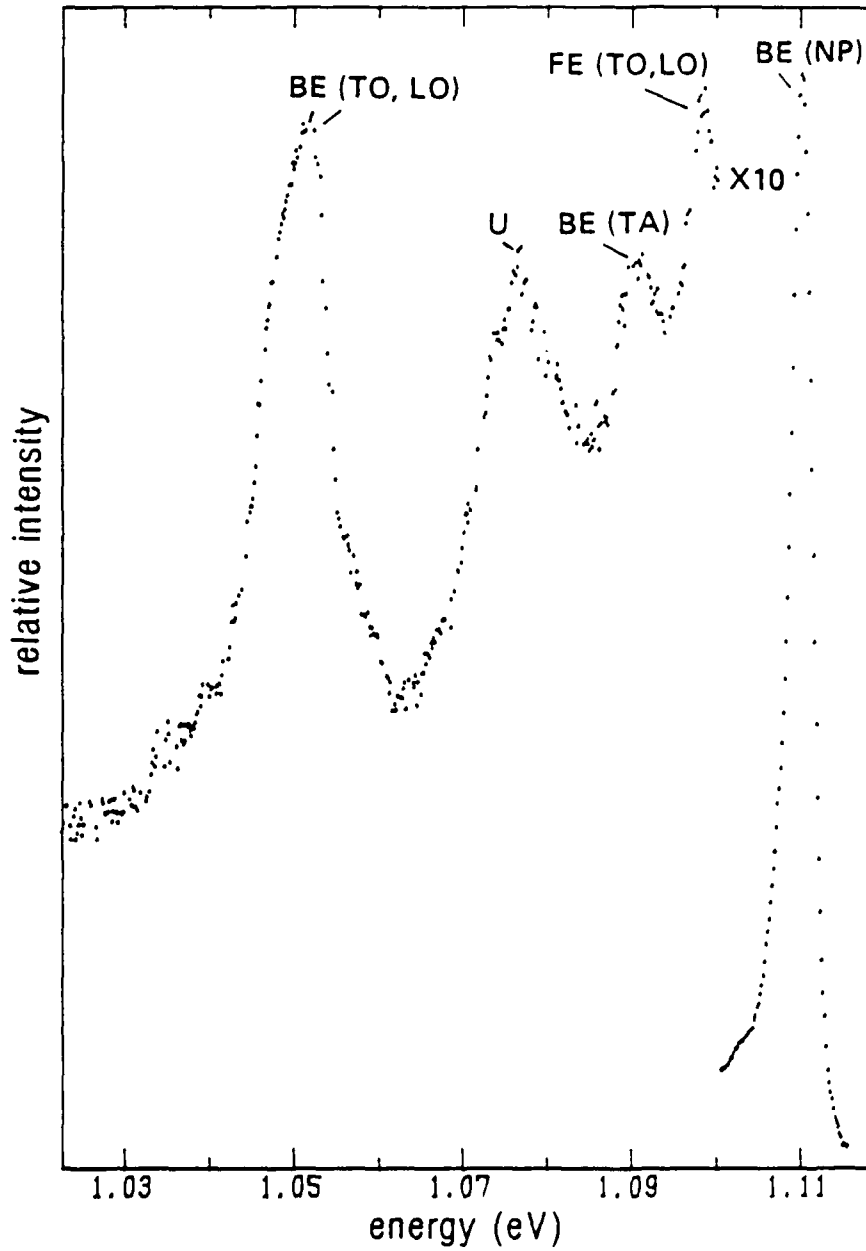


Figure 8. Photoluminescence Spectrum of Bulk Grown Si:Tl. Sample cs-13.

and its transverse acoustic (TA) and transverse optical plus longitudinal optical (TO,LO) phonon replicas. The BE(TA) line has not been previously reported for Si:Ti. The (TO,LO) phonon replica of the free exciton (FE) is also evident, but note that the FE spectra is negligible in Si:Ti. The BE localization energy was determined to be 44.3 meV using the FE(TO) from the intrinsic substrate material and 58.0 meV (Reference 43) as the energy of the TO phonon. An unexpected transition (U) 33.9 meV below the BE(NP) is also found in this spectrum. The energies of the peak intensities of the lines associated with the T1 acceptor are summarized in Table 2.

TABLE 2

## ENERGIES OF THE T1 ASSOCIATED LUMINESCENCE LINES, SAMPLE CS-13

Line	Peak energy (eV)
BE(NP)	1.1110
BE(TA)	1.0915
U	1.0771
BE(TO,LO)	1.0518

The luminescence spectrum from sample cs-13 was investigated as a function of pump power and temperature. The ratios of the U line intensity to the BE(NP), BE(TA), and BE(TO) line intensities remain constant with temperatures from 10 to 20 K, Figure 9, and laser pump powers in the range of 29 to 251 mW, Figure 10. These constant ratios indicate that the transition U has the same initial state as the BE transition. Similar results were obtained from the ion implanted specimens.

The luminescence from sample cs-6 was more complex and is shown in Figure 11 along with the spectrum of sample cs-13 from Figure 8. The lines coincide with those reported by Thewalt (Reference 49) et al. which they identified as due to isoelectronic BE recombination. Their samples

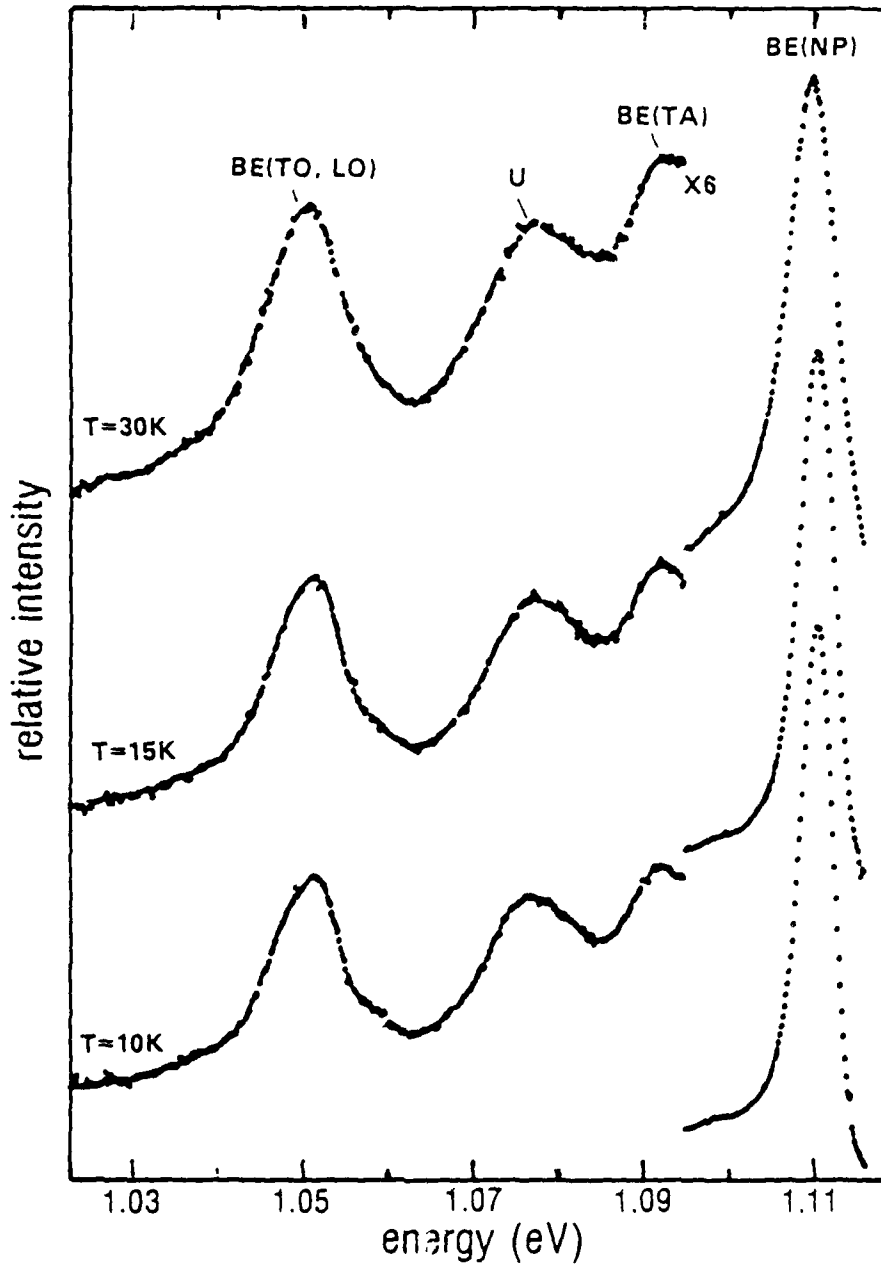


Figure 9. Photoluminescence Spectra of the T1 BE Taken at Temperatures from 10 K to 30 K. Sample cs-13.

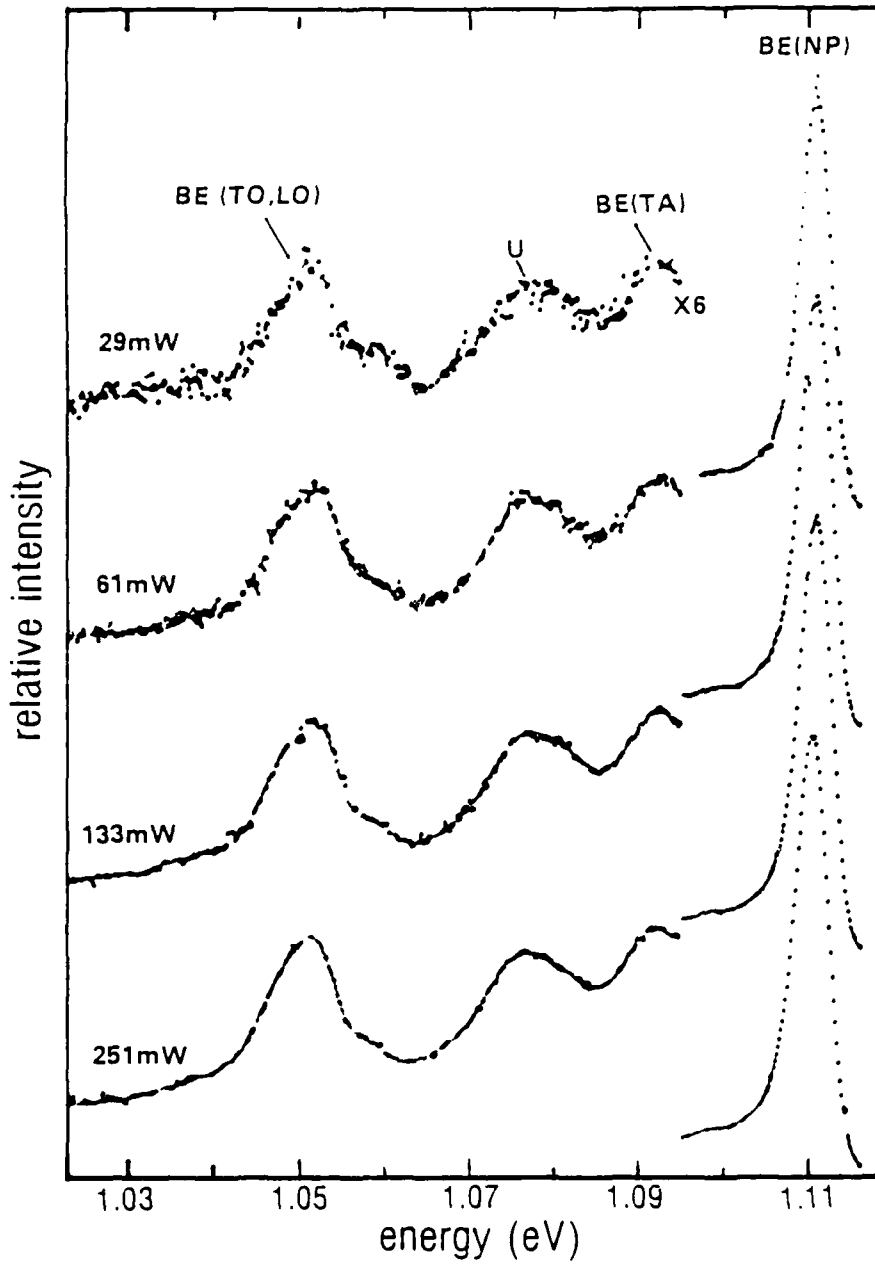


Figure 10. Photoluminescence Spectra of Tl BE at 10 K and Excitation Powers Ranging from 251 mW to 29 mW. Sample cs-13.

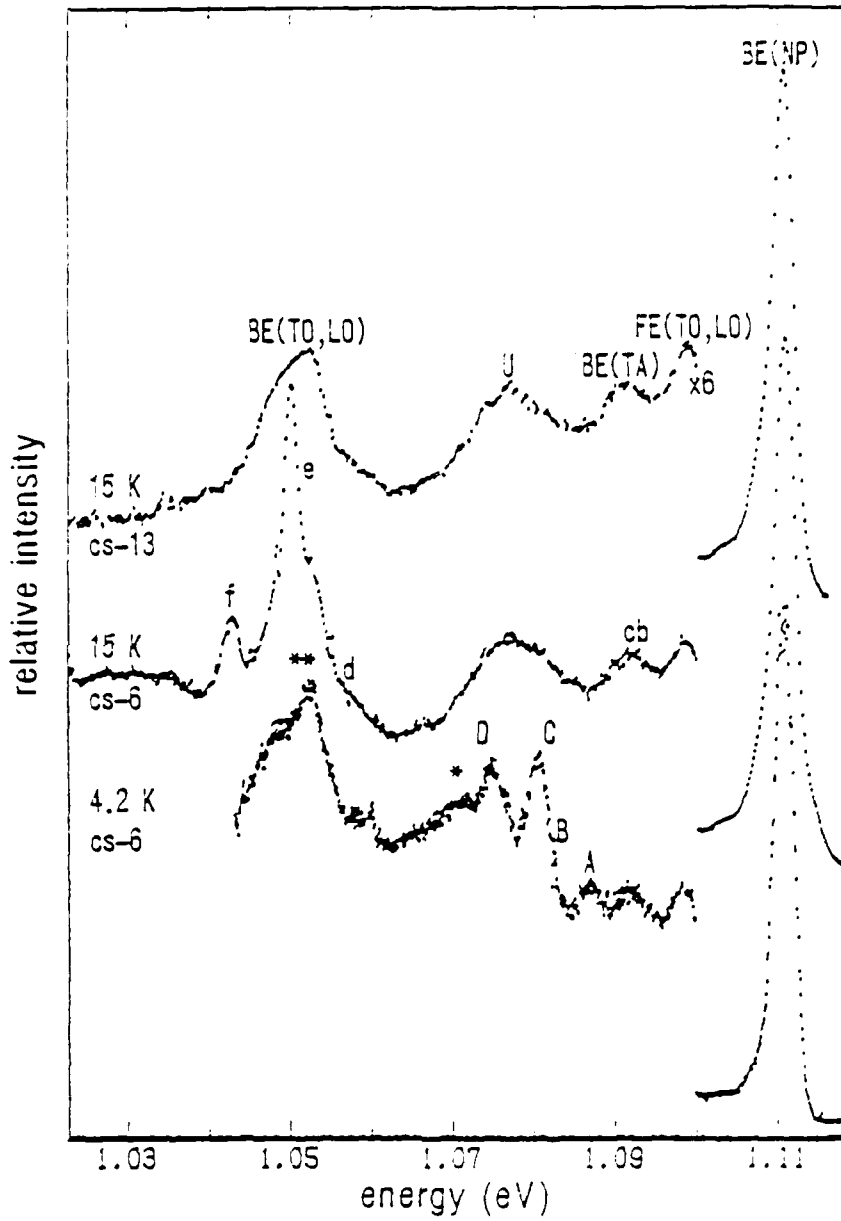


Figure 11. Comparison of Photoluminescence Associated with Isoelectronic BE and with the T1 BE (Intensity not Corrected).

were obtained from the same source as samples cs-6 and cs-13. The lines in Figures 11-13 have been labeled using their convention. They did not observe any of the isoelectronic BE lines until their samples were given a heat-quench treatment; however, sample cs-6 received no heat treatment after it was grown. They also did not report any of the underlying T1 BE structure except for the BE(NP). The temperature dependence of the isoelectronic BE luminescence is shown in Figure 12. Additional lines not reported before are seen in the low energy region of the spectrum in Figure 12. At 60 K the T1 BE structure has disappeared leaving the lines b,c and f,e and the recombination radiation from free electrons and holes. The line D also appears to grow with temperature. The excitation power dependence is also given in Figure 13. A saturation effect is clearly evident indicating a low concentration of the centers causing the isoelectronic BE lines. At high pump power, the spectra is dominated by the T1 BE lines.

#### 4. IMPLANTED SI:T1 LUMINESCENCE

##### a. Unannealed Implanted Samples

Cathodoluminescence from an implanted but unannealed sample is shown in Figure 14. The spectra is dominated by defect associated luminescence with a small amount of FE recombination radiation present from the substrate. The spectra were identical for implants into (100) and (111) material and for 280 and 560 keV implant energies except for the relative intensity of the FE luminescence to the defect luminescence. The FE luminescence was nearly nonexistent for (100) material and its relative intensity with respect to the defect luminescence decreased with implant energy for both orientations.

A low resolution plot is also shown in Figure 14 which is very similar to the unannealed spectra of Kirkpatrick (References 36 and 38) et al. They made tentative identifications of several of these lines. The defect lines in Figure 14 have been labeled after Kirkpatrick (Reference 13), and these lines are summarized in Table 3. The relative intensities of lines I1, I1(TA), and I1(LA) are constant with temperature

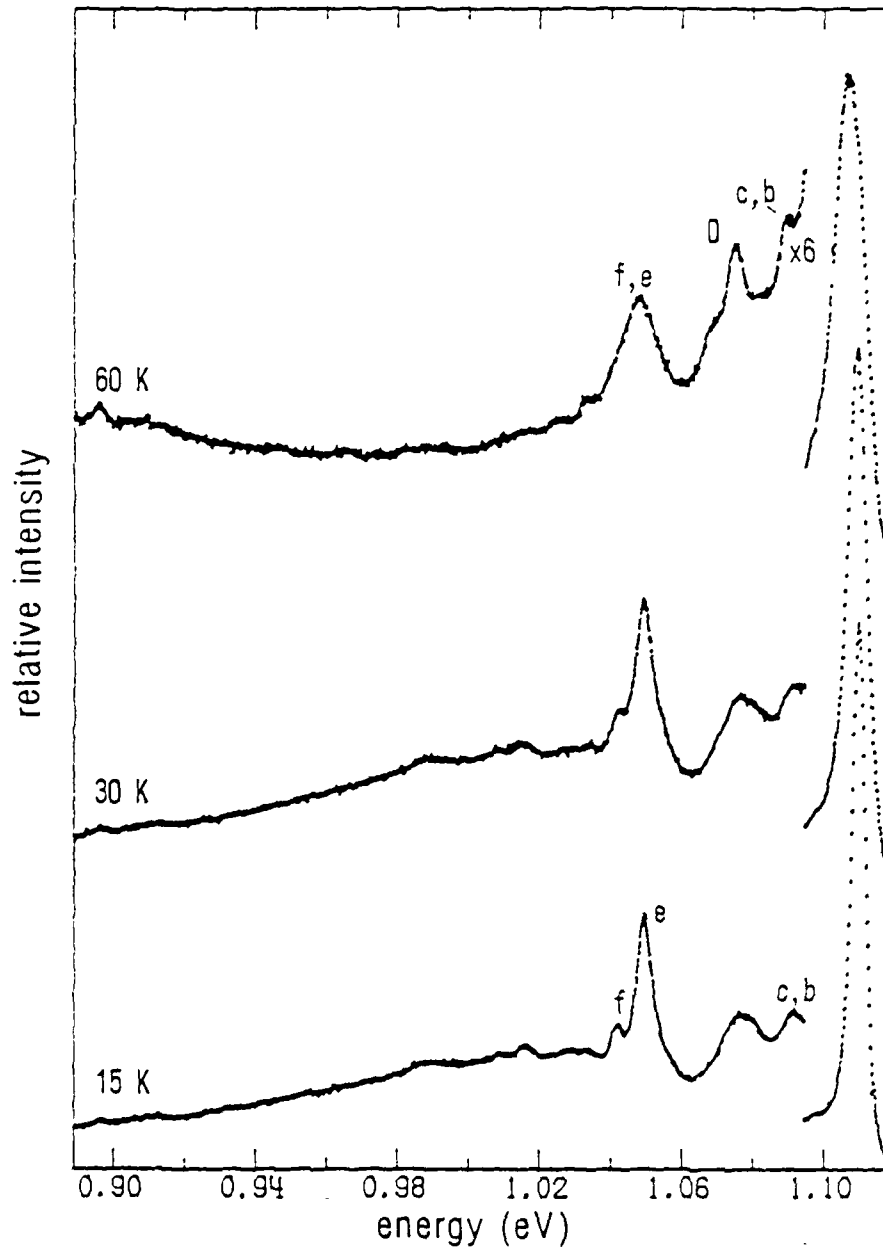


Figure 12. Photoluminescence Spectra of the Isoelectronic BE Taken at Temperatures from 15 K to . . . K. Sample cs-6.

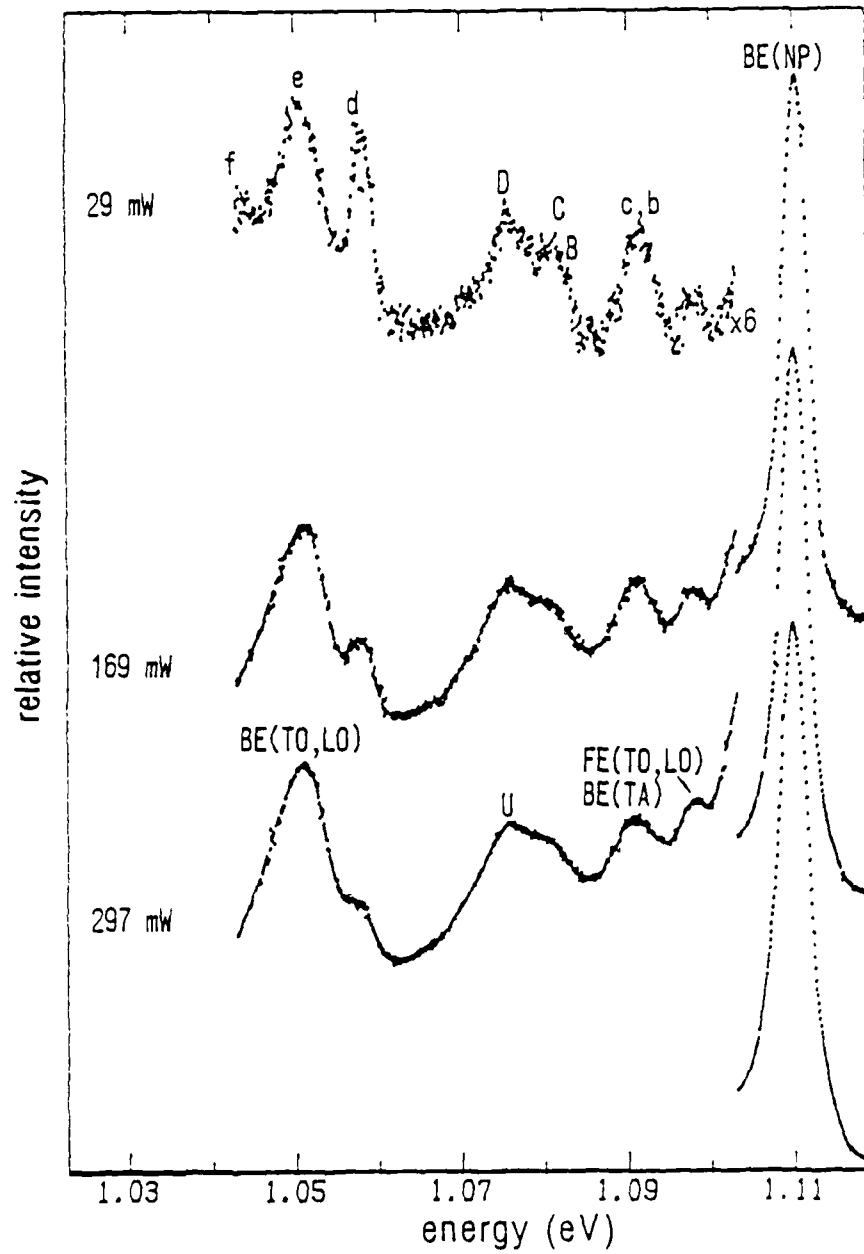


Figure 13. Photoluminescence Spectra of the Isoelectronic BE for Excitation Powers Ranging from 297 mW to 29 mW. Sample cs-6 at 15K.

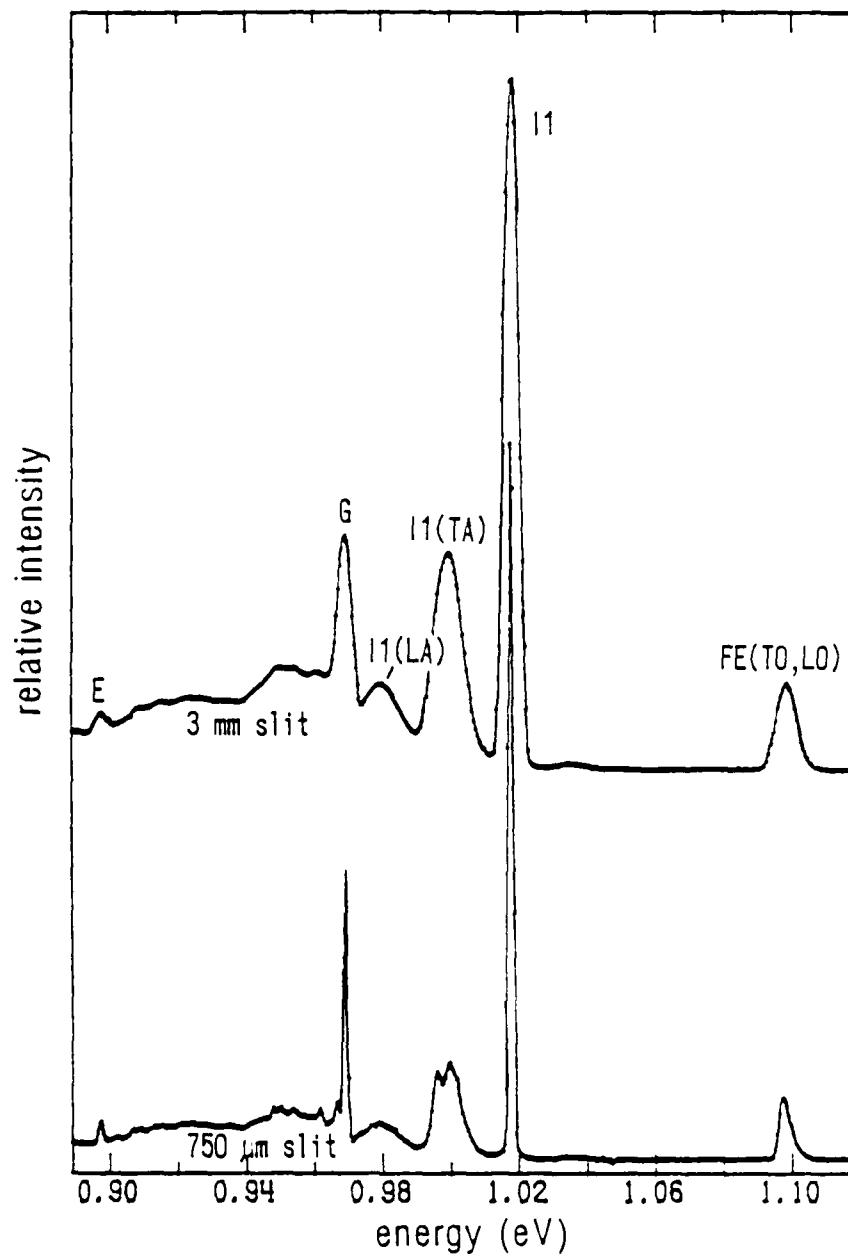


Figure 14. High and Low Resolution Cathodoluminescence of Unannealed Implanted Si:Tl at 24 K. Sample 3J3 (Intensity not Corrected).

TABLE 3

## DEFECT LUMINESCENCE

Kirkpatrick Identification	Kirkpatrick R.T.	3mm slit 1st order R.T.	1mm slit 2nd order R.T.
FE(TO)	1.096	1.098	1.098
I4	1.034	1.035	1.034**
I1	1.018	1.018	1.018
			1.000
I1(TA)	0.998*	1.000	
			0.996
I1(LA)	0.978*	0.979	0.981
G	0.970	0.969	0.970
			0.967
		0.966	
			0.963
I1(TO)	0.956*		0.955
G(TA)	0.950		0.951**
			0.948
E	0.897	0.898	0.898**
C	0.790		

\* After 200°C anneal

\*\* 750  $\mu$ m slit, 1st order

indicating they are associated with the same defect while line G has a different temperature dependence, Figure 15. The intense line I1 has been identified as due to recombination at a five vacancy cluster defect, and the G peak has been identified as due to a carbon dependent center (Reference 38). The line splittings appearing in the higher resolution results of this study (Figure 14) do not support the previous identifications of the fine structure between G and E as phonon replicas of G nor of the identification of a phonon wing associated with I1.

Defect lines similar to those introduced by ion implantation have been seen in luminescence studies of radiation damage introduced by other mechanisms in Si. Unimplanted substrate material was laser annealed and examined by luminescence for comparison with the ion implanted samples. The lines G and E were also introduced by the laser irradiation, Figure 16. Luminescence of 70 ohm-cm n-type Si irradiated with fast neutrons or gamma rays (Reference 51) showed very similar results.

#### b. Two-Step Annealed Samples

The unannealed defect luminescence is removed after a 550°C anneal and replaced by a broad structure containing many lines, Figure 17. The defect structure in the 15 K plot of Figure 17 is identical to that of the 30 K spectrum if magnified. The only difference between the two spectra is the intensity of the defect structure relative to the FE intensity. The broad structure introduced by the 550°C anneal is in turn replaced by another broad peak after the 650°C anneal, which is similar to the dominant peak reported by Street (Reference 40) et al. for laser annealed self-implanted Si. The defect luminescence largely disappears after the 750°C anneal, and all of the defect luminescence has disappeared after the 950°C anneal, Figure 18. The samples in Figure 18 were all taken from the same wafer, (100) Si implanted at 280 keV. They were all annealed at 550°C for one hour in the same batch. Their respective second anneals were for one hour also.

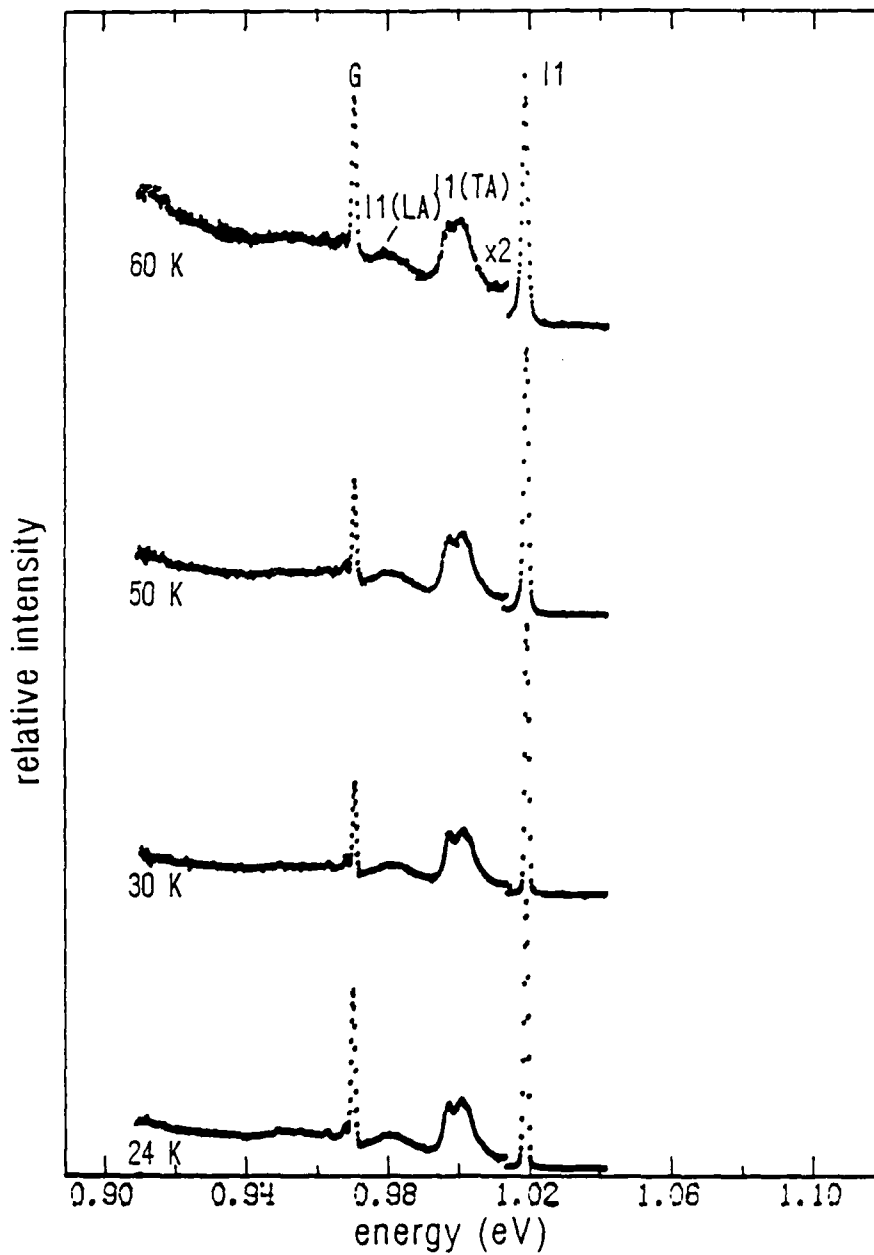


Figure 15. Temperature Dependent Cathodoluminescence of Un-Annealed Implanted Si:Tl. Sample 303 (Intensity not Corrected).

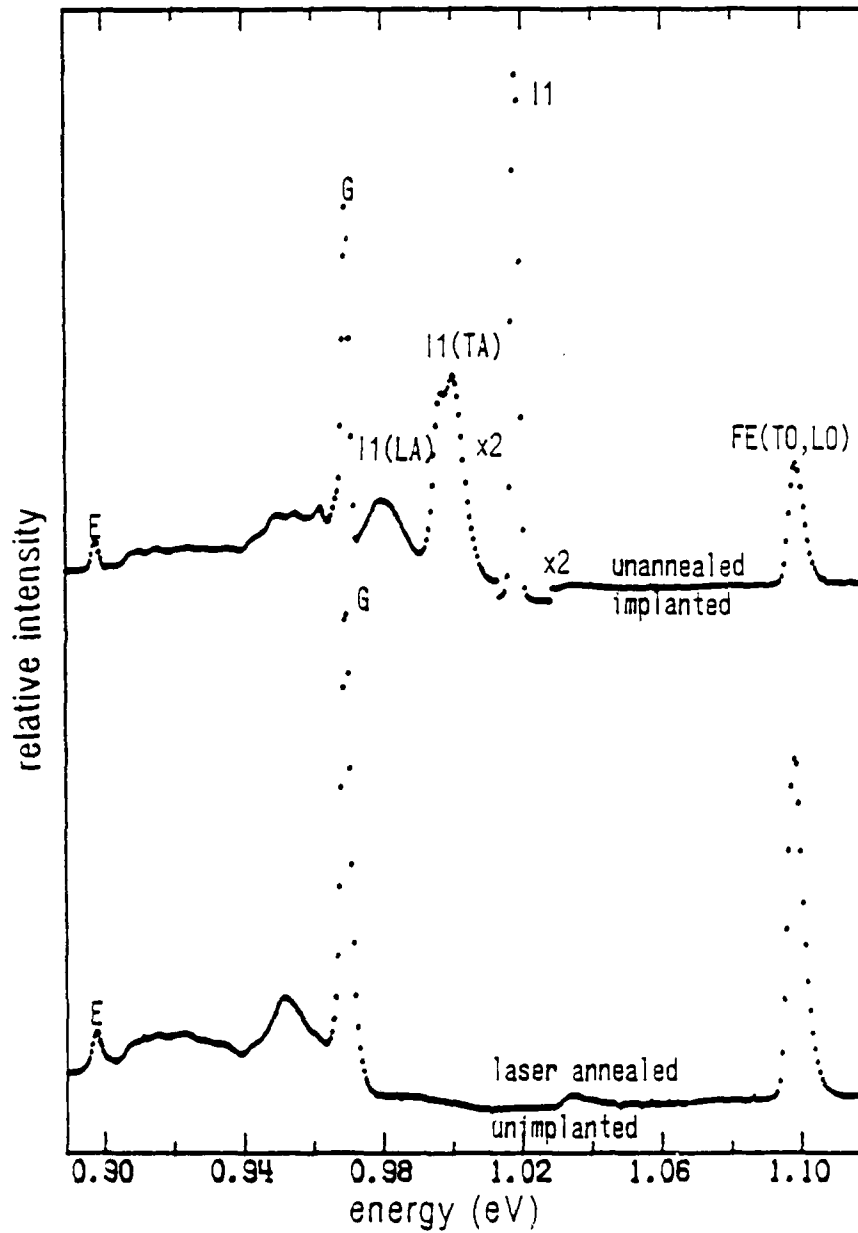


Figure 16. Cathodoluminescence from Laser Annealed Unimplanted Si and Unannealed Implanted Si:Tl Samples 406 and 303 (Intensity not Corrected).

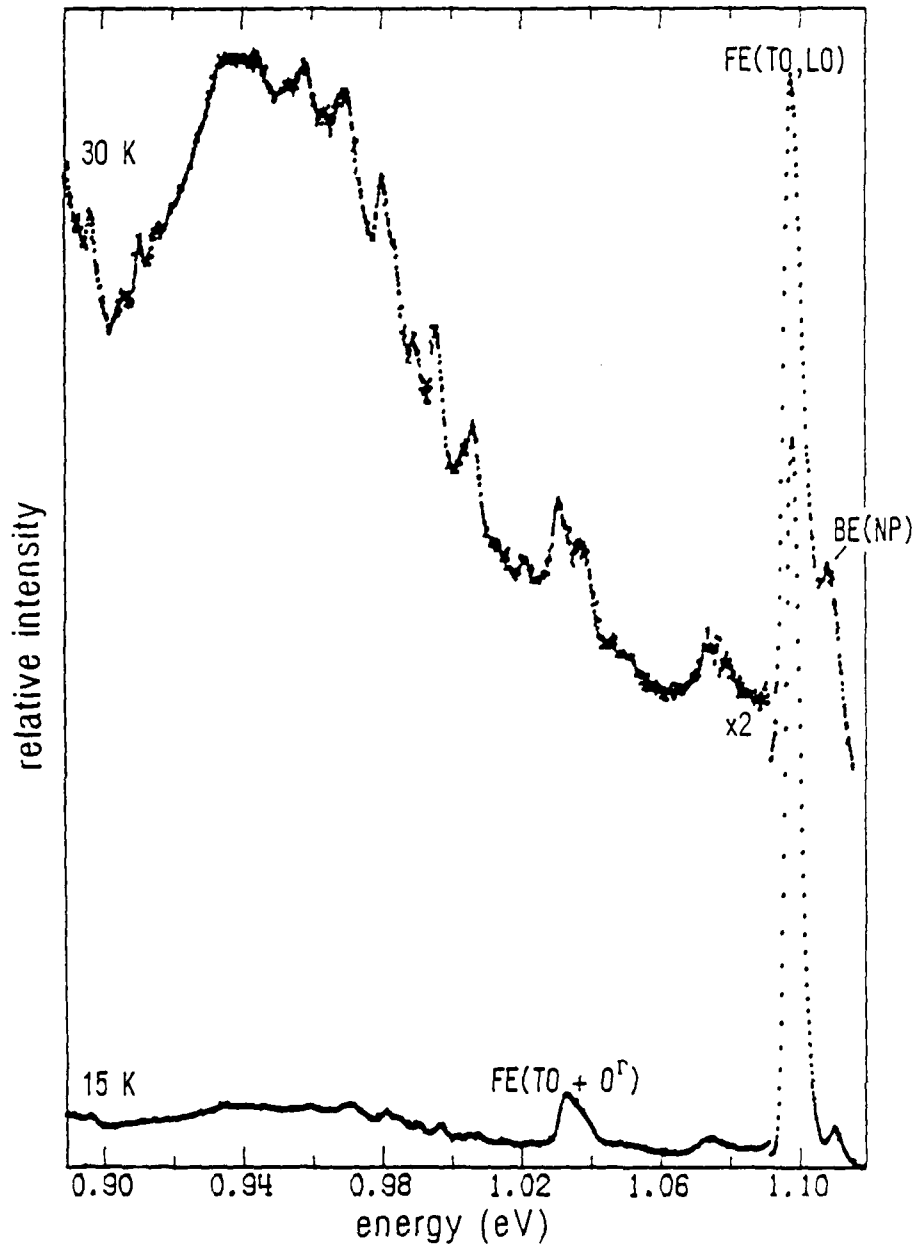


Figure 17. Photoluminescence from Ion Implanted Si:Tl at 15 K and 30 K after a 550°C Anneal. Sample 442.

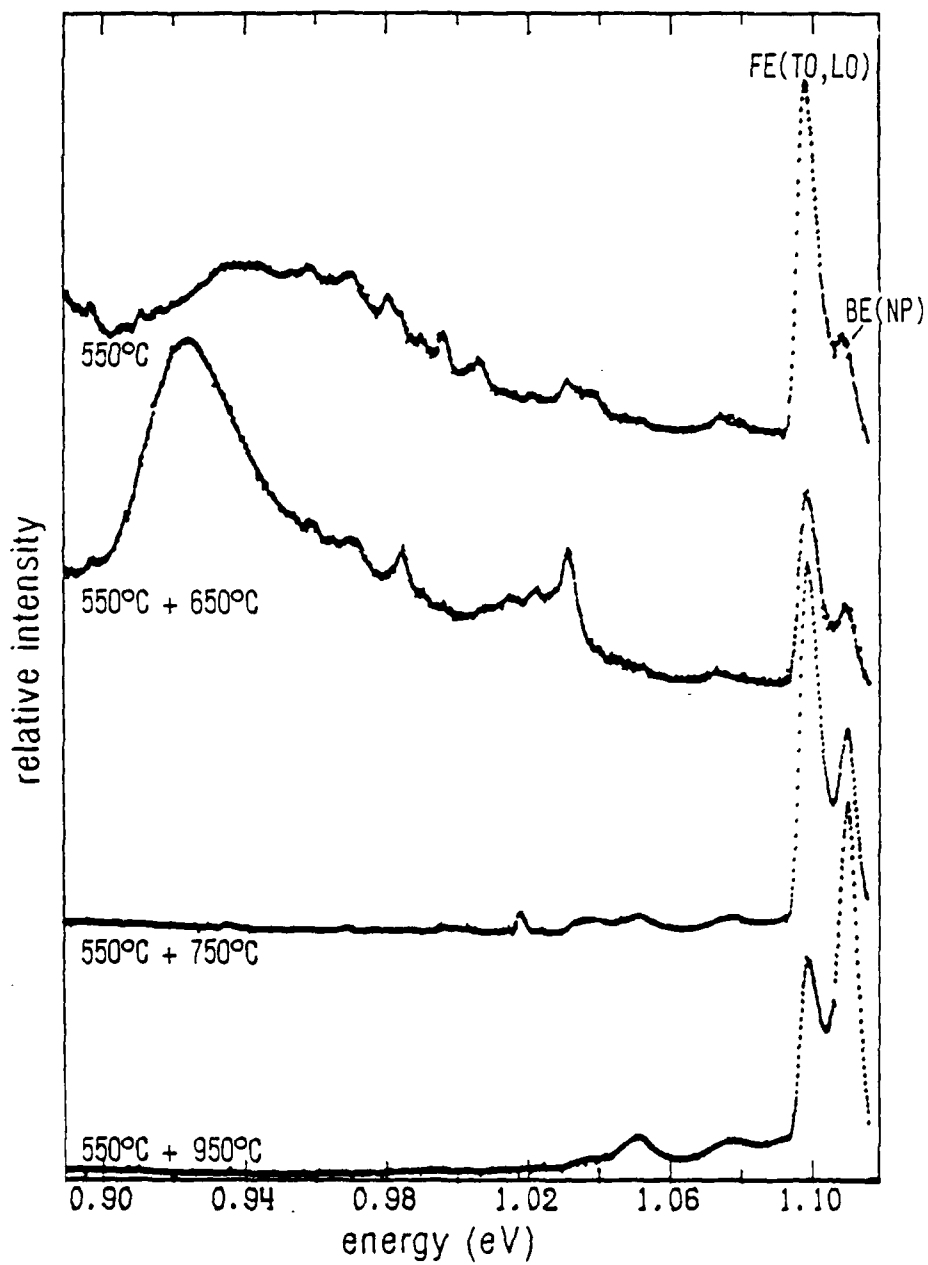


Figure 18. Photoluminescence from Ion Implanted Si:Tl at 30 K after Anneals at 550°C, 550°C + 650°C, 550°C + 750°C, and 550°C + 950°C. Samples 442, 440, 443, and 438.

The ability to detect the presence of the defect peaks present after 550°C and 650°C anneals has major significance for electrical property considerations. Early electrical studies of ion implants often used final anneals of only 550-700°C for which defects do exist, and consequently these defects could strongly affect the mobility and compensation. Luminescence also provides the capability to monitor the optical activity of the implanted dopant.

No Tl associated BE luminescence was observed from the unannealed amorphous layer. After the implanted samples had been epitaxially regrown at temperatures of 550°C, the Tl BE spectra was present in all samples, Figure 17. The Tl optical activation as indicated by the BE(NP):FE(TO) ratios, Figure 19, then increased with increasing temperature up through 950°C.

Single temperature anneals were also made for comparison with samples cut from the same wafer as for Figure 18 and 19 and annealed with the two-step anneal samples during their respective high temperature anneal. Variations in the BE(NP):FE(TO) ratio were seen when the exciting beam was moved across the samples single-step annealed at 750°C, 850°C, and 950°C. Very localized spots were found which had very intense Tl BE luminescence. By defocusing the electron beam, the luminescence from several of the spots was collected at one time. A large increase in the BE(NP):FE(TO) ratio was seen by defocusing the beam centered on the 850°C anneal sample, Figure 20. The scans were made at approximately the same temperature, beam current, and acceleration voltage. Part of the change in the ratio with defocusing may be accounted for by a saturation effect when BE's are associated with all of the Tl atoms in the area of the focused beam. A slight increase in the ratio was seen by defocusing for some of the two-step annealed samples. However, no change in the ratio for the 850°C single-step anneal sample was seen by varying the beam power from 31 mW to 5 mW with the beam focused. The variations for two positions and for the beam focused for the 950°C single-step anneal sample are shown in Figure 21. The variations in the ratio when moving the beam across the sample were not seen for the two-step annealed samples. This suggests that for the

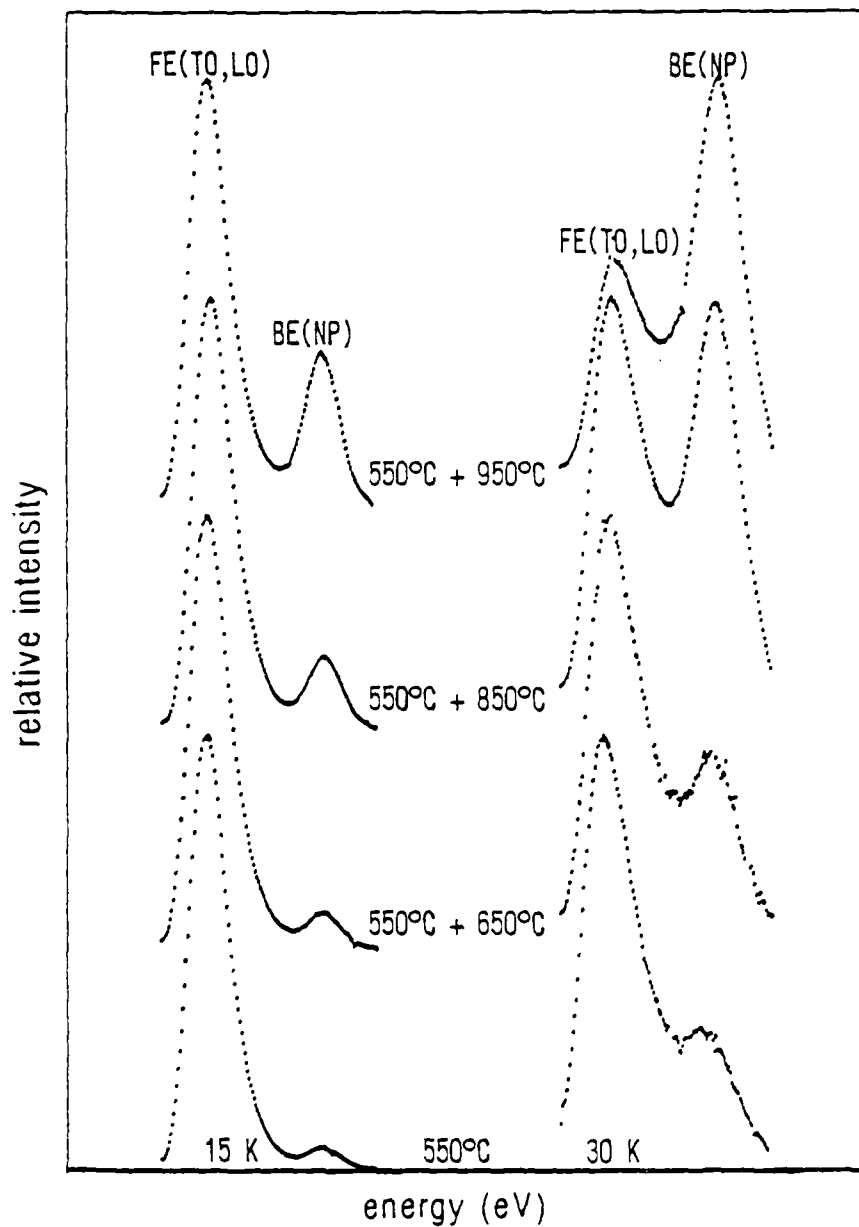


Figure 19. Photoluminescence from Ion Implanted Si:Tl at 15 K and 30 K Showing the BE(NP): FE(TO) Ratios as a Function of Second Anneal Temperature

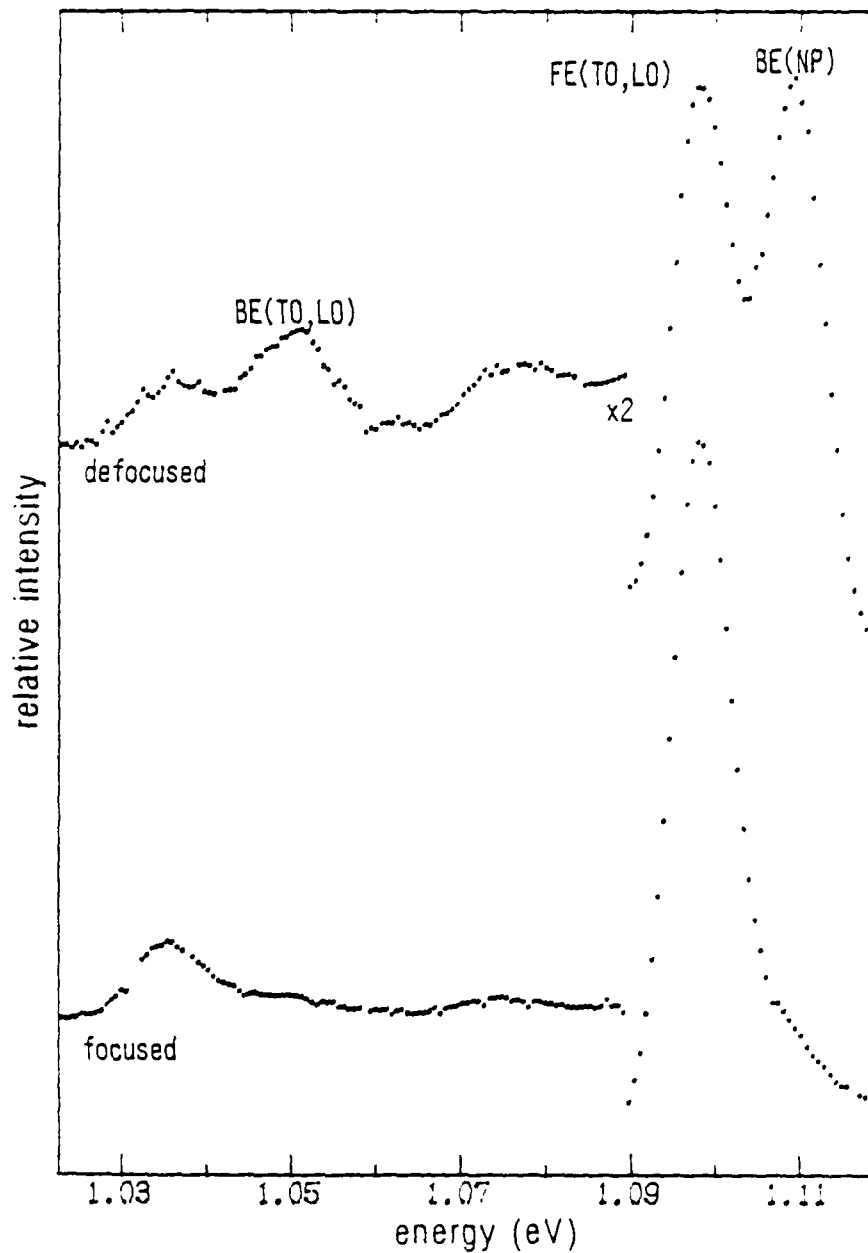


Figure 20. Cathodoluminescence from Single-Step 850C Annealed Si:Tl for a Focused and Defocused Beam. Sample 445 at 24K.

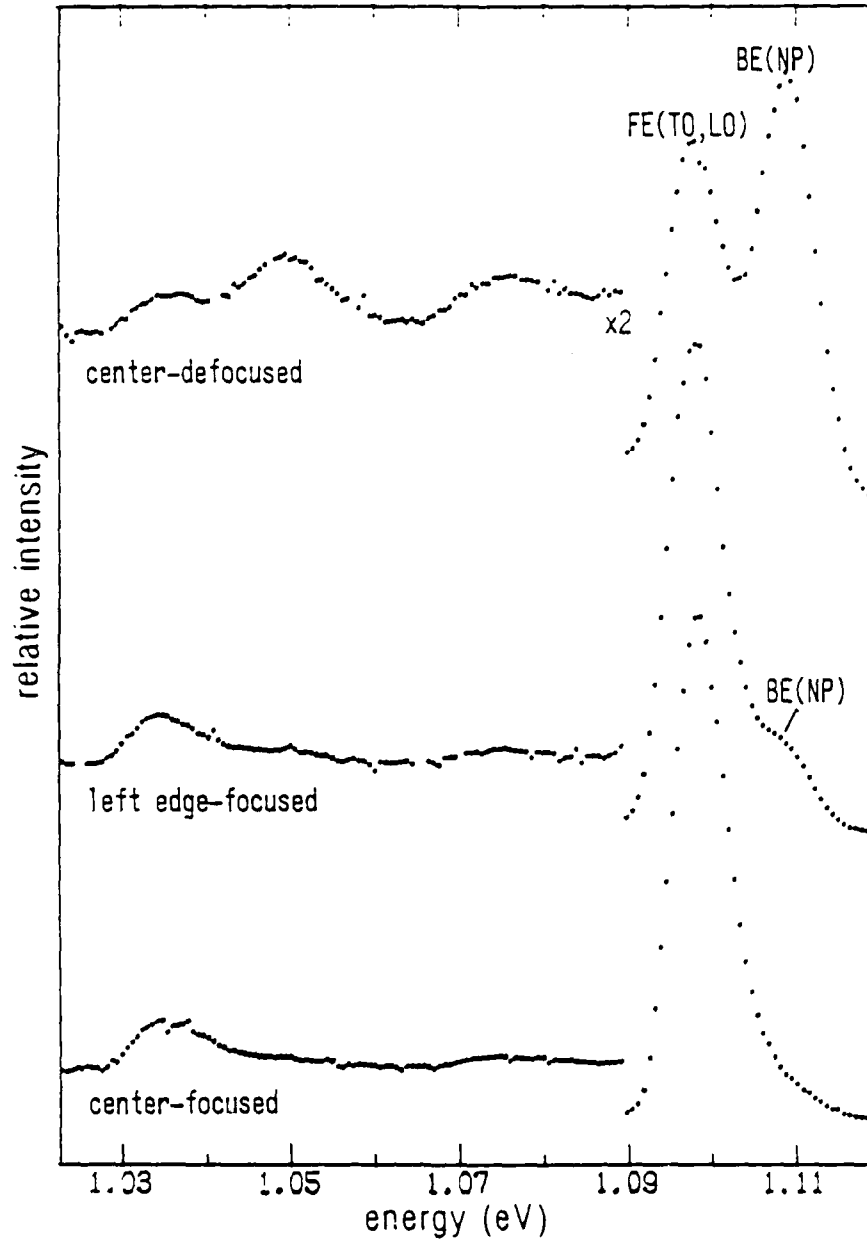


Figure 21. Cathodoluminescence from Single-Step 9500C Annealed Si:Tl for Two Positions and With the Beam Defocused. Sample 446 at 24 K.

single-step anneal samples, the amorphous layer has regrown as polycrystalline Si containing a few polycrystals with high Tl concentrations. This is consistent with previous single-step anneal studies (References 14 and 15).

c. Tl BE Luminescence in Implanted Si

The luminescence from a two-step, 550°C plus 940°C, anneal sample is shown in Figures 22 and 23. The results were the same for (100) and (111) orientations and implant energies of 280 and 560 keV. The FE lines have been labeled after Vouk and Lightowers (Reference 43). The bulk grown data presented in subsection 3b shows an insignificant FE spectra from Si:Tl which implies that the FE spectra observed here is from the substrate. The intensity of the BE luminescence increases relative to the FE luminescence as the temperature increases to above 40 K in contrast to the other group IIIA elements in Si. This is because the localization binding energy,  $E_{bx}$ , of 44.3 meV for Tl is greater than the FE binding energy,  $F_x$ , of 15.4 meV (Reference 43), while for all the other group IIIA elements (Reference 4), is smaller than  $E_x$ . The probability of the FGE being broken up by thermal energy therefore increases faster than for the Tl BE as the temperature increases. This fact makes it easier to see the Tl BE lines in ion implanted layers by using higher luminescence temperatures, e.g. 30 K.

Because the spectra from the ion implanted specimens are dominated by FE lines from the substrate, the lines associated with Tl related recombination are difficult to distinguish (see Figure 23). However, the line shapes of the FE phonon replicas should remain constant with respect to each other since the coupling between the phonons and the emitted radiation remain the same. Therefore, the FE spectrum of the substrate taken at the same sample temperature can be subtracted from the total spectrum to give the underlying BE spectrum. The FE spectra at 15 K normalized to the FE(T0) peak, Figure 7, was subtracted from the ion implanted Tl spectra at 15 K also normalized to the FE(T0) peak, Figure 22. The result is shown in Figure 24. Some artifacts of the FE(T0) are left because of the large relative intensity of this

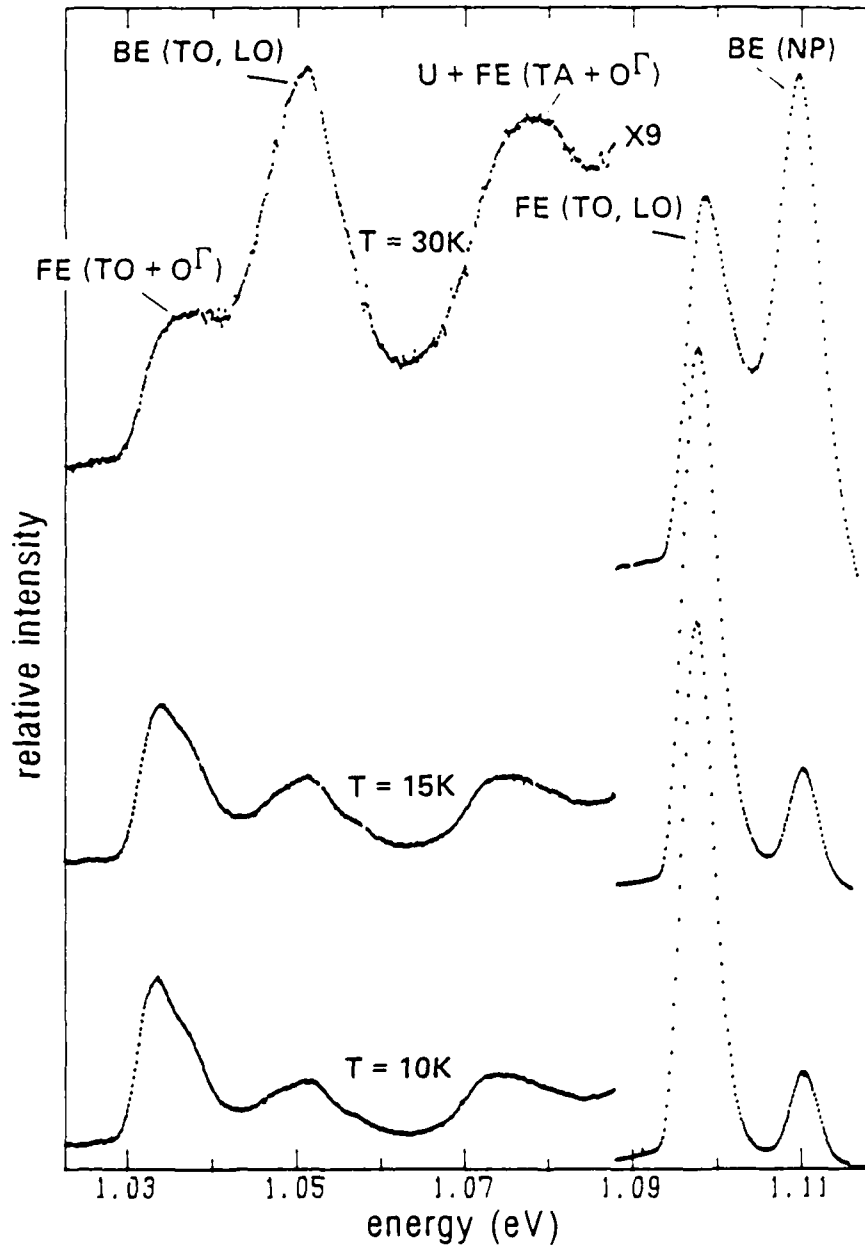


Figure 22. Photoluminescence Spectra of Fully Annealed Silicon Ion Implanted with  $10^{14}$  Tl Ions/cm<sup>2</sup> at 560 keV. Sample 310.

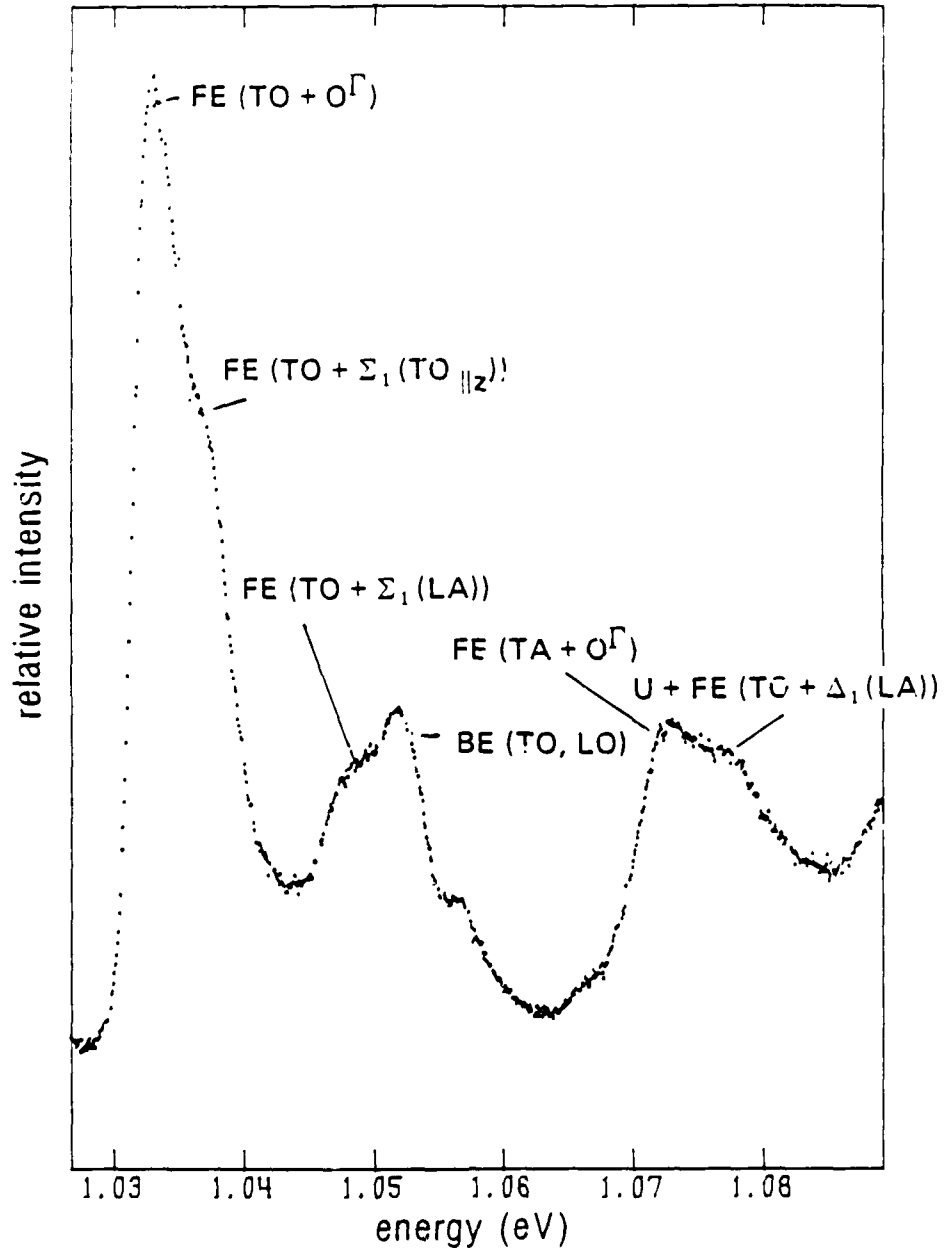


Figure 23. High Resolution Luminescence Spectrum Taken at 10 K of Annealed Silicon Ion Implanted with  $10^{14}$  Ions/cm<sup>2</sup> at 560 keV. Sample 310 (Intensity not Corrected).

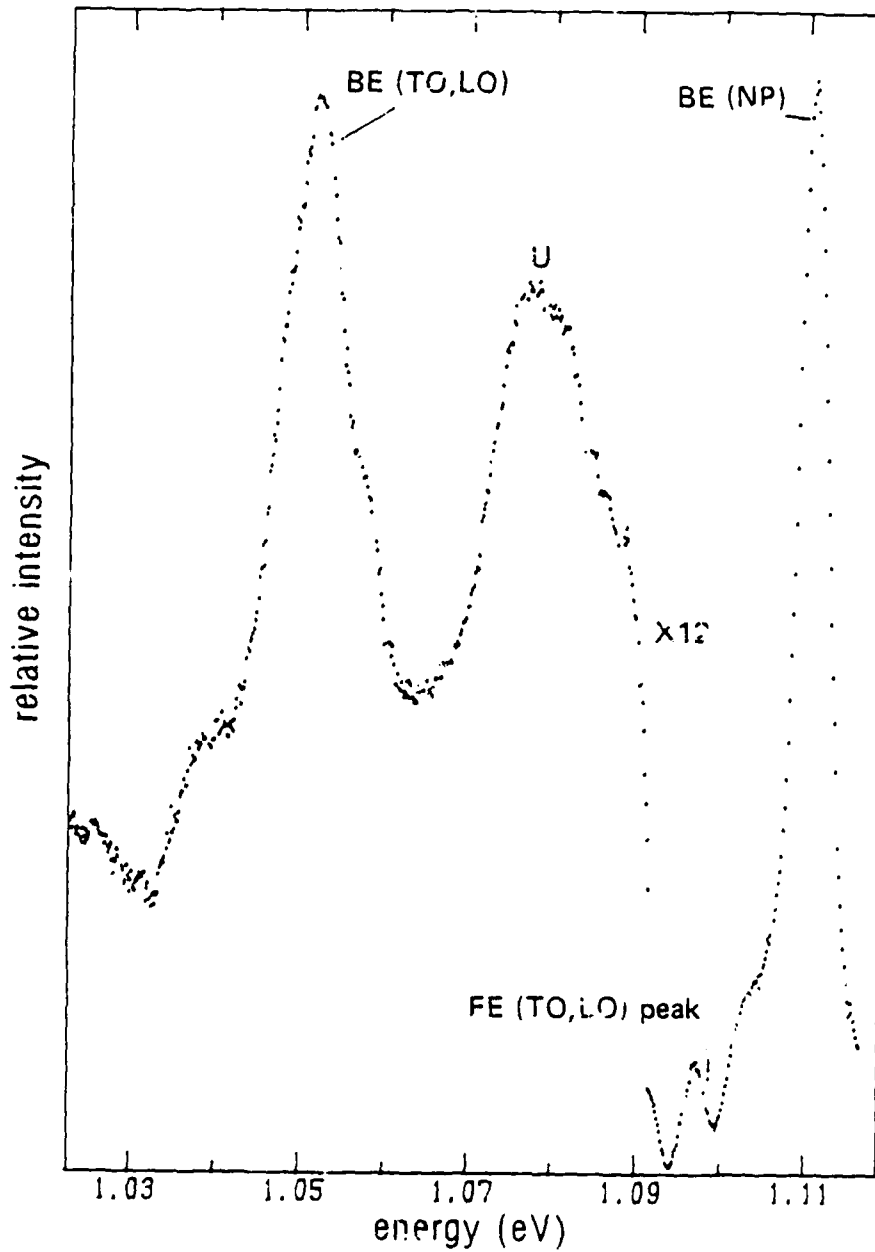


Figure 24. Thallium Associated Luminescence at 15 K from Ion Implanted Silicon. The FE Spectrum of Figure 7 Has Been Subtracted from the Combined FE and BE Spectrum of Figure 24

transition. The BE(TA) is also obscured. Otherwise, the subtracted implanted Tl BE spectra is identical to that of the bulk grown sample (compare Figures 8 and 24); therefore, this proves to be a powerful new technique for studying implants by luminescence.

#### d. BE Excited States

The BE split into four lines as reported by Elloitt (Reference 33) et al. Figure 25 shows the BE lines at temperatures of 8, 15, and 30 K from a (111) sample implanted with  $10^{14}$  Tl ions/cm<sup>2</sup> at 280 keV. Thermalization of the lines is very evident with the relative intensity of the excited states increasing with temperature. The resolution of these four lines was better in the ion implanted samples than in the bulk grown samples. This indicates that qualitatively either the concentration in the implanted samples was higher than in the bulk grown sample or the crystal structure was better.

### 5. COMPARISON WITH PREVIOUS STUDIES

The BE and its phonon replicas, (T<sub>0</sub>, L<sub>0</sub>) and TA, reported in this paper for Si:Tl are similar to those reported for the other group IIIA dopants (References 4 and 23). The relative NP intensity with respect to that of its phonon replicas is greater than for the other group IIIA dopants as expected (References 45 and 52) because of the higher exciton binding energy, 44.3 meV, of Tl. The presence of four lines in the fine structure of the BE(NP) is confirmed (Reference 33). The fact that the fine structure was resolved in implanted Si:Tl indicates the regrown implant layer had a high quality lattice structure.

The new line U does not fit into the pattern of the shallow group IIIA dopants. This line was not reported by Vouk and Lightowers (Reference 4) probably due to its close proximity to the FE(TA + 0) and the EHD(T<sub>0</sub>,L<sub>0</sub>). The line was present in all Tl doped samples, both bulk grown and ion implanted. It was not present in the substrate material. The energy displacement from the BE(NP), 33.9 meV, does not correspond to any of the allowed one or two phonon processes in Si (References 23, 43,

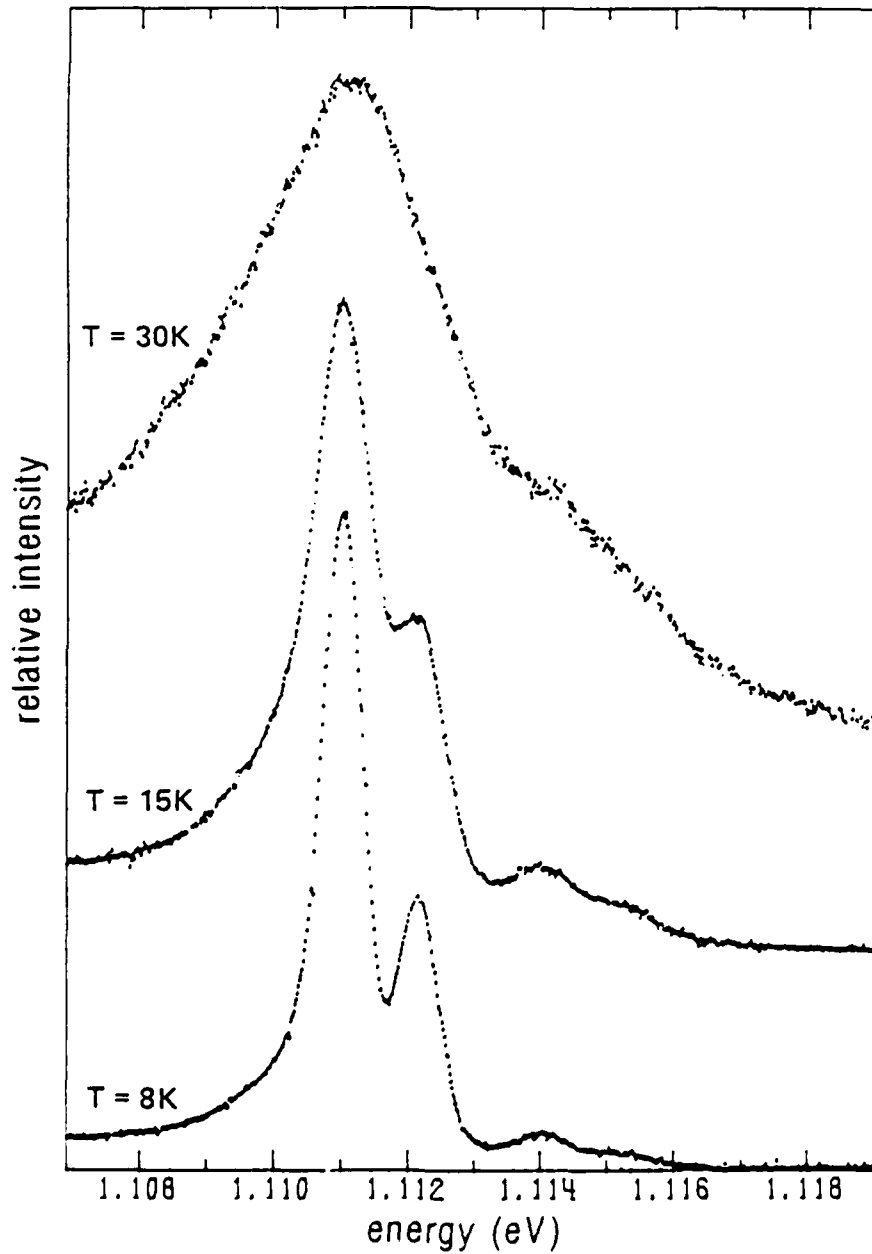


Figure 25. High Resolution Spectra of the BE(NP) Line in Ion Implanted Si:Tl Showing Four Thermalizing Lines. Sample 301 (Intensity not Corrected).

and 53). The relative intensity of U with respect to the BE and its phonon replicas is independent of doping level, excitation power, and temperature. Therefore, U is not a line associated with a multiple bound exciton complex (References 25, 54, 55, and 56) called an impurity associated localized carrier (IALC) by Vouk and Lightowers (Reference 4). Such lines increase in intensity with excitation power and decrease in intensity at higher doping levels with respect to the BE (References 29, 31, 54). It is also not associated with impurity associated EHD (IAEHD) (Reference 4) bands since they disappear with increasing temperature and shift in energy as a function of the doping level. The transition U therefore has the same initial ground state as the BE transition, the neutral acceptor ground state  $A^0$  (References 4 and 23). The U line probably is caused by the same mechanism as the line 4 meV below the BE(NP) in the Si:In spectrum (References 28, 29, and 31) which was first labeled as U1 by Vouk and Lightowers (Reference 4). The ratio of this In related line intensity to the intensities of the In BE lines is also independent of excitation power, dopant concentration, and temperature (References 29 and 31).

Si:Tl is also analogous to Si:In (References 30 and 57) by the presence of the isoelectronic BE lines. Thewalt (Reference 49) et al. suggest the line labeled A in the Si:Tl spectra corresponds to the Si:In line P (also labeled (Reference 4) U2). As with Si:In, the isoelectronic lines in Si:Tl are dependent on crystal growth and vary from sample to sample (Reference 4). The lines were not present in bulk grown samples cs-13 or the ion implanted samples. The identification of these lines is important so that the impurity or defect acting as the recombination center can be eliminated during the growth process; however, ion implantation already provides a method for producing Si:Tl free of these centers.

No EHD's were seen in either the Si:Tl bulk grown or ion implanted material at temperatures down to 4.2 K. Vouk and Lightowers (Reference 4) did report the EHD(TO,LO) in their diffusion doped sample. Shallow impurities in Si do act as condensation centers for EHD's. (References 58 and 59). However, the binding energy for the Tl BE, 44.3

meV, is considerably higher than the EHD work function  $\phi(T) = [8.21 + 5.9 \times 10^{-3}T^2]$  meV (Reference 46) where T is the absolute temperature; therefore, for moderately high Tl doping levels there would not be sufficient free excitons to condense into EHD's. The effect of the high Tl BE localization energy can also be seen in Figure 22 where the BE spectrum persists for higher temperatures than the FE (binding energy = 15.4 meV)(Reference 43) spectrum. This is not the case for the shallower dopants in Si (References 4 and 23).

This is the first luminescence study of radiation damage by heavy ion implants in Si. Previous studies have included the light ions B, P, Ar, As, C, O, Si, and N. The defect lines introduced by these light ion implants were identical to those produced by Tl implants in this study indicating that implant defect lines are independent of the implanted species. Since the defects associated with ion implantation are present for all implants in Si and at least in some cases after laser annealing of Si, it is very important to determine that they are annealed out. This study confirms that luminescence is an ideal tool for accomplishing this.

Luminescence has not been reported before from ion implanted Si:Tl or from any other ion implanted dopant in Si with the exception of Nakashima (Reference 42) et al. They reported the P BE(NP) from a laser annealed P implanted sample as a just visible shoulder on the B BE(NP) from the substrate. However, the results of this study show that the complete BE luminescence spectra can be observed for implanted dopants, and therefore, luminescence is an excellent method for studying implanted dopants in Si.

## SECTION IV

## ELECTRICAL MEASUREMENTS

## 1. SURFACE HALL-EFFECT MEASUREMENTS

In an ion implanted sample, the concentration of dopant atoms varies with depth from the surface. As a result, both the carrier concentration and carrier mobility will vary as functions of depth. Any electrical measurements will then be a weighted average over the depth distribution of implanted ions. Because of this, most studies have attempted to obtain only an empirical relationship for the electrical characteristics of implanted layers (Reference 8); however, the techniques developed in this chapter determine the ionization energy of the implanted dopant by restricting measurements to the compensated region. Precautions are also detailed for insuring the validity of the Hall-effect measurements considering the leakage current through the p-n junction and the ratios of the resistances  $R_a/R_b$ . The sheet carrier concentration temperature profiles can also be used for qualitative comparison between samples.

## a. The Van der Pauw Technique

The van der Pauw (Reference 60) method was used for this study. This technique requires four contacts located anywhere on the periphery of a uniformly thick sample of arbitrary shape. The current is passed through one pair of contacts while the potential difference is measured across the remaining pair of contacts. The six configurations (Reference 61) used are shown in Figure 26. The resistance for each configuration,  $R_x$ , is defined by

$$R_x = \frac{V1 - V2}{I} \quad (5)$$

where  $x = a - f$ . Using configurations (a) and (b), and in analogous fashion using (c) and (d), the resistivity is then given by

$$\rho = \frac{\pi t}{\ln 2} \frac{R_a + R_b}{2} f \left( \frac{R_a}{R_b} \right) \quad (6)$$

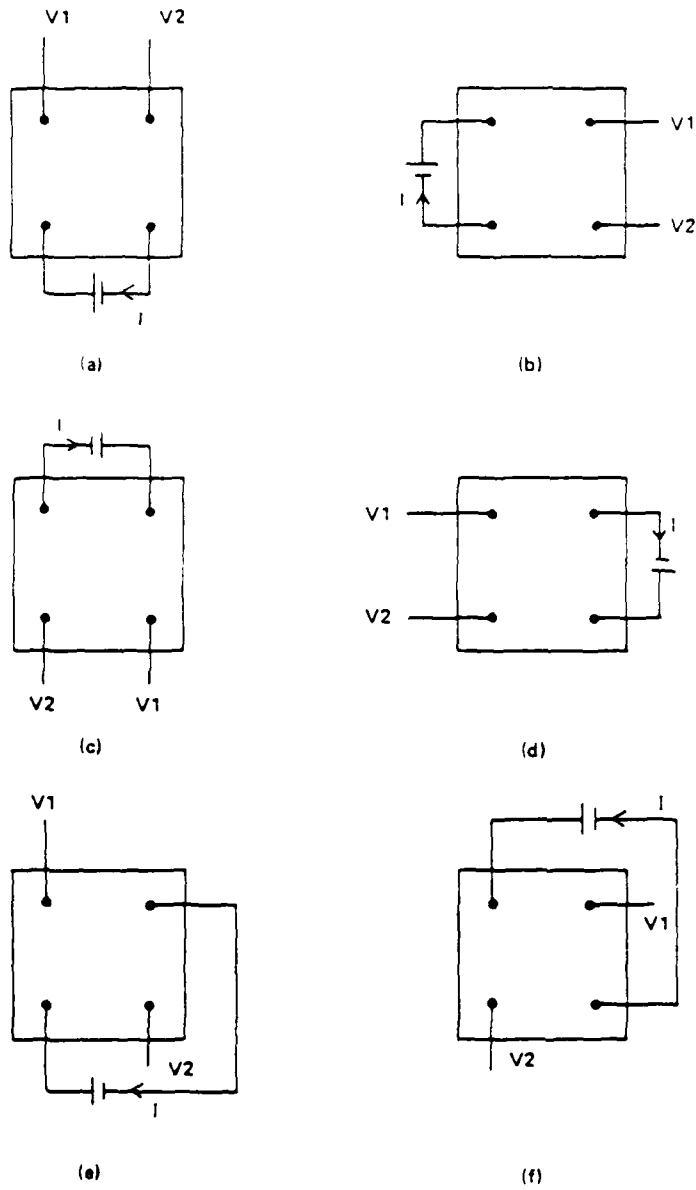


Figure 26. Configurations Used for Van der Pauw Measurements

where  $t$  is the sample thickness and  $f(R_a/R_b)$  is a dimensionless geometrical correction factor (Reference 60) dependent only upon the ratio of  $R_a$  and  $R_b$ :

$$\cosh \left\{ \frac{\frac{2n^2}{t}}{\frac{\frac{R_a}{R_b} - 1}{\frac{R_a}{R_b} + 1}} \right\} = \frac{1}{2} \exp \left( \frac{2n^2}{t} \right) \quad (7)$$

The resistance values  $R_a$  and  $R_b$  are functions of geometry and temperature, but for a symmetrical sample,  $R_a$  and  $R_b$  should be nearly equal and their ratio  $R_a/R_b$  independent of temperature if the sample is homogeneous (Reference 62). The temperature dependence of  $R_a/R_b$  can therefore be used as a figure of merit to determine the sample homogeneity and to indicate the data quality.

Using sample configurations (e) and (f) of Figure 26, the Hall coefficient is given by

$$R_H = \frac{t}{B} \Delta R_e \quad (8)$$

where  $B$  is the applied magnetic field and  $R_e$  is the change in resistance of configuration (e) or (f) when the magnetic field is applied perpendicular to the sample (Reference 60). For an extrinsic p-type semiconductor, the carrier concentration  $p$  is related to the Hall coefficient (Reference 63)

$$p = \frac{r_H}{R_H e} \quad (9)$$

where  $e$  is the charge of the carrier and  $r_H$  is the Hall scattering factor (or  $r$ -factor). The Hall mobility  $\mu_H$  is defined by

$$\mu_H = R_H \sigma = \frac{R_H}{p} \quad (10)$$

where  $\sigma$  is the conductivity and  $\rho$  is the resistivity of the sample. However, the conductivity is related to the conductivity mobility  $\mu$  by

$$\sigma = p e \mu \quad (11)$$

From Equations (9) - (11) we then find the Hall scattering factor

$$r_H = \frac{\mu_H}{\mu} \quad (12)$$

The Hall scattering factor  $r_H$  depends on the nature of the carrier scattering, the band structure of the material, the temperature, and the statistics characterizing the distribution of carrier velocities (Reference 64). The usual practice for implanted layers is to set  $r_H$  equal to unity (Reference 65). However,  $r_H$  has been determined experimentally (Reference 66) for p-type silicon and varies with absolute temperature  $T$  as

$$r_H = .54 + \frac{1.22 \left(\frac{T}{50}\right)}{1 + \left(\frac{T}{50}\right)^2} \quad (13)$$

in the acceptor dopant range of  $10^{16} - 10^{18} \text{ cm}^{-3}$ .

The potential difference in Equation 8 can be affected by galvanomagnetic and thermomagnetic effects other than the Hall-effect (Nernst, Righi-Leduc and Ettinghausen effects) (Reference 67). Except for the Ettinghausen effect, these effects can be eliminated by reversing the field and obtaining an average value for the configurations used in Equations 6 and 8. The Ettinghausen effect is small in silicon because the thermoelectric power is small (Reference 68). Configurations (c), (d), and (f) in Figure 26 are not essential in principle to determine  $\rho$  and  $R_H$ , but they are used for the practical purpose of averaging out any geometrical effects.

Since the dopant concentration does vary with depth in implanted layers, the experimental results from the van der Pauw technique will be an effective resistivity,  $\rho_{\text{eff}}$ , and an effective Hall coefficient,  $R_{\text{Heff}}$ . Therefore, it is only meaningful to speak of sheet measurements where the sheet resistivity, sheet conductivity, sheet Hall coefficient and sheet carrier concentration are defined by

$$\rho_s = \frac{\rho_{\text{eff}}}{t} ; \sigma_s = \frac{1}{\rho_s}$$

$$R_s = \frac{R_{\text{Heff}}}{t}$$

$$P_s = \rho_{\text{eff}} t = \frac{r_H}{R_s e} \quad (14)$$

Petritz (Reference 69) has shown by circuit analysis and also by a derivation from Boltzmann's equation that the sheet Hall coefficient is given by

$$R_s = \frac{\int_0^t e p(x) r_H u^2(x) dx}{\left[ \int_0^t e p(x) u(x) dx \right]^2} \quad (15)$$

where  $p(x)$  and  $\rho(x)$  are functions of depth from the surface, and we have assumed there are no circulating currents.

The effective sheet carrier concentration is then given by

$$p_s = \frac{r_H}{e} \frac{\left[ \int_0^t e p(x) u(x) dx \right]^2}{\int_0^t e p(x) r_H u^2(x) dx} \quad (16)$$

or

$$P_s = \frac{\left[ \int_0^t p(x) u(x) dx \right]^2}{\int_0^t p(x) u^2(x) dx}$$

if we assume that  $r_H$  does not vary with depth. This value may differ from the actual sheet carrier concentration which is defined by

$$P = p t = \int_0^t p(x) dx$$

The sheet conductivity is given by (Reference 69)

$$\sigma_s = \sigma_{\text{eff}} t = \int_0^t e p(x) u(x) dx \quad (17)$$

and therefore the Hall mobility of the implanted layer is

$$\mu_{H_s} = R_s \sigma_s = R_{\text{Heff}} \sigma_{\text{eff}} = \frac{\int_0^t p(x) u^2(x) \tau_H dx}{\int_0^t p(x) u(x) dx} \quad (18)$$

b. The Reverse-Biased p-n Junction

In order to measure the electrical properties of the implanted layer, the implanted region must be isolated from the substrate. Isolation can be accomplished by using a substrate of very high resistivity or by forming a p-n junction using a substrate material of opposite type to the implanted layer (Reference 8). Because of its very deep acceptor level in Si, Tl doped Si has a high resistivity at measurement temperatures. For this reason, the high resistivity approach is impractical, and a p-n junction was therefore used for electrical isolation in this study.

The van der Pauw shape was cut out of an implanted wafer with an ultrasonic cutter as opposed to the common mesa etching procedure. In the mesa etching technique, the implanted layer is etched from the substrate except in the van der Pauw pattern (References 8 and 68) which has the disadvantage of allowing surface currents to flow through the substrate material around the periphery of the mesa structure. In the ultrasonically cut samples, the only possible path for current flow is through the p-n junction which can be measured. An ohmic contact was placed in the center of the back of the substrate in order to identify the existence of a p-n junction (Reference 68) to reverse-bias the junction (Reference 70) and to monitor any leakage current.

The backside contact was at the same potential as the positive current contact, therefore preventing leakage current from crossing the p-n junction between these contacts. The junction between the negative current contact was reverse biased by the potential (1 volt) applied to supply the measurement current (see Figure 27). The leakage current through the backside contact was monitored during all Hall-effect measurements. This precaution has not been previously reported. A region of validity for the data was established using leakage current as a figure of merit. Myers (Reference 71) states that as a "rule of thumb", the Hall-effect data should be considered valid when the total leakage current is less than 2% of the sample current through the implant layer. Mayer (Reference 8) et al. state that leakage current should be less than 5% of the measurement current. Data was used quantitatively in this study only if the leakage current was less than 1% of the measurement current.

The quality of the p-n junction is dependent on the anneal temperature of the implanted sample. Michel et al. (Reference 72) found that the leakage current of P, As, and B implants in silicon was strongly dependent on the anneal temperature of the sample. They found that a minimum anneal temperature of 900°C for 30 min is required to produce low leakage ion-implanted junctions.

Since the measurement current does not flow through the depletion region, the extent of the depletion region into the implant layer will affect the electrical measurements (Reference 73). The depletion region will however extend deeper into the more lightly doped region (Reference 74). For this reason, 70 ohm-cm n-type material ( $N_d = 6 \times 10^{13} \text{ cm}^{-3}$ ) was used as a substrate. The depletion region therefore extended primarily into the substrate side. For shallow implants, the surface states of the silicon may strongly affect the electrical measurements (References 73 and 75). In this work, deep implants (280 and 560 keV) were used so that surface effects would have negligible effects on the electrical measurements.

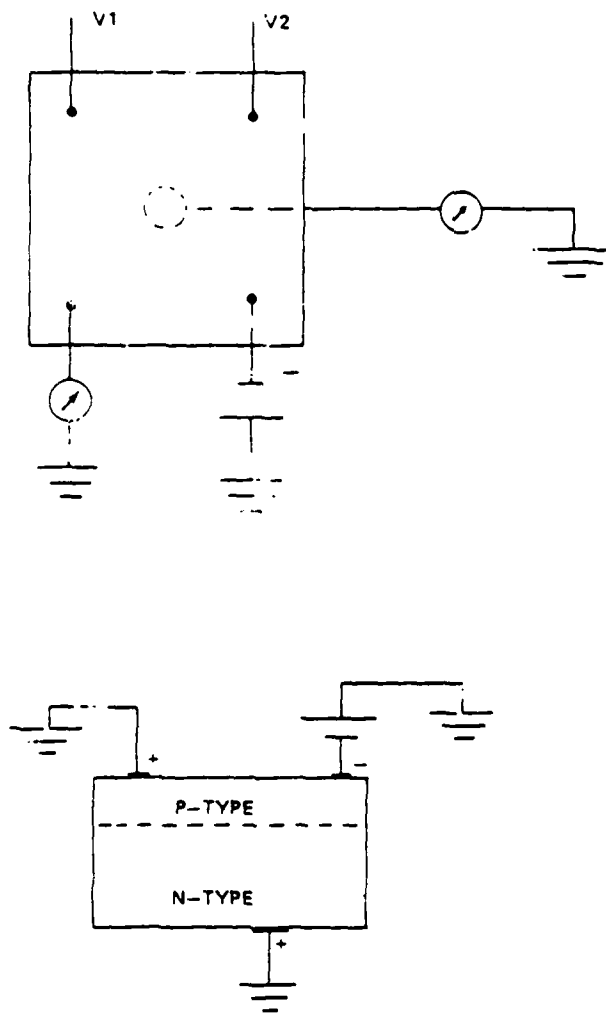


Figure 27. Electrical Connections for a Reverse-biased Implant Layer

## c. Measurements as a Function of Temperature

For a uniformly thick sample, the carrier concentration  $p$  can be measured as a function of temperature using Hall-effect measurements and Equation 9. At low temperatures, a logarithmic plot of  $p$  versus  $\frac{1}{T}$  yields (after correcting for the temperature dependence of  $N_V$ ) the value of the activation energy  $E_A$  (Reference 76). However, for implanted layers the variation in dopant concentration with depth makes the accurate determination of the ionization energy much more difficult (Reference 8). This is evident from the temperature dependence of the hole carrier concentration which is now discussed.

For a p-type semiconductor, the density of hole carriers  $p$  is given by

$$\frac{p(p+N_d)}{N_a - N_d - p} = \frac{N_V}{g} e^{-E_a/kT} = \beta(T) \quad (19)$$

where  $N_V$  is the effective density of valence band states,  $g$  is the degeneracy of the acceptor,  $N_a$  is the density of acceptors, and  $N_d$  is the density of compensating donors (Reference 77). Boltzmann statistics have been assumed. At high temperatures  $p(T)$  tends to the exhaustion value  $p(T) \rightarrow N_a - N_d$ .

As the temperature is lowered (Reference 70), the semiconductor goes through the noncompensated region where  $N_d < p(T) < N_a$ . Equation 19 can be approximated by

$$p(T) = \left( \frac{N_V N_a}{g} \right)^{1/2} e^{-E_a/2kT} \quad (20)$$

At the lowest temperatures, the sample is in the compensated region where  $p(T) < N_d < N_a$  and Equation 19 can be approximated by

$$p(T) = \frac{N_V}{g} \frac{(N_a - N_d)}{N_d} e^{-E_a/kT} \quad (21)$$

The effective density of states is given by

$$N_V = 2 \left( \frac{2\pi m_h^* kT}{h^2} \right)^{3/2} \quad (22)$$

where  $m_h^*$  is the carrier concentration effective mass (Reference 8) for holes. Therefore, a semilogarithmic plot of  $T^{-3/2}p(T)$  versus  $\frac{1}{T}$  changes slope from  $(-\frac{E_a}{2k})$  to  $(-\frac{E_a}{k})$  as  $p(T)$  falls through the value  $N_d$ . The location of this transition is determined not only by  $N_d$  but also by  $N_a$  since the value of  $p(T)$  is dependent on  $N_a$ . The transition region is characterized by a "knee" between the two slopes.

The measured sheet carrier concentration,  $P_s$ , is given in terms of integrals of  $p(x,T)$  as expressed by Equation 16. When  $N_d$  and  $N_a$  vary with depth, the transition in slope or "knee" will be in a different temperature region for each layer. Then the integral of these layers, Equation 16, will not have a slope of  $(-\frac{E_a}{2k})$  or  $(-\frac{E_a}{k})$  but a mixture of the two. Therefore, the semilogarithmic plot of  $T^{-3/2}P_s$  versus  $1/T$  will not produce a linear relation. However, this difficulty can be overcome if we consider only a temperature region where all layers will be in the compensated regions.

In the compensated region where  $p(T) < N_d < N_a$  Equation 21 is given by

$$p(T) = \beta \frac{(N_a - N_d)}{N_d} \quad (23)$$

where  $\beta(T) = \frac{N_V}{g} \exp(\frac{E_a}{kT})$ . Equation 19 can be solved exactly to give

$$p = \frac{-(N_d + \beta) + \sqrt{(N_d + \beta)^2 + 4(N_a - N_d)\beta}}{2} \quad (24)$$

Equations 23 and 24 have been plotted in Figure 28 for  $N_d = 6.0 \times 10^{13} \text{ cm}^{-3}$ ;  $N_a = 10^{14}, 10^{16}, \text{ and } 10^{18} \text{ cm}^{-3}$ ; and  $E_a = 0.25 \text{ eV}$ . From these plots, only data for temperatures less than 165 K were used to determine  $E_a$ .  $N_d$  may be larger than the constant doping level of the substrate if compensating centers are introduced by ion implantation. However, the influence of these centers appears to be removed by anneal temperatures of  $900^\circ\text{C}$  (Reference 68). If  $N_d$  were larger due to defect levels, the compensated region would extend to even higher temperatures.

Substituting Equation 23 into Equation 16, we get for the sheet concentration

$$P_s = \frac{\left[ \int_0^t \frac{\beta (N_a(x) - N_d(x))}{N_a(x)} u(x) dx \right]^2}{\int_0^t \frac{\beta (N_a(x) - N_d(x))}{N_d(x)} u^2(x) dx} \quad (25)$$

If we assume the mobility is separable into functions of temperature and depth

$$u(x, T) = h(x) C(T),$$

then

$$P_s = \beta H(x) \quad (26)$$

where

$$H(x) = \frac{\left[ \int_0^t \frac{N_a(x) - N_d(x)}{N_d(x)} h(x) dx \right]^2}{\int_0^t \frac{N_a(x) - N_d(x)}{N_d(x)} h^2(x) dx}$$

From Equation 22 and 26 we then have

$$\frac{d}{d(1/T)} \ln \left( \frac{P_s}{T^{3/2}} \right) = -E_a/k$$

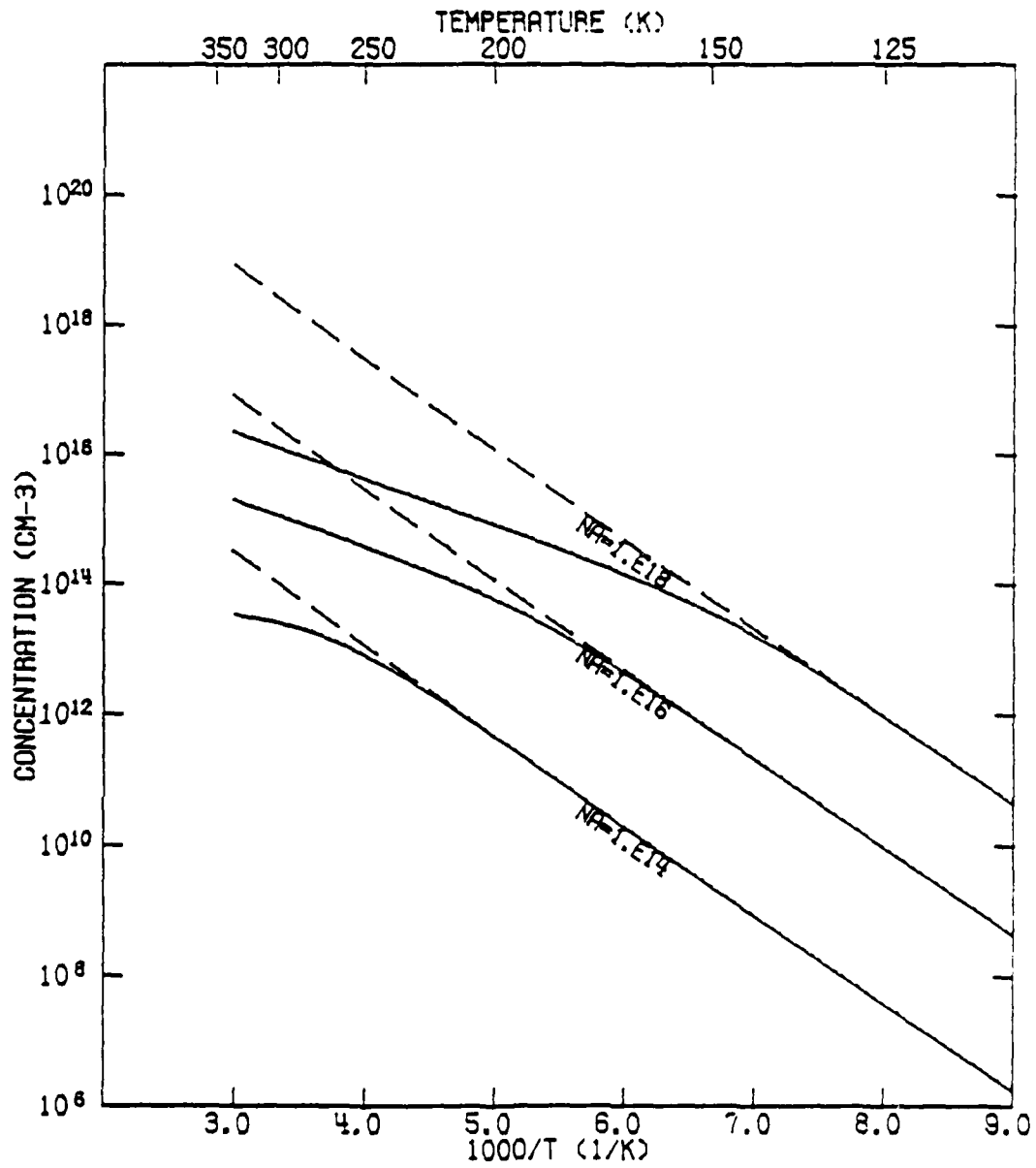


Figure 28. Computer Plots Generated Using Equation 23 and Equation 24, Dashed and Solid Lines, Respectively.

The activation energy of the implanted layer is then given by

$$E_a = -k \frac{d}{d(1/T)} \ln \left( \frac{P_s}{T^{3/2}} \right) \quad (27)$$

As a check, the sheet conductivity,  $\sigma_s$ , can also be used to determine the activation energy. The calculation of  $\sigma_s$ , from the van der Pauw data, Equation 5, is independent of the determination of the sheet concentration  $P_s$ , Equation 9. Substituting Equation 23 into Equation 17, we have for the compensated region:

$$\sigma_s = e \beta \int_0^t \frac{N_a(x) - N_d(x)}{N_a(x)} \mu(x) dx \quad (28)$$

This quantity is dominated by the region in which  $N_a(x) \gg N_d(x)$ , and therefore  $\mu(x)$  will be reasonably uniform over this region. The effect of  $\mu(x)$  in the low dopant concentration tail region can be neglected in contrast to its effect on Equation 16. If the temperature dependence of  $\mu(x)$  is assumed to be  $T^{-n}$ , then the activation energy is given by

$$E_a = -k \frac{d}{d(1/T)} \ln (T^{n-3/2} \sigma_s) \quad (29)$$

Similarly in the noncompensated region, from Equation 20 the activation energy will be given by

$$E_a = -2k \frac{d}{d(1/T)} \ln (T^{n-4/3} \sigma_s) \quad (30)$$

The knee between these two slopes will then identify the compensated region.

## d. Previous Electrical Measurements

Other investigators have studied the electrical properties of Si:Tl and of ion implants in Si. The review article by Johansson and Mayer (Reference 68) and the book by Mayer et al. (Reference 8) served as the basis for much of the procedure in this study. They note only five reports of temperature dependent Hall-effect measurements on implanted silicon prior to 1970. The past decade has seen the addition of only a few temperature dependent studies of ion-implants in silicon. Thallium doped Si has been studied even less because of the low solubility of Tl in Si as well as the large activation energy.

Shulman (Reference 6) published the first determination of the ionization energy of Si:Tl. He made potentiometric resistivity measurements on a Hall bar cut from a crystal grown by dropping Tl pellets into the melt. By plotting conductivity versus  $\frac{1}{T}$  he determined a value of 0.26 eV. Similarly, Sclar (Reference 1) measured the resistance of a vertical float zone Tl doped crystal with a resistance calibrated electrometer. His plot of resistance versus  $\frac{1}{T}$  yielded an ionization energy of 0.21 eV. In an earlier publication (Reference 7), he reported a value of 0.23 eV.

Hall-effect measurements on ion implanted Si:Tl by Baron et al. (Reference 79) were largely unsuccessful because of the high resistivities encountered. The implants were made at an energy of only 40 keV with the substrate held at 450°C. For anneal temperatures between 500°C and 780°C, the implanted region was found to be n-type. For higher temperature anneals, the p-type layer had a carrier concentration of about  $10^{11} \text{ cm}^{-2}$  at room temperature. More recently, Brotherton and Gill (Reference 80) used thermal emission-rate measurements on implanted Si:Tl to determine a value of 0.24 eV.

The ionization energies of implanted layers can be determined from the sheet concentration as a function of temperature. One problem in doing this has been previously described, the variation with depth of the dopant concentration. Another problem is that for heavier dopant species at energies of less than 100 keV, degenerate doping conditions are produced for doping levels as low as  $10^{13} \text{ ions/cm}^2$  (Reference 68).

The carrier concentration then becomes nearly independent of temperature. Because of these problems, only a limited number of attempts have been made to measure the ionization energy of implants in silicon which have resulted in the following dopant ionization energies: boron (0.045 eV (Reference 81), 0.052 eV (Reference 82)), phosphorus (0.045 eV (Reference 82), 0.027 eV (Reference 83)), lithium (0.029 eV (Reference 83)), nitrogen (0.045 eV (Reference 84)), sodium (0.032 eV (Reference 85), 0.035-0.038 eV (Reference 86)), indium (0.160 eV (Reference 75)), and tellurium (0.140 eV (Reference 75)). Two additional studies have been done on temperature dependent Hall-effect measurements in phosphorus implanted silicon from which the ionization energy was not determined.

MacDonald and Galster (Reference 87)) studied P implanted into Si at 400 keV. They determined the sheet concentration versus  $\frac{1}{T}$  both experimentally and theoretically. The sheet concentration was calculated from carrier statistics for nondegenerate n-type semiconductors, the L.S.S. theory for donor distribution, and scattering equations for mobility as a function of dopant concentration. A well defined minimum (a drop to  $\frac{1}{6}$ ) in the sheet concentration was found both experimentally and theoretically between 50 K and 250 K. They (Reference 87) attributed this dip to high mobility in the tail region of the implant distribution dominating the integral in the denominator of Equation 16.

In a similar study of P implants, Wagner and Burkhardt (Reference 65) also found a linear region in their semilog plot of sheet concentration versus temperature below 50 K and a dip between 50 and 300 K. They concluded that the measured sheet concentration was equal to the actual sheet concentration for temperatures below 50 K. They also concluded that it is impossible to get true quantitative information from Hall-effect measurements made only at room temperature on implanted P because of the dip in sheet concentration.

The more popular use of Hall-effect measurements on implants in silicon has been to study the anneal properties using room temperature only measurements. The result given above (References 65 and 87) indicate that these studies are of questionable value because of the effect of the varying dopant concentration with depth on the measured sheet concentration at room temperature. Nevertheless, the annealing characteristics of the following implanted dopants in silicon have been studied with room temperature only Hall-effect measurements: boron (References 64, 79, 88, 90 and 91), aluminum (References 79 and 88) gallium (References 79 and 92), indium (References 93), phosphorus (References 64, 88, 90, 94 and 95), arsenic (References 71, 79, 95 and 96), antimony (References 79 and 92), bismuth (Reference 79), selenium (Reference 97), tellurium (Reference 97), zinc (Reference 97), and cadmium (Reference 97).

The effects of the changing dopant concentration with depth can be eliminated by using differential Hall-effect techniques (References 8, 68 and 79). Sheet concentration measurement are made after each repetitive anodic etching of the implant layer. If the layers removed are thin enough so that the dopant concentration can be assumed uniform, the carrier concentration can be determined as a function of depth. This technique does have the disadvantage of introducing large errors. It is difficult to etch off uniform layers and also to measure the thickness removed accurately. Since differences are taken between sheet resistivities for consecutive etchings, the carrier concentration is extremely sensitive to errors in these measurements (Reference 71). The following dopants have been studied by differential Hall-effect at room temperature: boron (References 98 and 99) aluminum (Reference 79) gallium (Reference 100), phosphorus (References 94, 98, 101, 102, 103, and 104). Also, Pashley (Reference 75) has done temperature dependent differential Hall-effect measurements on indium and tellurium implants and determined their ionization energies.

## 2. THE VAN DER PAUW SYSTEM

Hall measurements were made using a guarded dc Hall apparatus designed for high resistance ( $\approx 10^{13}$  ohm) measurements. The guarding system has been previously described (Reference 61). A six position switching unit automatically gave the configurations shown in Figure 26. The current in each configuration was also reversed by the unit to give an average value for that configuration. A fifth guarded lead was connected to the substrate as shown in Figure 27 to measure the leakage current through the p-n junction. An applied voltage of 1 volt and an applied magnetic field of 1 kG were used for all measurements.

The sample was clamped by a spring clip against a BeO holder fastened on the copper cold finger of a heat exchange, gas flow liquid helium, variable-temperature cryostat. The sample temperature was monitored with a calibrated Lake Shore Cryotronics model DT-500 KL silicon diode which contacted the BeO holder. The temperature was controlled by an Artronix unit with a platinum sensor which varied the flow of current to heating coils wrapped around the copper block on which the sample was mounted.

## 3. HALL-EFFECT RESULTS

### Substrate Donor Concentration

The substrate material used was 70 ohm-cm phosphorus doped silicon procured from General Diode Corporation. Hall measurements were made on van der Pauw samples cut from an unimplanted wafer. The concentrations of donors and acceptors and the donor ionization energy were determined by a non-linear least-squares fit (Reference 107) to the charge balance equation

$$n + N_A = \frac{N_d}{1 + n \left(\frac{2}{N_C}\right) \exp\left(\frac{E_i}{kT}\right)} \quad (31)$$

where  $n$  is the carrier concentration,  $N_A$  is the acceptor concentration,  $N_D$  is the donor concentration,  $E_i$  is the ionization energy of the phosphorus and  $N_C$  is the density of states of the conduction band. The concentration with the computer fit are plotted versus  $\frac{1}{T}$  in Figure 29 for Sample 287, and the results are summarized in Table 4 for three samples.

b. Figures of Merit

The leakage current through the p-n junction into the substrate was monitored for all Hall-effect measurements. These measurements along with the ratios  $R_a/R_b$  were used to establish the validity of the measurements. The  $R_a/R_b$  ratio is defined in Equations 6 and 7 where  $R_a$  and  $R_b$  are the resistances measured using configurations (a) and (b) of Figure 26. For all the data, the following sequence was followed.  $R_a$  and  $R_b$  were measured as shown in Figure 26, and then the same configurations were again measured with the current direction reversed.  $R_c$  and  $R_d$  were measured with positive and reverse current instead of  $R_a$  and  $R_b$  at every other temperature point to insure that the geometry did not influence the results. The leakage current into the substrate was also measured at each of these sample configurations and directions of current flow. The 15 samples measured are listed in Table 1, page 10. The maximum leakage current as a percentage of the measurement current in the temperature range 130-200 K is given for each sample

TABLE 4. SUBSTRATE CONCENTRATIONS

Sample	Donor Concentration ( $\text{cm}^{-3}$ )	Donor Ionization Energy (eV)	Acceptor Concentration ( $\text{cm}^{-3}$ )
285	$5.83 \times 10^{13}$	0.0452	$1.76 \times 10^{13}$
286	$6.76 \times 10^{13}$	0.0447	$2.31 \times 10^{13}$
287	$5.81 \times 10^{13}$	0.0451	$1.81 \times 10^{13}$
Mean	$6.13 \times 10^{13}$	0.0450	$1.96 \times 10^{13}$

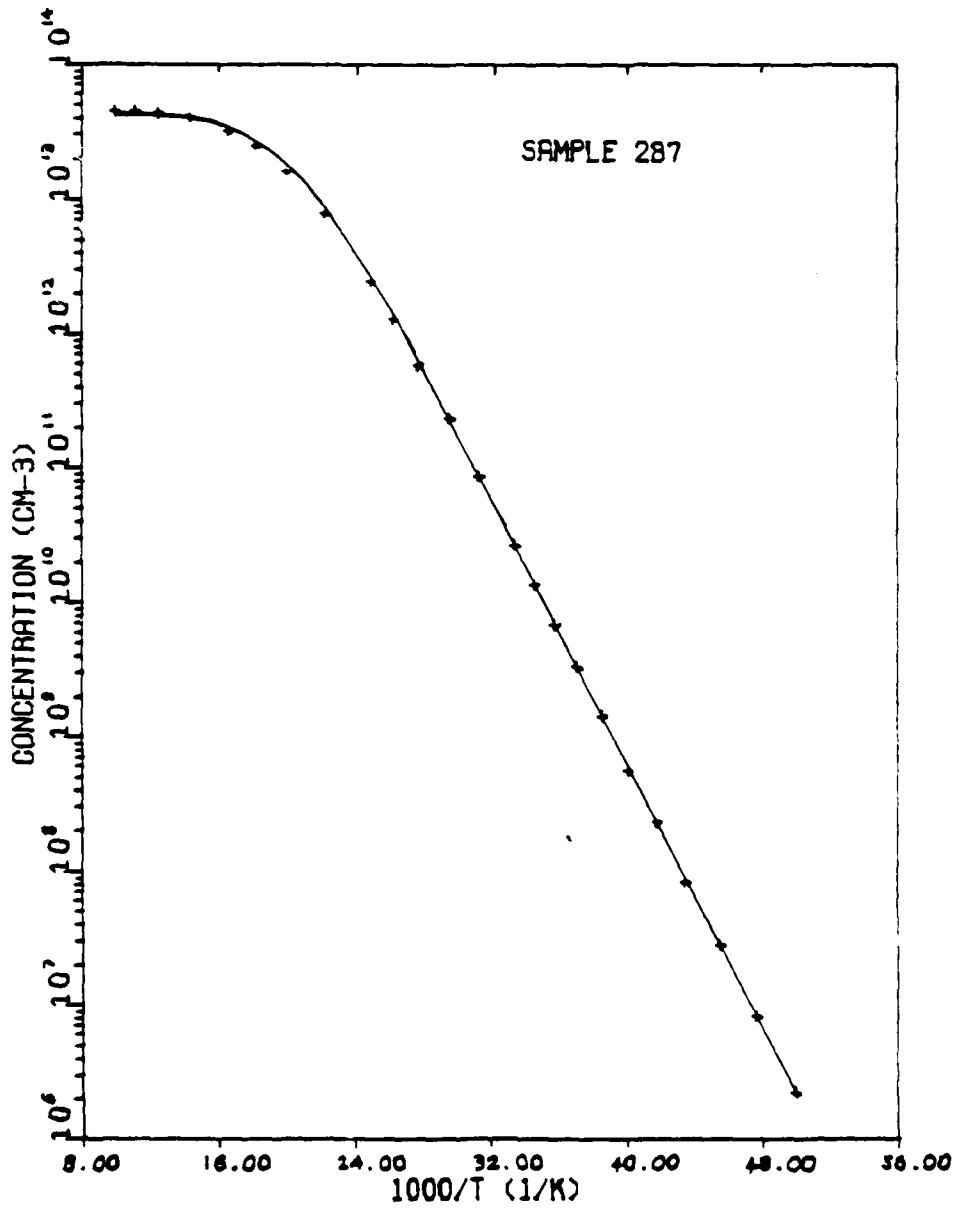


Figure 29. Carrier Concentration of the Substrate Including the Charge Balance Equation Fit, Solid Line

The leakage current as a percentage of the measurement current is plotted versus inverse absolute temperature in Figure 30 for a good sample and in Figure 31 for a leaky sample. Four points are shown at each temperature because a leakage current percentage was measured for configurations (a) and (b) of Figure 26 with both forward and reverse currents. Sample 532 shows a very large leakage current in the range of 10-24 percent of the measurement current which clearly indicates that this sample cannot be used for quantitative results. Only data points with a leakage current less than one percent of the measurement current were considered for quantitative results.

The leakage current (not as a percentage) for the same two samples versus inverse temperature is plotted in Figures 32 and 33. The four values at each temperature correspond to those of Figures 30 and 31. At temperatures above 200 K, the leakage current increased as the temperature was raised until it was larger than the current through the implant layer. As a result, the samples took on the n-type Hall-effect characteristic of the substrate at temperatures above about 360 K.

Figures 30 and 31 also give the ratios  $R_a/R_b$  for positive and negative current alternately with the ratios  $R_c/R_d$  at every other temperature point. The ratios are normalized to their mean value for each sample. Since  $R_a/R_b$  should be a function of geometry only (see subsection 1a), data can be considered valid only in temperature regions where  $R_a/R_b$  remains nearly constant. Clearly sample 532 does not satisfy this criterion. Sample 526 was rejected for quantitative results because its  $R_a/R_b$  ratio was not constant even though its leakage current was less than one percent of the measurement current. Sample 457 is a marginal sample for quantitative results because of the variation in its  $R_a/R_b$  ratio. Only three samples (450, 457, and 471) satisfied the criteria for leakage current and  $R_a/R_b$  ratio.

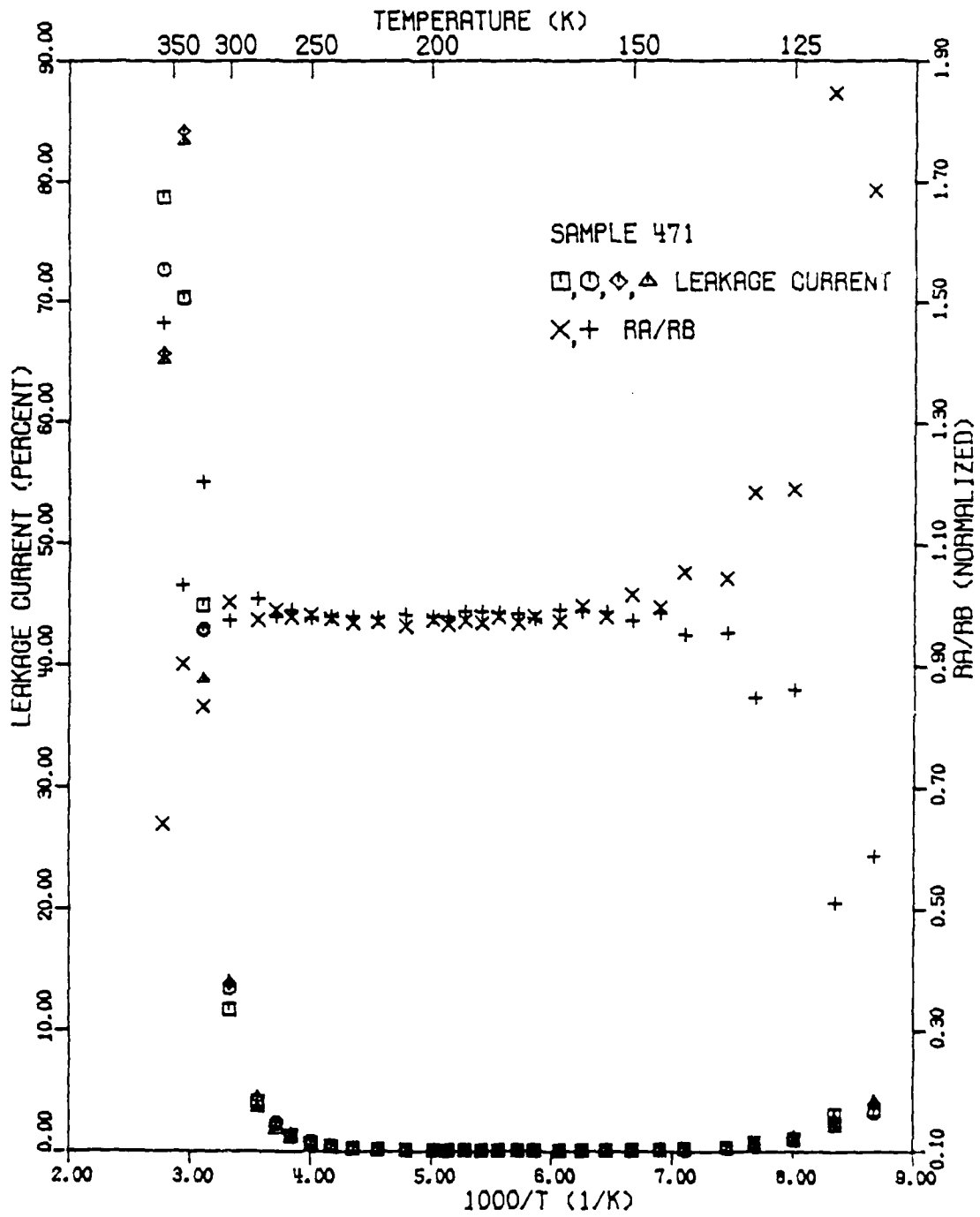


Figure 30. Leakage Current Percent and  $R_a/R_b$  Values for a Good Sample

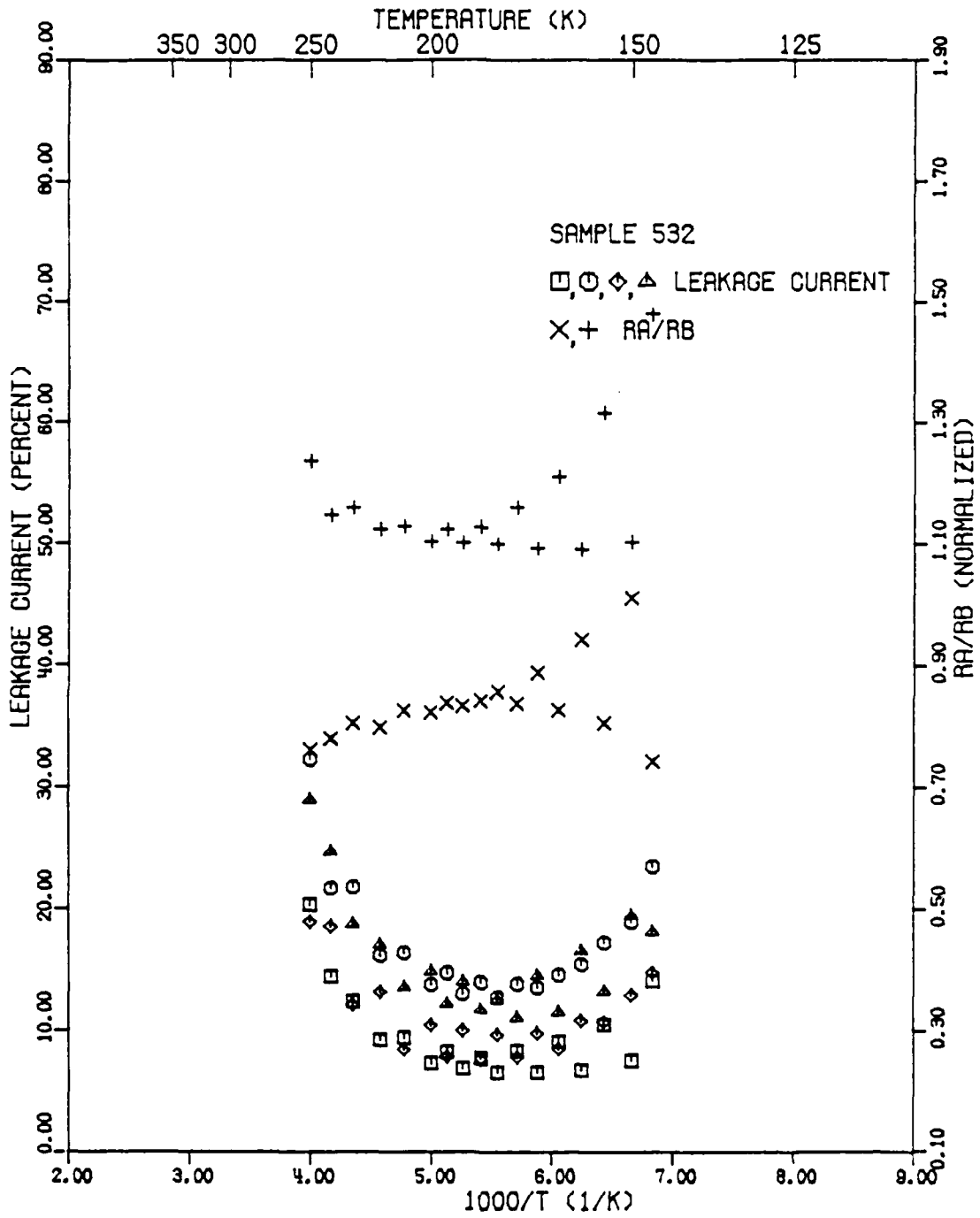


Figure 31. Leakage Current Percent and  $R_a/R_b$  Values for a Leaky Sample

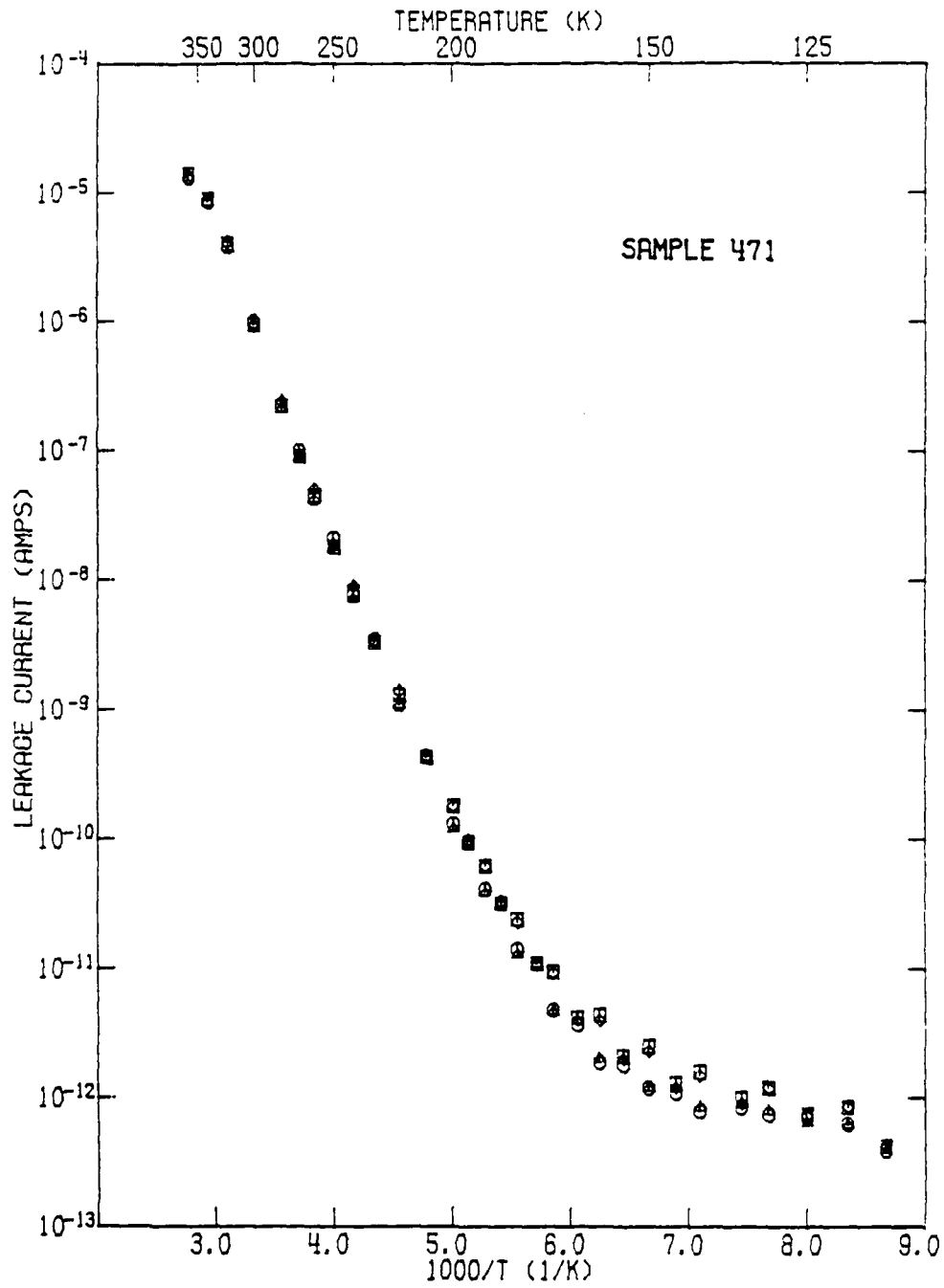


Figure 32. Leakage Current for a Good Sample

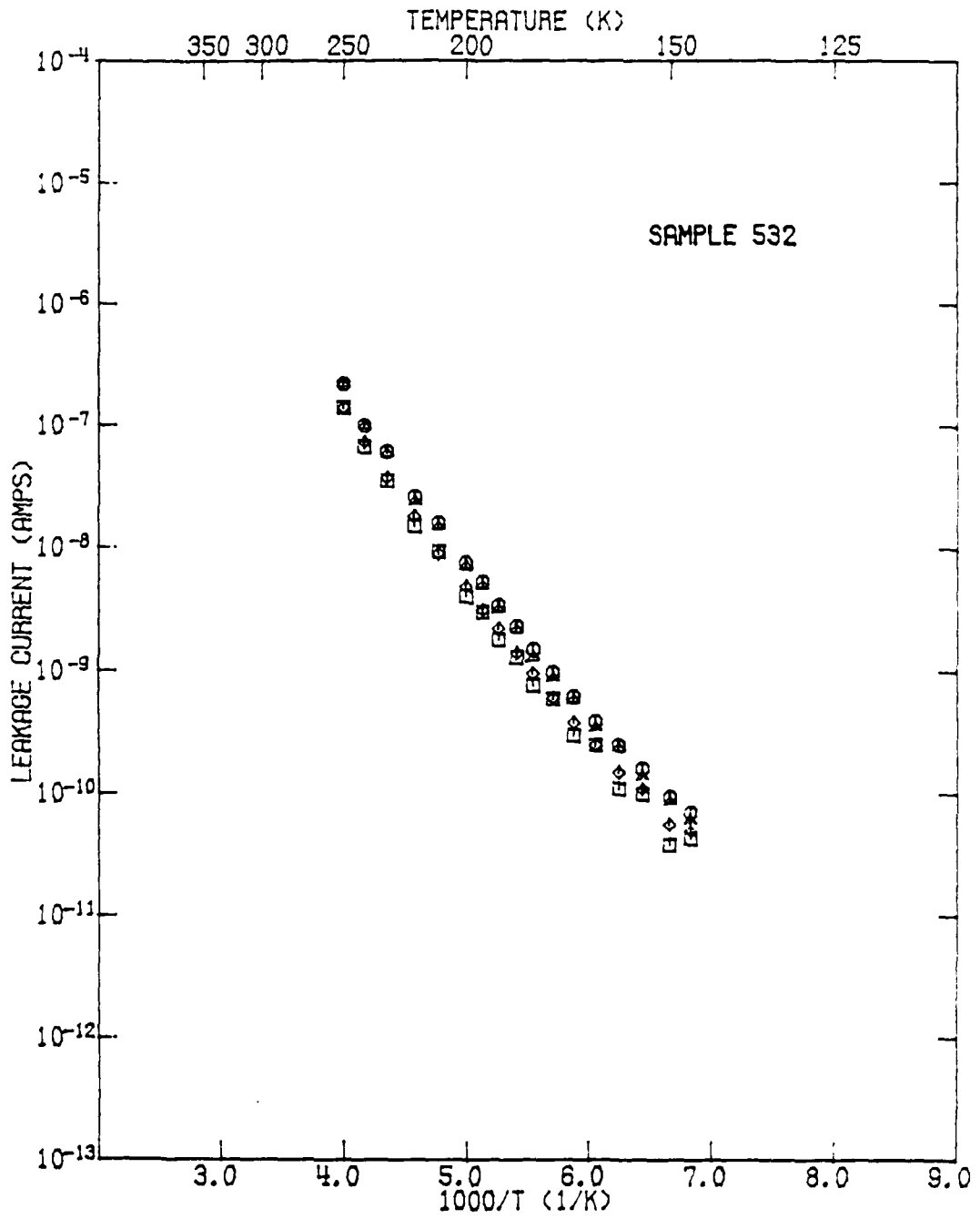


Figure 33. Leakage Current for a Leaky Sample

## c. Sheet Hole Concentration

The effective sheet carrier concentration was calculated for each of the electrical samples listed in Table 1, page 10, using Equation 14. The results are plotted for samples 471 and 532 in Figures 34 and 35 respectively. Configurations (e) and (f) of Figure 26 were used alternately for every other point. The sheet carrier concentration is shown for both forward and reverse current directions for each configuration. The forward and reverse current results match very closely except for higher temperatures in Figure 34 where the leakage current is very large. Note that the plot for  $\log(P_S)$  versus  $\frac{1}{T}$  for sample 532 is very linear even though Figures 31 and 33 indicate there is a considerable error due to the leakage current. This points out the importance of monitoring the leakage current for Hall-effect measurements on implanted layers.

While the effective sheet carrier concentration which is measured does not give the actual sheet carrier concentration, the relative concentrations between samples can be determined as indicated by Equation 16. If we assume that all the carriers in the tail region are frozen out (References 65 and 87) at low temperatures leaving a fairly uniform layer of carriers, then the effective sheet concentration should closely match the actual sheet concentration. The low temperature measurements (less than 200 K) were therefore used to give a qualitative measure of the actual sheet hole concentration. On a semilog plot, even errors of 25% will not greatly change the qualitative results.

Sheet carrier concentrations for samples implanted at 560 keV with a dose of  $10^{14}$  ions/cm<sup>2</sup> and annealed initially at 550°C are shown in Figure 36. The second 30 minute anneal was varied from 550°C to 940°C. Electrical activation occurs after the 550°C anneal. Figure 36 clearly shows that the electrical activation increases with increasing anneal temperatures through 940°C. The slope intercepts at 200 K from the plots of Figure 36 are shown in Figure 37. One sample, 473, annealed only at 800°C for 20 minutes did not show a significant different from samples 539 and 549 which were annealed with the two step technique at 550°C and 850°C.

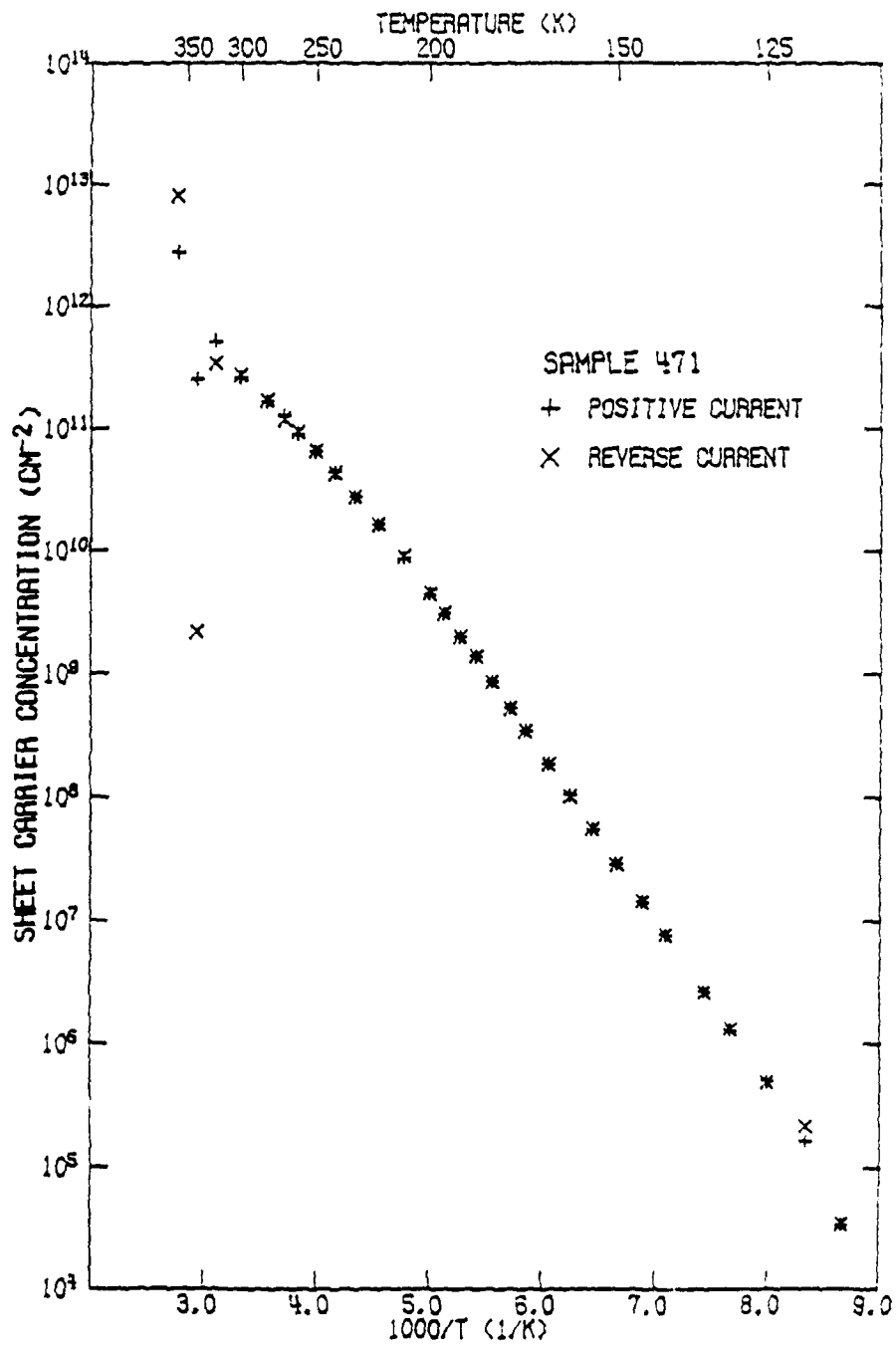


Figure 34. Sheet Carrier Concentration Versus Inverse Temperature for a Good Sample

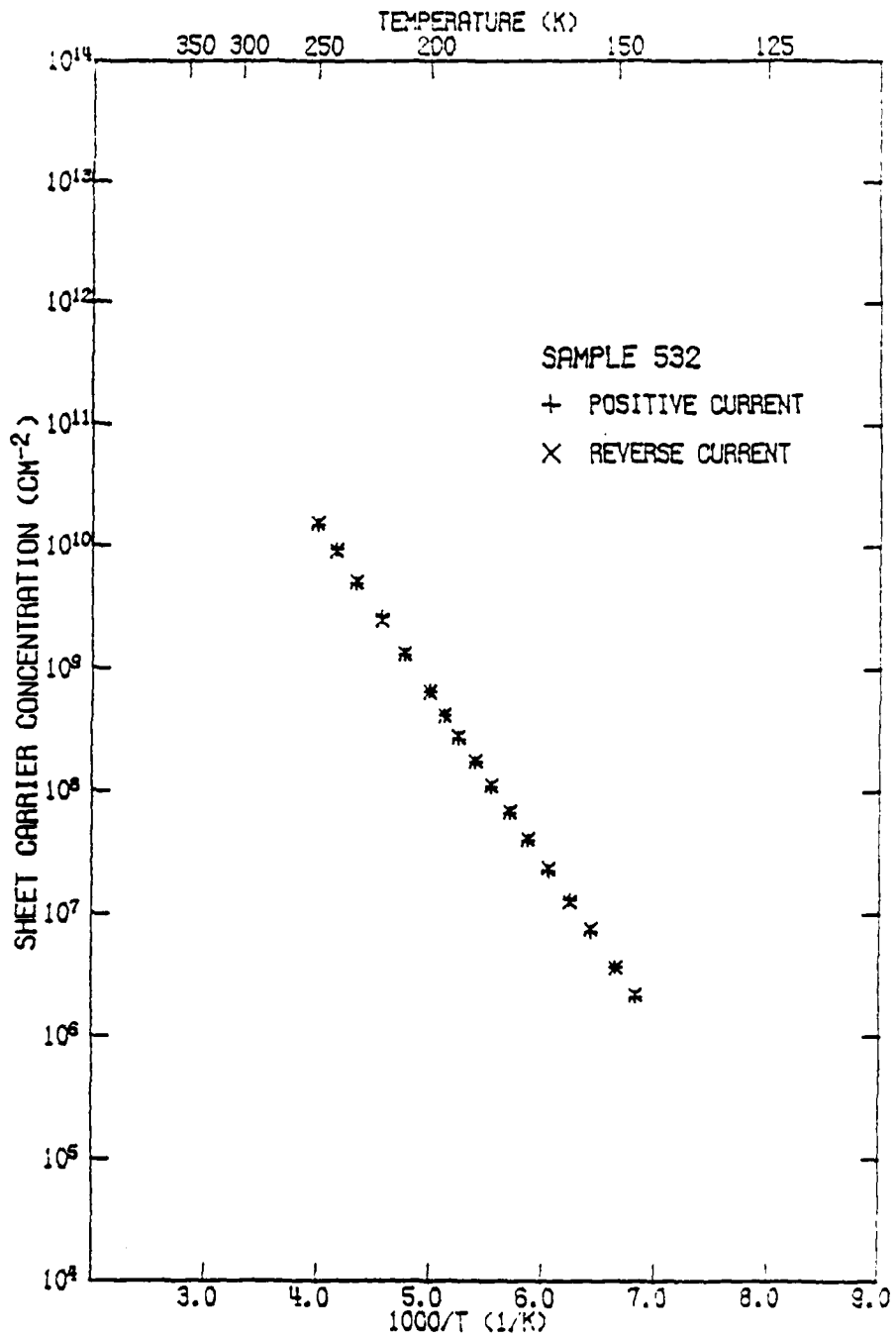


Figure 35. Sheet Carrier Concentration Versus Inverse Temperature for a Leaky Sample

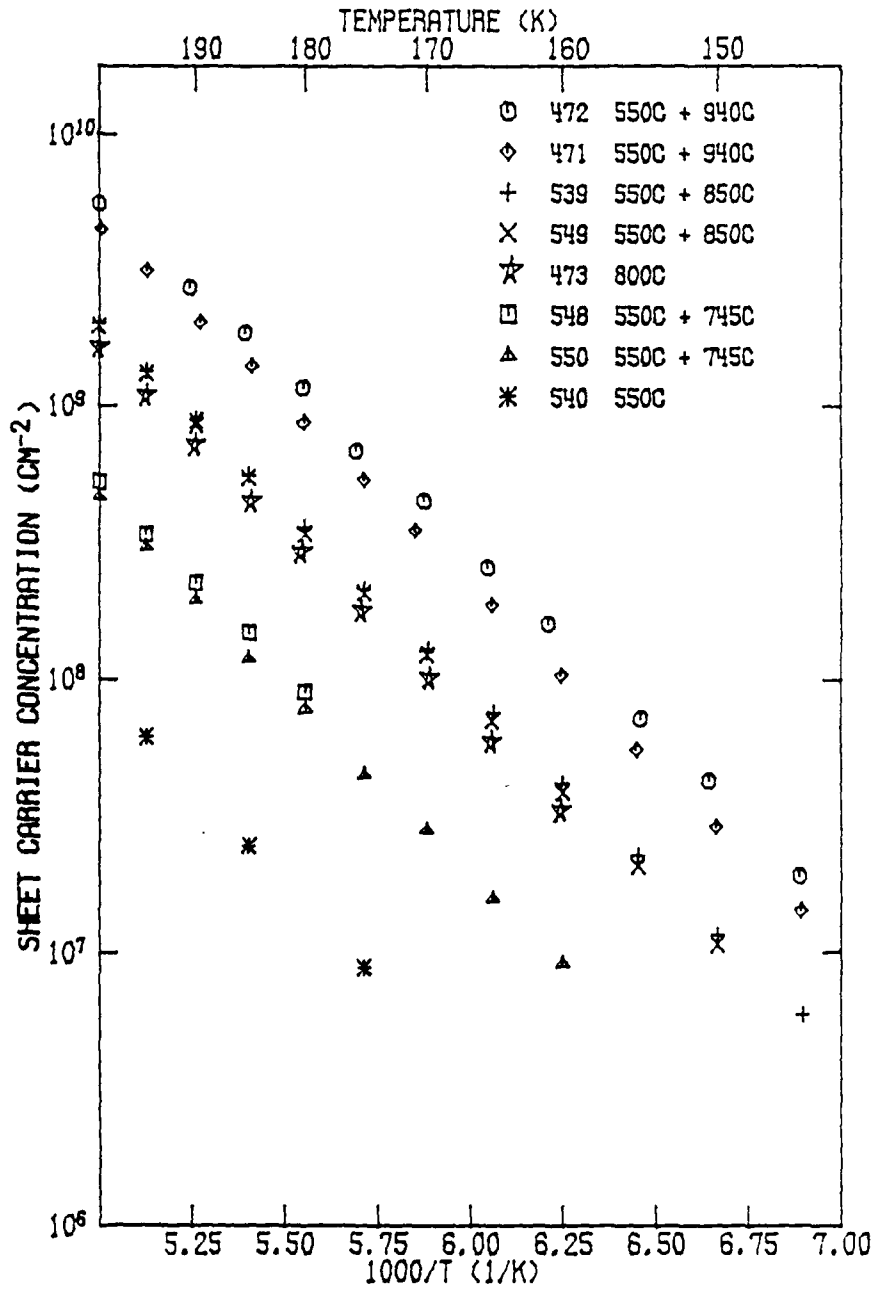


Figure 36. Sheet Carrier Concentration Variations with Second Anneal Temperature

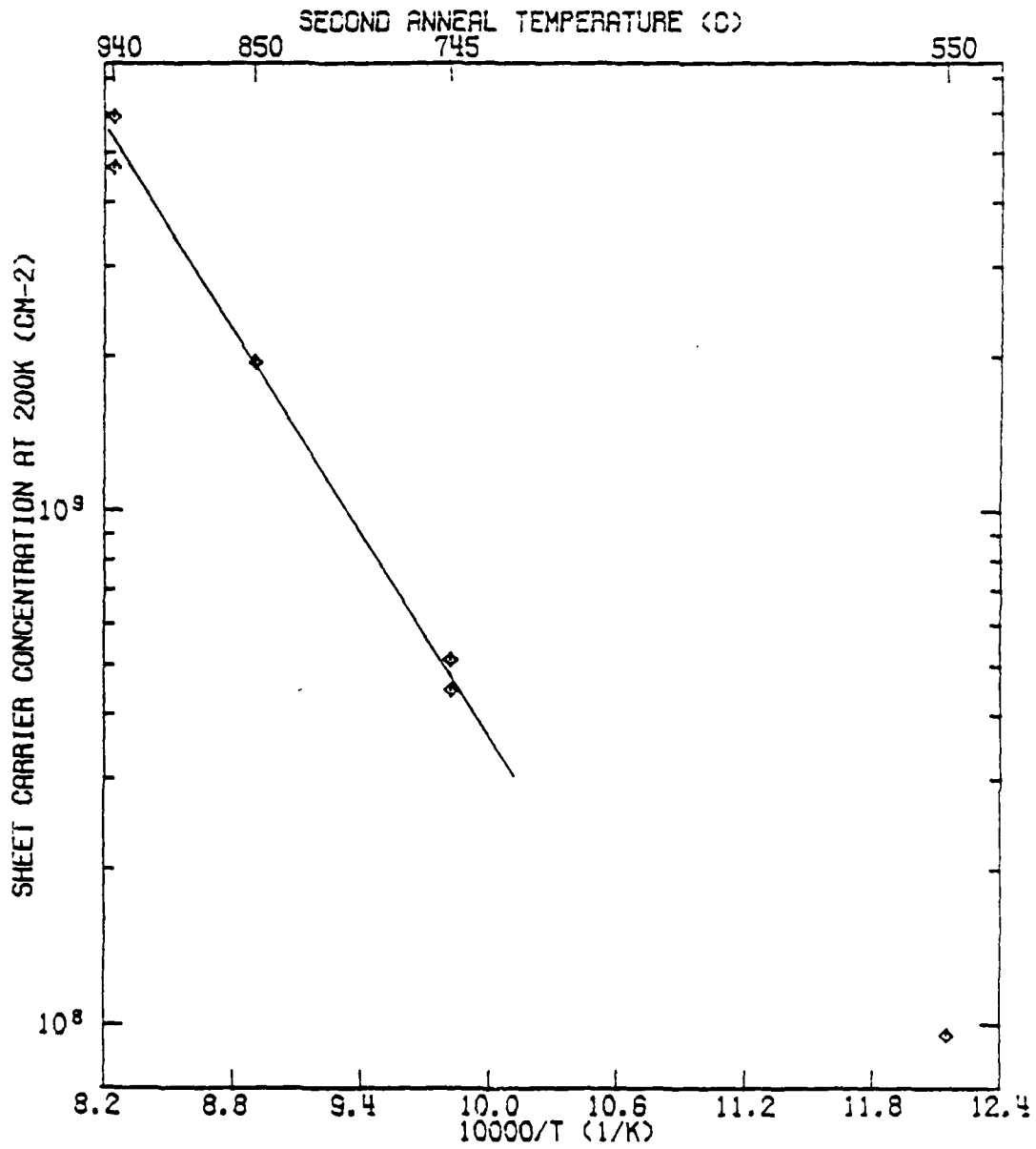


Figure 37. Sheet Carrier Concentration at 200 K as a Function of Inverse Second Anneal Temperature

The sheet carrier concentrations for varying implant doses are shown in Figure 38. All the samples were annealed with the two step technique at 550°C and 940°. Figure 38 shows the expected trend of increasing sheet hole concentration as the dose is increased from  $10^{13}$  to  $10^{14}$  ions/cm<sup>2</sup> at 280 keV and from  $10^{14}$  to  $10^{15}$  ions/cm<sup>2</sup> at 560 keV. An increase is also seen in increasing the implant energy from 280 keV to 560 keV for doses of  $10^{14}$  ions/cm<sup>2</sup>. This was also expected since the 560 keV implants have a much deeper distribution than the 280 keV implants; therefore, the dopant concentration will be smaller resulting in a higher probability of a Tl atom being substitutional considering the low solubility of Tl in Si.

One sample, 538, did not follow the trend of increasing sheet carrier concentration with increasing implant dose. It was implanted with  $10^{15}$  ions/cm<sup>2</sup> at 560 keV, but its carrier concentration plot fell just below those of 471 and 472 which was implanted with  $10^{14}$  ions/cm<sup>2</sup> at 560 keV. There is no apparent explanation for this decrease although 538 was a poor sample. Its  $R_a/R_b$  was erratic and it had a large leakage current, up to 7.5% of the measurement current in the temperature range of Figure 38.

#### d. Hall Mobility

The Hall mobility was calculated from Equation 10, and the conductivity mobility was determined from the Hall mobility using Equations 12 and 13. The results are plotted in Figures 39 and 40 for samples 450, 457, and 471. The temperature dependences ( $T^{-n}$ ) of both mobilities were calculated using a linear least-squares fit to the log-log plots. The results are given in Table 5.

#### e. Ionization Energy

Only three samples (450, 457, and 471) satisfied the criteria for quantitative results, namely temperature independent  $R_a/R_b$  ratios and a leakage current of less than one percent of the measurement current. The mean of the ratios of  $R_a/R_b$  and their standard deviation is given in

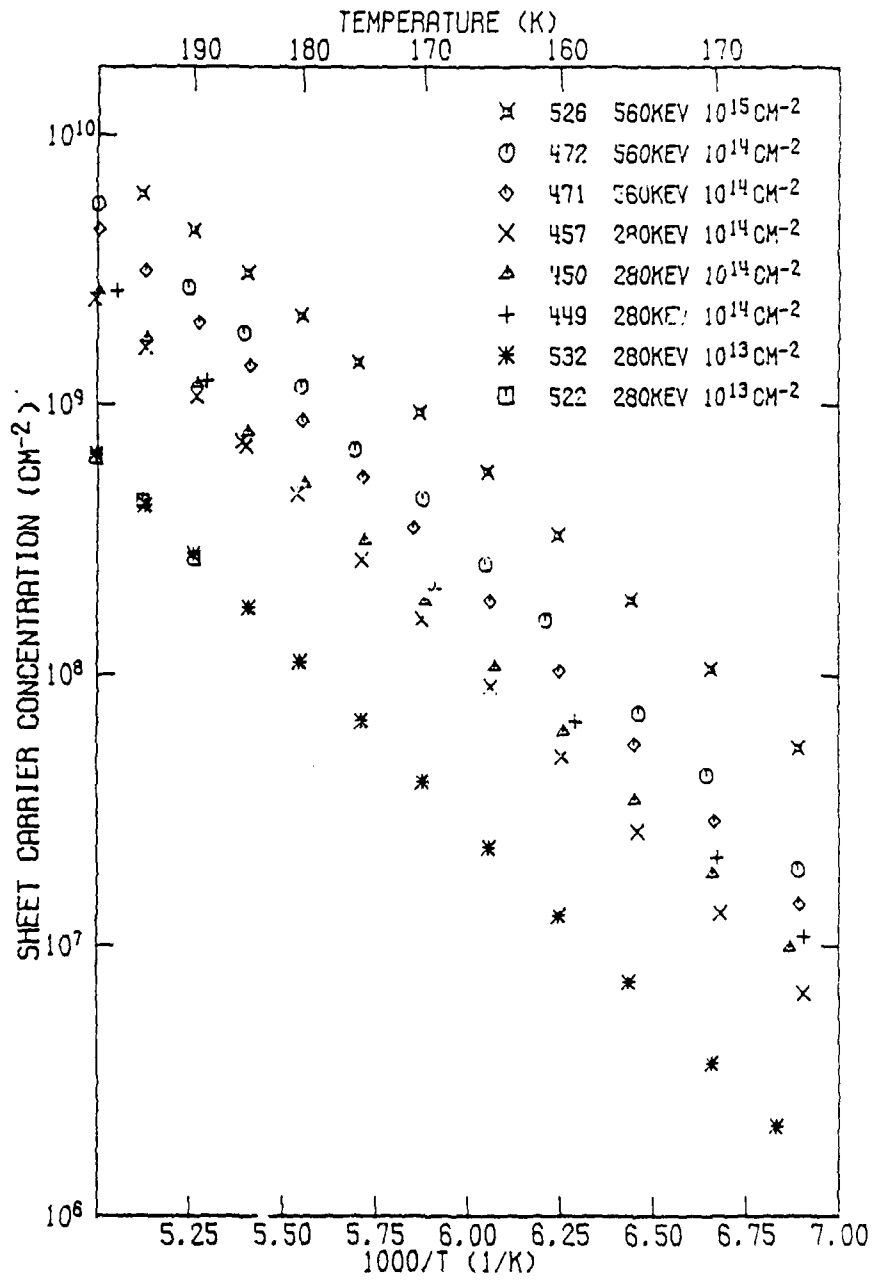


Figure 38. Sheet Carrier Concentration Variations with Dose and Implant Energy

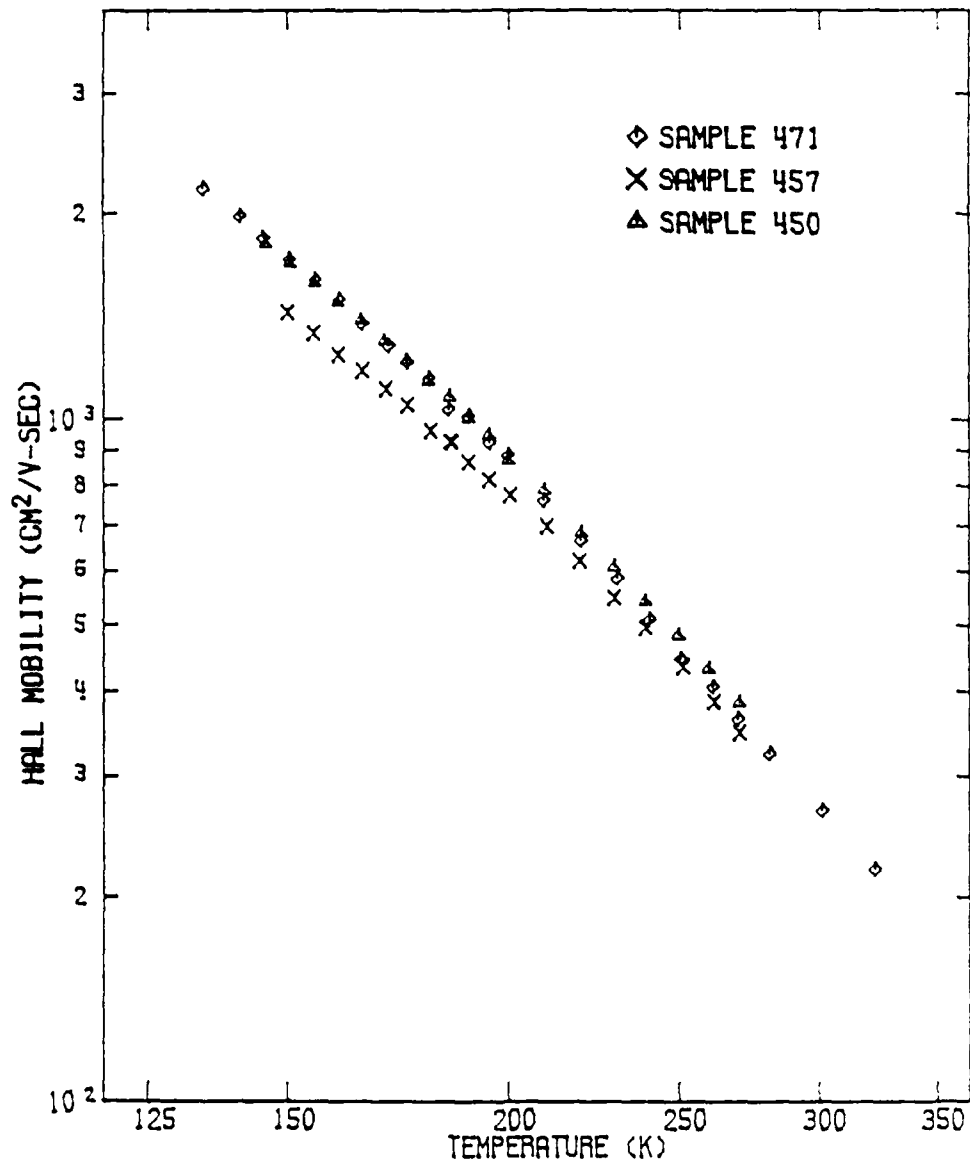


Figure 39. Hall Mobility Temperature Dependence

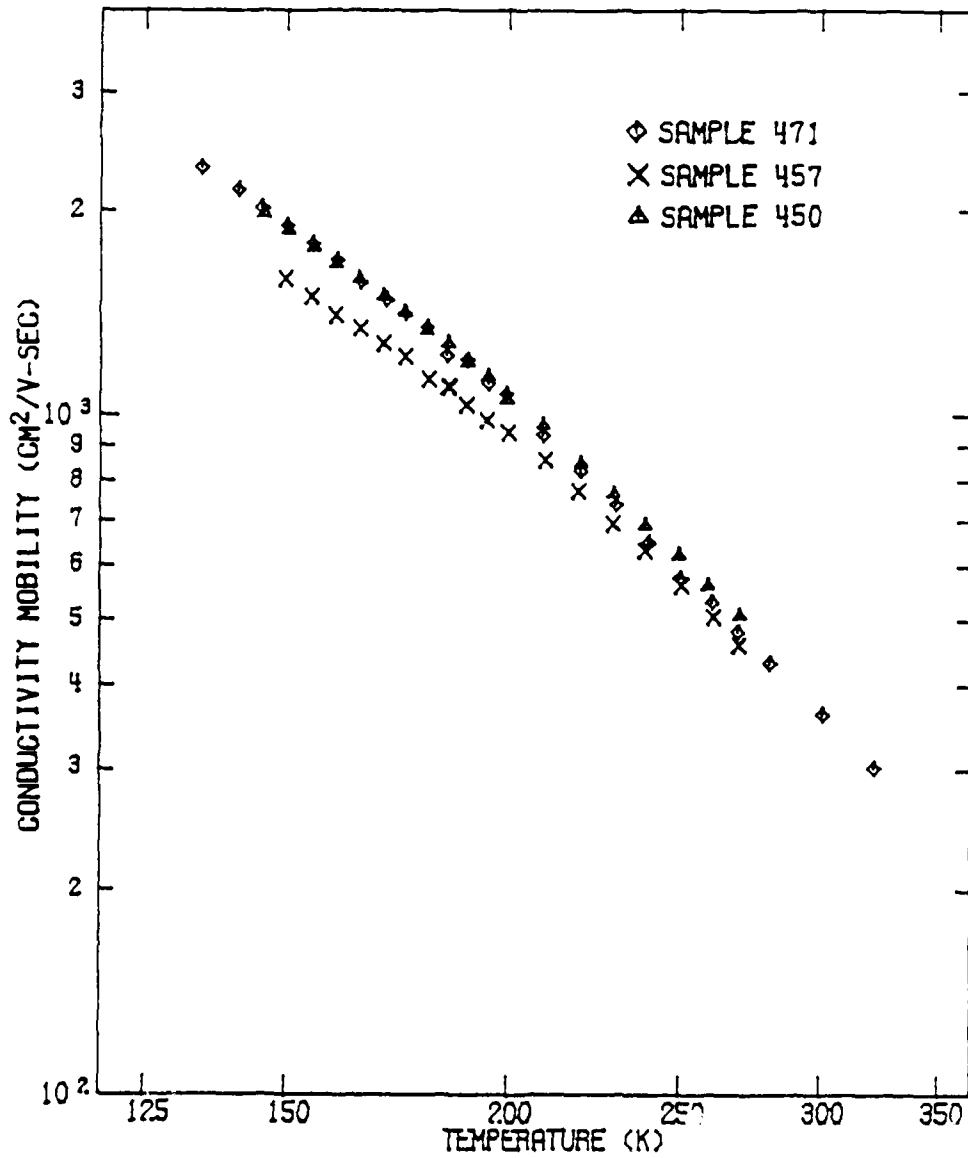


Figure 40. Conductivity Mobility Temperature Dependence

AD-A128 417

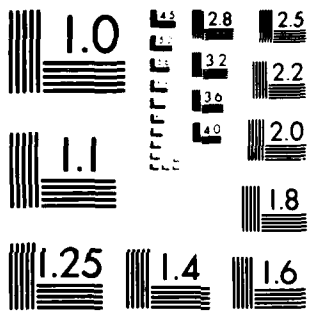
LUMINESCENCE AND ELECTRICAL CHARACTERIZATION OF ION  
IMPLANTED Si:TL(U) AIR FORCE INST OF TECH  
WRIGHT-PATTERSON AFB OH SCHOOL OF ENGI... O F SWENSON  
NOV 82 AFIT/DS/PH/82-1 AFWAL-TR-82-4115 F/G 20/12

22

UNCLASSIFIED

NL


END  
DATE  
FILMED  
6-83  
DTIC



MICROCOPY RESOLUTION TEST CHART  
NATIONAL BUREAU OF STANDARDS 1963 A

TABLE 5

 $R_a/R_b$  RATIOS AND MOBILITY TEMPERATURE DEPENDENCE

Sample	Temperature Range (K)	$R_a/R_b$	$f(R_a/R_b)$	Temperature dependence of $\mu_H$	Temperature dependence of $\mu_{cond}$
450	145.6 - 164.7	1.1260 $\pm 0.0241$	0.99878	$2.10 \pm 0.01$	$1.78 \pm 0.01$
457	149.7 - 165.0	1.2096 $\pm 0.0776$	0.99687	$2.04 \pm 0.08$	$1.72 \pm 0.08$
471	134.3 - 165.1	1.3242 $\pm 0.0384$	0.99322	$2.18 \pm 0.04$	$1.36 \pm 0.04$
471	209.3 - 322.1		0.99322	$2.90 \pm 0.04$	$2.59 \pm 0.02$

Table 5 as well as the geometrical correction factor  $f$  which was obtained by solving Equation 7 numerically for  $R_a/R_b$  as  $f$  was varied. The Hall scattering factor  $r_H$  was given by Equation 13. The activation energy  $E_a$  was calculated from the sheet conductivity using Equation 29 and the sheet carrier concentration Equation 27. Because these equations describe the compensated region, only data points for temperatures less than 165 K were used.

A linear least-squares fit was made of  $\ln(T^{-3/2} p_s)$  versus  $\frac{1}{T}$ , and the fit for sample 471 is shown in Figure 41. The results are given in Table 6 including the uncertainty (Reference 108) of the fit. The weighted mean (Reference 108) activation energy for the three samples was 0.229 eV. Fits were also done for the same points without the  $T^{-3/2}$  dependence of the effective density of states of the temperature dependence of  $r_H$  ( $r_H = 1$ ). The result was a weighted mean of 0.250 eV.

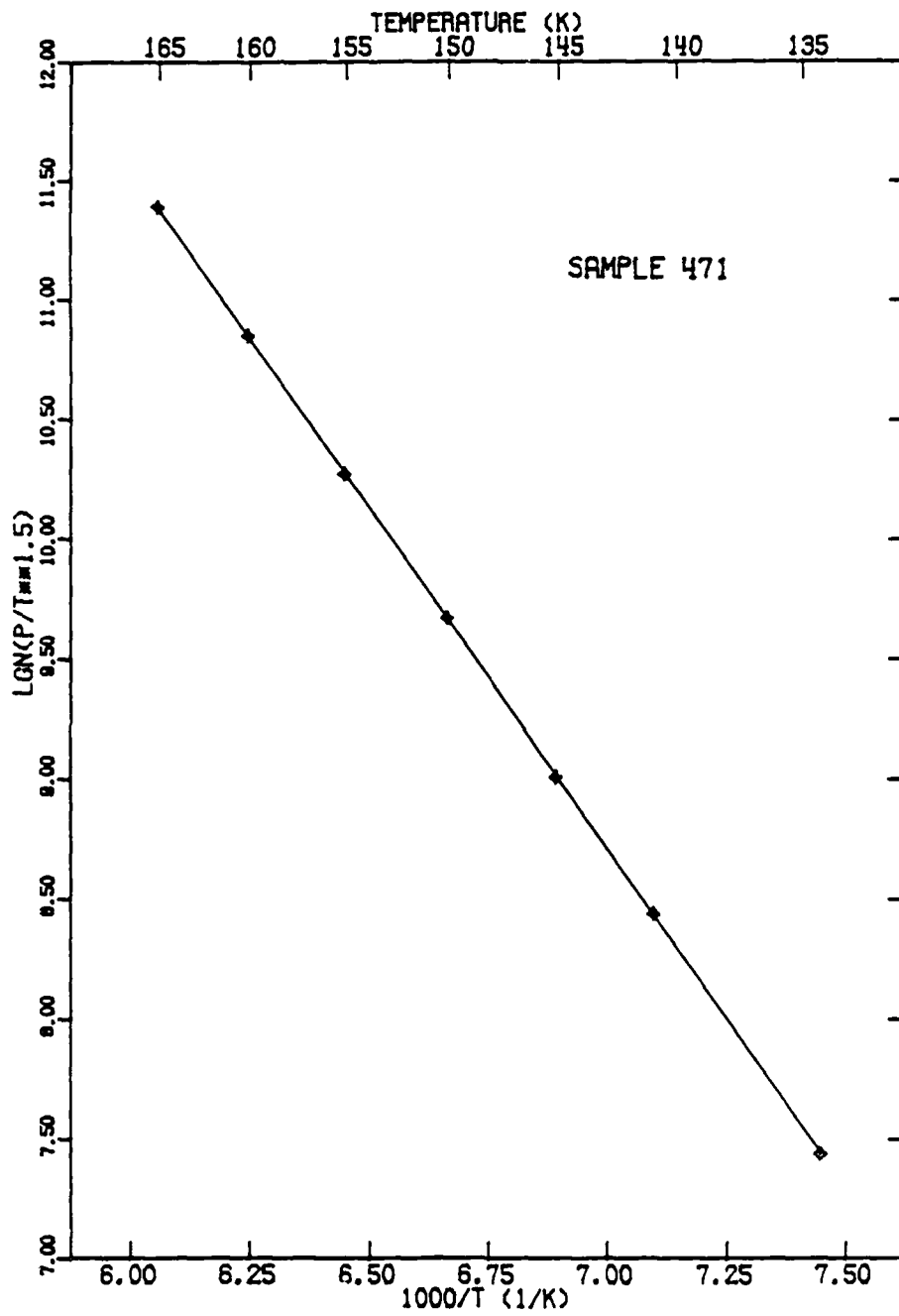


Figure 41. Fit of the Sheet Carrier Concentration in the Compensated Temperature Region

TABLE 6  
IONIZATION ENERGIES

Sample	Temp Range	$E_a$ (eV)		$E_a$ (eV)	
		$\ln \sigma_s$	$\ln T^{n-3/2} \sigma_s$	$\ln P_s$	$\ln T^{-3/2} P_s$
450	145.6- 164.7	0.222 $\pm 0.0002$	0.226 $\pm 0.0002$	0.249 $\pm 0.0003$	0.226 $\pm 0.0003$
457	149.7- 165.0	0.231 $\pm 0.0007$	0.234 $\pm 0.0007$	0.258 $\pm 0.0017$	0.234 $\pm 0.0018$
471	134.3- 165.1	0.228 $\pm 0.0004$	0.232 $\pm 0.0004$	0.254 $\pm 0.0005$	0.232 $\pm 0.0003$
Weighted Mean		0.224 $\pm 0.0002$	0.228 $\pm 0.0002$	0.250 $\pm 0.0003$	0.229 $\pm 0.0002$

Since the sheet conductivity and the sheet carrier concentration are calculated from different data on the same sample, the ionization energy calculated from the former was used as a check on the value determined above. The plots of sheet conductivity versus  $\frac{1}{T}$  are given in Figure 42. A linear least squares fit was made of  $\ln (T^{n-3/2} \sigma_s)$  versus  $\frac{1}{T}$ . The values of the conductivity mobility temperature dependence,  $n$ , used are given in Table 5. A fit was also done neglecting the  $T^{n-3/2}$  temperature dependence. The results are given in Table 6. The weighted mean of the  $\ln (T^{n-3/2} \sigma_s)$  fit matches the activation energy determined from the sheet carrier concentration. The Hall mobility of the implanted layer is related to the true mobility by Equation 18; therefore, the true temperature dependence of the mobility is not known. For this reason, the sheet carrier concentration should give a more accurate result for the activation energy. The agreement of the sheet conductivity result serves to confirm this value of 0.229 eV.

A fit was also done for the higher temperature region of sample 471. The ionization energy of 0.124 eV is slightly greater than half of the low temperature value of 0.232 eV, which is expected in the non-compensated region according to Equation 30. The low and high

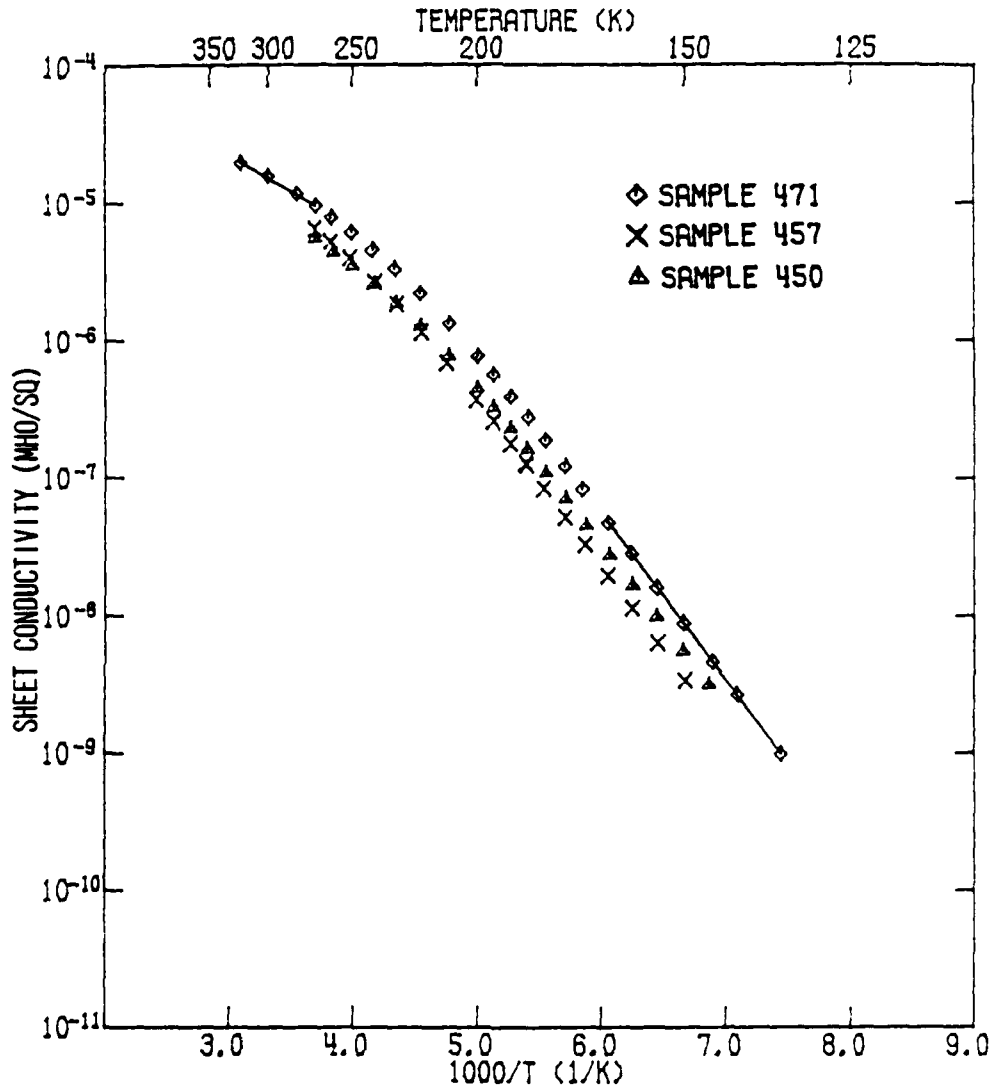


Figure 42. Sheet Conductivity Temperature Dependence

temperature fits for sample 471 are shown in Figure 42. The knee between these slopes clearly indicates that the points used to determine the activation energy from both the sheet carrier concentration and the sheet conductivity lie in the compensated region.

There was no difference in the activation energy between the two orientations (100) (sample 450) and (111) (samples 457 and 471) nor between implant energies of 280 keV (samples 450 and 457) and 560 keV (sample 471). A higher implant dose did show a change in activation energy  $E_a$  however. Sample 526 was implanted with  $10^{15}$  ions/cm<sup>2</sup> as opposed to  $10^{14}$  ions/cm<sup>2</sup> for samples 450, 457, and 471. It did satisfy the criterion of a leakage current less than one percent of the measurement current but had variations of  $R_a/R_b$  so that the quantitative result is in doubt. The fit for sample 526 gave a value of  $0.210 \pm 0.0008$  eV. This indicates that the sample is becoming degenerate with the higher implant dose.

#### 4. COMPARISON WITH PREVIOUS STUDIES

##### a. Ionization Energy of Ion-Implanted Silicon

The previously reported ionization energies measured in ion-implanted silicon are summarized in Table 7. Only very shallow dopants have been measured with the exception of indium and tellurium (Reference 75) which were measured with the differential Hall-effect technique. Seidel and MacRae (Reference 81) did not actually measure the ionization energy of B but compared the slope of their data with experimental results for bulk doped Si:B in the uncompensated region. They do not give results for the compensated region of ion-implanted Si:B. Zastavnyi et al. (Reference 86) found that for Na, complete impurity exhaustion occurs in the temperature range 250-77 K for any dose in samples annealed at temperature exceeding 550°C; therefore, the ionization energy must be measured at temperatures below 77 K. Because the other dopants listed in Table 7 are similarly shallow, their concentration as a function of temperature should be similar to that reported by Seidel and MacRae and by Zastavnyi et al. Therefore,

TABLE 7  
IONIZATION ENERGIES DETERMINED FOR IMPLANTS

Implant/Ref	Dose (cm <sup>-2</sup> )	Implant Energy (keV)	Assumed Implant Thickness (μm)	Anneal Temp °C	Temp Range °K	Measured Ionization Energy (eV)	Bulk Ionization Energy (eV)
P/26	6x10 <sup>13</sup>	50	0.25	500	90-330	0.055	0.044D
P/26	6x10 <sup>13</sup>	50	0.25	700	90-330	0.045	0.044D
P/27	1x10 <sup>15</sup>	400	--	550	35-250	0.027	0.044D
P/31	1x10 <sup>15</sup>	400	--	600-850	4.2-300	banding	0.044D
P/7	3x10 <sup>13</sup>	50	--	500-900	4.2-300	banding	0.044D
P/7	3x10 <sup>14</sup>	50	--	400-900	4.2-300	banding	0.044D
B/25	2x10 <sup>13</sup>	150	0.5	760	90-330	0.045	0.045A
B/26	6x10 <sup>13</sup>	50	0.5	500	90-300	0.084	0.045A
B/26	6x10 <sup>13</sup>	50	0.5	700	90-300	0.052	0.045A
B/27	1x10 <sup>15</sup>	400	--	480	40-200	dip	0.045A
Li/27	1x10 <sup>15</sup>	400	--	410	16-200	0.029	0.035D
Na/29	6x10 <sup>13</sup>	50	0.5	620-720	90-300	0.032	D
Na/30	6x10 <sup>15</sup>	30	100.	700	20-77	0.035-0.038	D
Na/30	6x10 <sup>14</sup>	50	100.	700	20-77	0.035-0.038	D
Na/30	6x10 <sup>15</sup>	30	270. Implanted both sides	800	20-77	0.035-0.038	D
K/29	6x10 <sup>13</sup>	50	0.25	620	90-300	0.073	D
K/29	6x10 <sup>13</sup>	50	0.25	670	90-300	0.1	D
K/29	6x10 <sup>13</sup>	50	0.25	720	90-300	0.04	D
In/16	5x10 <sup>12</sup> - 1x10 <sup>13</sup>	80	differential	350	110-285	0.160	0.16 A
In/16	5x10 <sup>14</sup>	50	differential	350	110-285	0.156	0.16 A
Te/16	4x10 <sup>12</sup>	220	differential	300-900	125-285	0.140	D

measurements to determine their ionization energy should also be made below 77 K.

The slopes reported (References 81, 82, and 85) for higher temperature ranges in Table 7 may actually be the up-slope of the dip reported for ion-implanted P (References 65 and 87). This dip has only been reported for degenerate implants but is probably present in lower doses as well. A dip is seen in the Si:B results of Gioson et al. (Reference 83). The sheet concentration versus  $\frac{1}{T}$  plots reported by MacDonald and Galster (Reference 87) and by Wagner and Burkhardt (Reference 65) are constant for temperatures below 50 K indicating the presence of metallic banding and making a determination of the ionization energy impossible.

Except for the results of Zastavnyi et al. (Reference 86), all of the results of Table 7 are for low temperature anneals. Luminescence shows that a large number of defects remain in the implant layer for these anneal temperatures. If electrically active, these defects will strongly affect the ionization energy results.

With one exception (Reference 83), all of the ionization energies in Table 7 were determined by assuming a uniform layer and an effective layer thickness in order to fit the density of carriers equation to the measured sheet concentration. This neglects the fact that the measured sheet concentration is given by Equation 16. Also, since the experimental concentration used in the fit is inversely proportional to the layer thickness, large errors in the ionization energy are introduced by not knowing the layer thickness precisely.

The validity of using the differential Hall-effect to measure the ionization energy of ion-implanted dopants has been demonstrated (Reference 75). However, this is a tedious procedure prone to errors in determining the thickness of the etched off layer.

The present technique allows the accurate determination of the ionization energy for implants without making differential Hall-effect measurements. However, it does require high resistivity measurements in the compensated temperature region. This study also points out the importance of monitoring the leakage current and  $R_a/R_b$  as a function of temperature. Hall-effect measurements on implant layers should not be used at room temperature unless the temperature dependence is known. This is borne out by the previous P implant results (References 65 and 87) and by this study.

b. Electrical Measurements on Si:Tl

This is the first reported determination of the Si:Tl ionization energy,  $E_a$ , from Hall-effect measurements. This determination was also confirmed by sheet conductivity measurements. The previous determinations of  $E_a$  from conductivity (Reference 6) and resistivity (References 1 and 7) measurements neglected the temperature dependence of  $N_v$  and of the mobility. The present value of 0.229 eV is comparable to the previous values of 0.26 eV (Reference 6) and 0.21 eV (Reference 1), but should be more accurate because of these considerations. This value is also comparable to the thermal-emission-rate measurement of 0.24 eV (Reference 80).

The first mobility measurements are also reported for Si:Tl. The Hall mobility temperature dependence in Table 5 is comparable to the  $T^{-2.4}$  dependence reported (Reference 75) for In implants in Si.

## SECTION V

## RBS AND SIMS

## 1. RUTHERFORD BACKSCATTERING AND CHANNELING

The theory and application of Rutherford Backscattering (RBS) and channeling effects have been well documented (References 8, 10, 109, and 110); therefore, only a brief review will be given here. In RBS, a beam of high energy (1-2 MeV) low mass (generally He) particles is used as a probe. The probe ions suffer elastic nuclear collisions with the target atoms and additionally suffer a continuous energy loss as they move through the lattice, both before and after the elastic collision. The backscattered ions are collected at a fixed angle and their number as a function of energy is measured using a solid state detector. The resulting energy spectrum contains information about the mass of the atoms in the target as well as their numbers and spatial location relative to the surface (Reference 109).

If the probe beam is aligned at an angle smaller than some critical angle ( $1^{\circ}$ ) relative to a major symmetric direction, i.e. channeled, the fraction of probe ions backscattered can be drastically reduced (see Figure 2). The probe ions suffer only a series of small angle deflections as they are steered through the relatively open regions between the atomic rows (Reference 10) (channels). By analyzing the attenuation of backscattered ions from the major crystallographic directions, the amount of disorder and the number of impurities not on lattice sites can be determined.

## a. Depth Sensitivity

A typical RBS spectrum for a semiconductor with an implanted impurity is shown in Figure 43. For elastic scattering, the energies before and after scattering are related by (Reference 10);

$$E = k^2 E_0 \quad (32)$$

where

$$k = \frac{M_1 \cos \phi + (M_2^2 - M_1^2 \sin^2 \phi)^{\frac{1}{2}}}{M_1 + M_2} \quad (33)$$

$\phi$  is the scattering angle in the laboratory system (see Figure 44),  $M_1$  is the probe ion mass, and  $M_2$  is the mass of the target particle. For  $\phi = 150^\circ$ ,  $k^2$  is equal to 0.59 for Si and, therefore, the energy of He ions backscattered from the surface will be  $E_s = 0.59 E_0$ . Solving Equation 33 for  $M_2$  gives:

$$M_2 = M_1 \left( \frac{1 + k^2 - 2k \cos \phi}{1 - k^2} \right) \quad (34)$$

The mass of the target atom  $M_2$  can therefore be determined from the front edge of the energy spectrum when  $M_1$  and  $E_0$  are known.

The energy of a probe ion backscattered at depth  $x$  is given by (Reference 10)

$$E(x) \approx k^2 \left[ E_0 - \frac{x}{\cos \theta_1} S(E_0) \right] - S(k^2 E_s) \frac{x}{\cos \theta_2} \quad (35)$$

where  $S(E)$  is the electronic stopping power and  $\theta_1$  and  $\theta_2$  are the angles made with respect to the surface normal. Solving Equation 35 for depth  $x$  gives:

$$x = \frac{k^2 E_0 - E}{\frac{k^2}{\cos \theta_1} S(E_0) + \frac{1}{\cos \theta_2} S(k^2 E_0)} \quad (36)$$

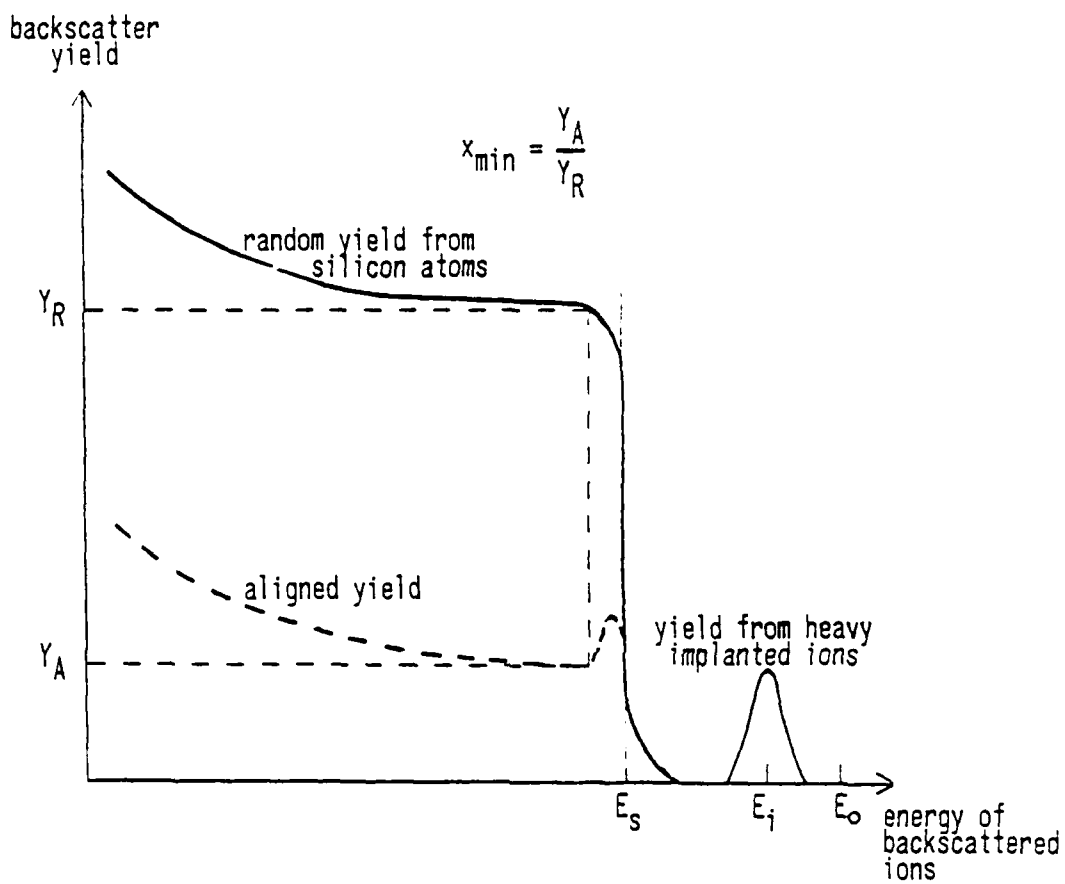


Figure 43. Typical Backscatter Yields in Silicon

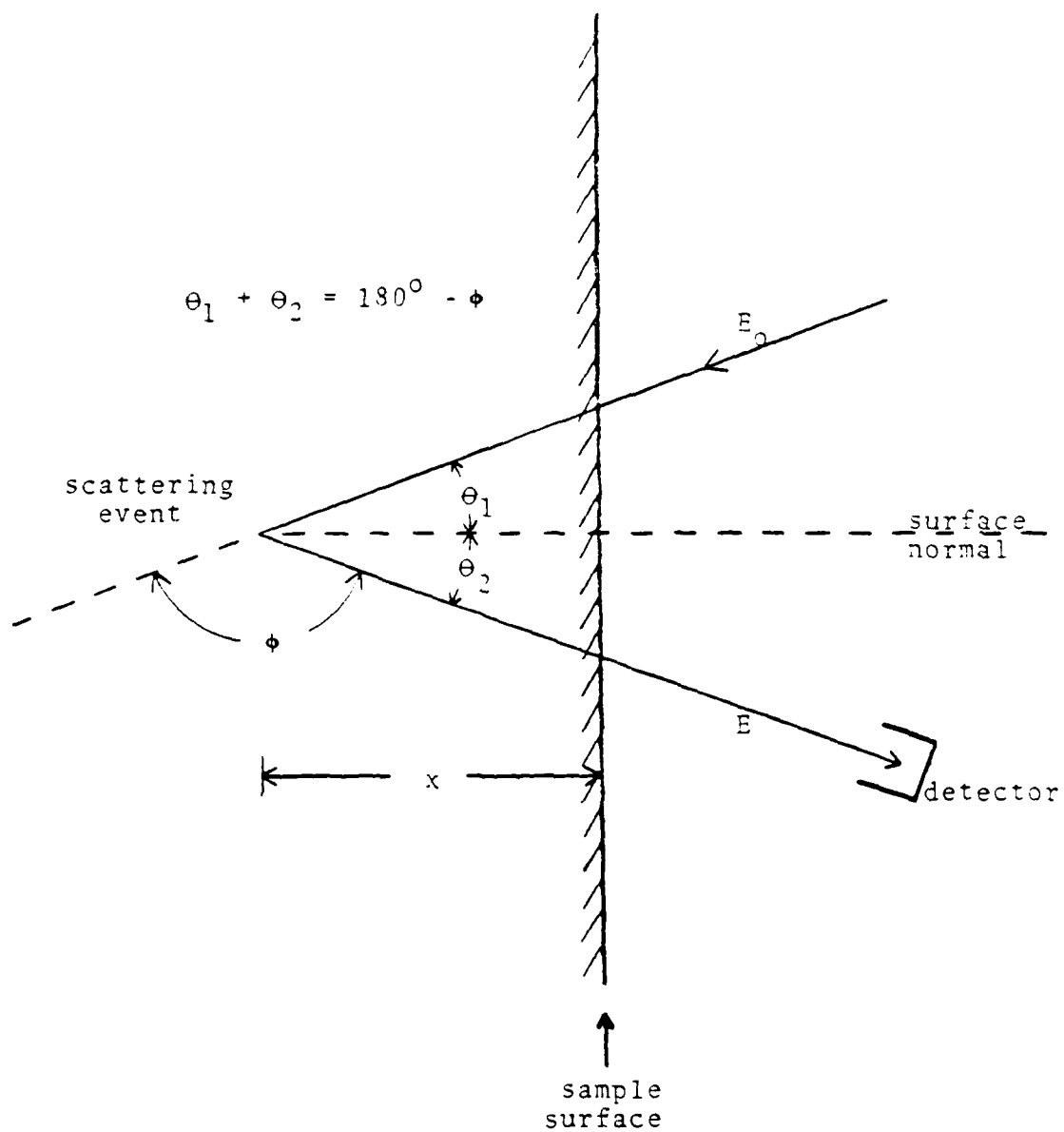


Figure 44. Typical RBS Configuration

From Equation 36 the energy spectrum can be converted to a depth spectrum. The depth resolution of the measurement will then be:

$$dx = \frac{dE}{\left[ \frac{k^2 S(E)}{\cos \theta_1} + \frac{S(k^2 E_s)}{\cos \theta_2} \right]} \quad (37)$$

By using a glancing angle geometry (e.g.  $\theta_1 = 80^\circ$ ,  $\theta_2 = 68^\circ$ , see Figure 45), the cosines will decrease resulting in a smaller  $dx$  and hence better resolution. For Ti target atoms and  $\theta_1 = 80^\circ$ , the resolution is approximately 25 Å/channel.

#### b. Lattice Disorder

The depth distribution of disorder can be determined from the energy spectrum of backscattered particles when the probe beam is channeled (Reference 8). If the probe beam is aligned in a random direction, the backscatter spectrum consists of a sharp edge at energy  $E_s$  corresponding to scattering from the atoms in the surface region, followed by a smooth, slowly increasing yield at lower energies corresponding to scattering from atoms at greater depths in the crystal as shown in Figure 43. This is true regardless of the disorder present in the crystal. When the probe beam is aligned with a major crystallographic direction, typically  $\langle 111 \rangle$ ,  $\langle 110 \rangle$ , or  $\langle 100 \rangle$ , the beam is split into channeled beam and random beam components (see Figures 2 and 46). The probe ions that strike the ends of the rows can interact with all the atoms within the crystal producing a scattering yield at all depths within the crystal, and thus form the random part. However, a considerable portion (95%) of the aligned beam is steered in such a fashion that it does not come closer to the lattice rows than 0.1-0.2 Å. These channeled ions will be deflected from the "forbidden" regions forming their channel resulting in an oscillating path leading deeper into the crystal with only a gradual randomization or dechanneling. Dechanneling increases as the probe ions slow down. Thermal oscillations of the lattice atoms also contribute to the randomization until eventually all the ions are dechanneled by approaching a lattice atom within the forbidden region. If there are no interstitial atoms and no

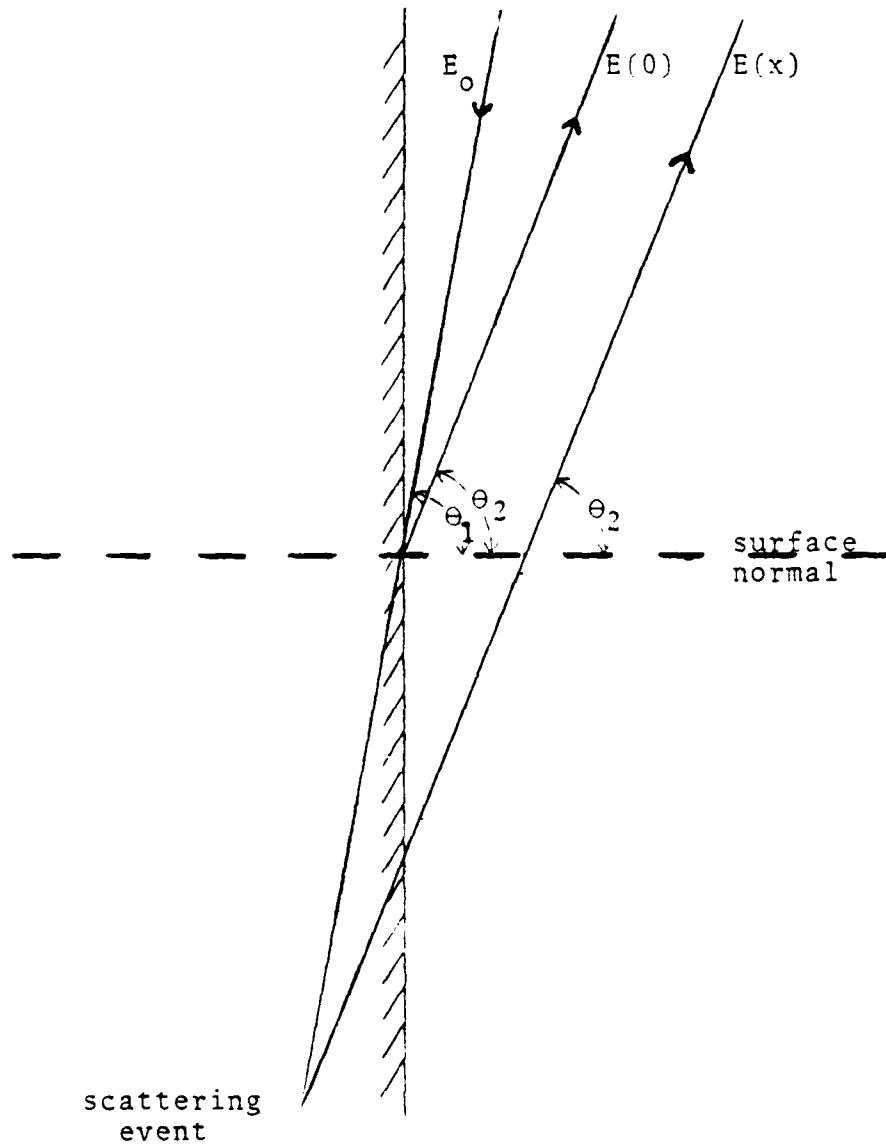


Figure 45. Glancing Angle, High Resolution RBS Configuration

disorder, channeling the probe beam will result in a 30-fold decrease (Reference 8) in the yield near the surface and a somewhat smaller decrease at greater depths. For a real crystal, there will be a small peak in the yield at the surface, due to the layer of atoms that form the surface as well as any residual damage or an oxide layer, followed by the slowly rising aligned spectrum (see Figure 43). The increase of the aligned yield at lower energies (greater depths) is a result of the escape of particles from channeling trajectories due to various scattering mechanisms.

For a damaged sample the surface peak for an aligned beam will be much larger and rise toward the random level (Reference 10). This "damage peak" corresponds to large angle scattering from the significant fraction of atoms located more than  $0.2 \text{ \AA}$  from lattice sites in the disordered region. The width of this peak will correspond to the depth of the disordered region (Reference 8). The background yield will also be increased over that of an undamaged crystal due to the additional "dechanneling" of the analyzed beam in passing through the disordered region.

At the position of minimum yield behind the surface peak, the quantity  $x_{\min}$  is defined by

$$x_{\min} = \frac{Y_C}{Y_R} \quad (38)$$

where  $Y_R$  and  $Y_C$  are the yields from a crystal in random and perfectly channeled positions, respectively. The lowest observed value of  $x_{\min}$  is 2% in Si due to backscattering of the surface (Reference 109).  $x_{\min}$  is typically in the 4-6% range. The quantity  $x_{\min}$  gives an indication of how much the probe beam has been randomized upon passing through the lattice damage near the surface and it therefore serves as a measure of the relative amount of disorder present in the implant layer.

## c. Impurity Atom Detection

Scattering from an impurity heavier than Si results in less energy loss than scattering from Si (Reference 10). The impurity peak will therefore be separated from the Si backscatter at a higher energy as shown in Figure 43. The impurity depth distribution can therefore be determined by Equation 36. If the implant distribution is Gaussian (Equation 1), the center of the backscatter peak will be the projected range  $R_p$ . For a Gaussian distribution, the standard deviation  $\Delta R_p$  is related to the full width at half minimum (FWHM) by

$$\Delta R_p = \frac{1}{2 \sqrt{2 \ln 2}} \text{FWHM} \quad (39)$$

If the probe beam flux is assumed uniform across a channel as Figure 2 indicates, then the lattice location of impurity atoms can be located by channeling along the  $\langle 100 \rangle$  or  $\langle 111 \rangle$  directions and the  $\langle 110 \rangle$  direction. From Figure 46, if an atom lies within a crystal row, it will not be "seen" when the probe beam is aligned along that crystal row. However, if it lies at a position within the channel more than  $0.2 \text{ \AA}$  from the crystal row, it will interact with the probe beam and cause backscattered ions. The peak area corresponding to impurity backscatter is therefore a measure of those atoms which occupy positions within the open channel and can be "seen" by the beam. The reduction in yield from the impurity between random and aligned exposures can therefore be used as a measure of the proportion of impurity that is located along the lattice row in question (Reference 10). From Figure 46 we see that tetrahedral interstitial positions are "hidden" from the beam along the  $\langle 100 \rangle$  and  $\langle 111 \rangle$  directions but not along the  $\langle 110 \rangle$  direction. Hence, by making measurements along either a  $\langle 111 \rangle$  or  $\langle 100 \rangle$  direction, a  $\langle 110 \rangle$  direction, and a random direction, it should be possible in principle to determine (Reference 8) the fraction of impurity atoms located:

- (1) Within  $0.1 - 0.2 \text{ \AA}$  of the substitutional lattice sites
- (2) Within  $0.1 - 0.2 \text{ \AA}$  of the tetrahedral interstitial sites
- (3) In some random locations other than (1) or (2).

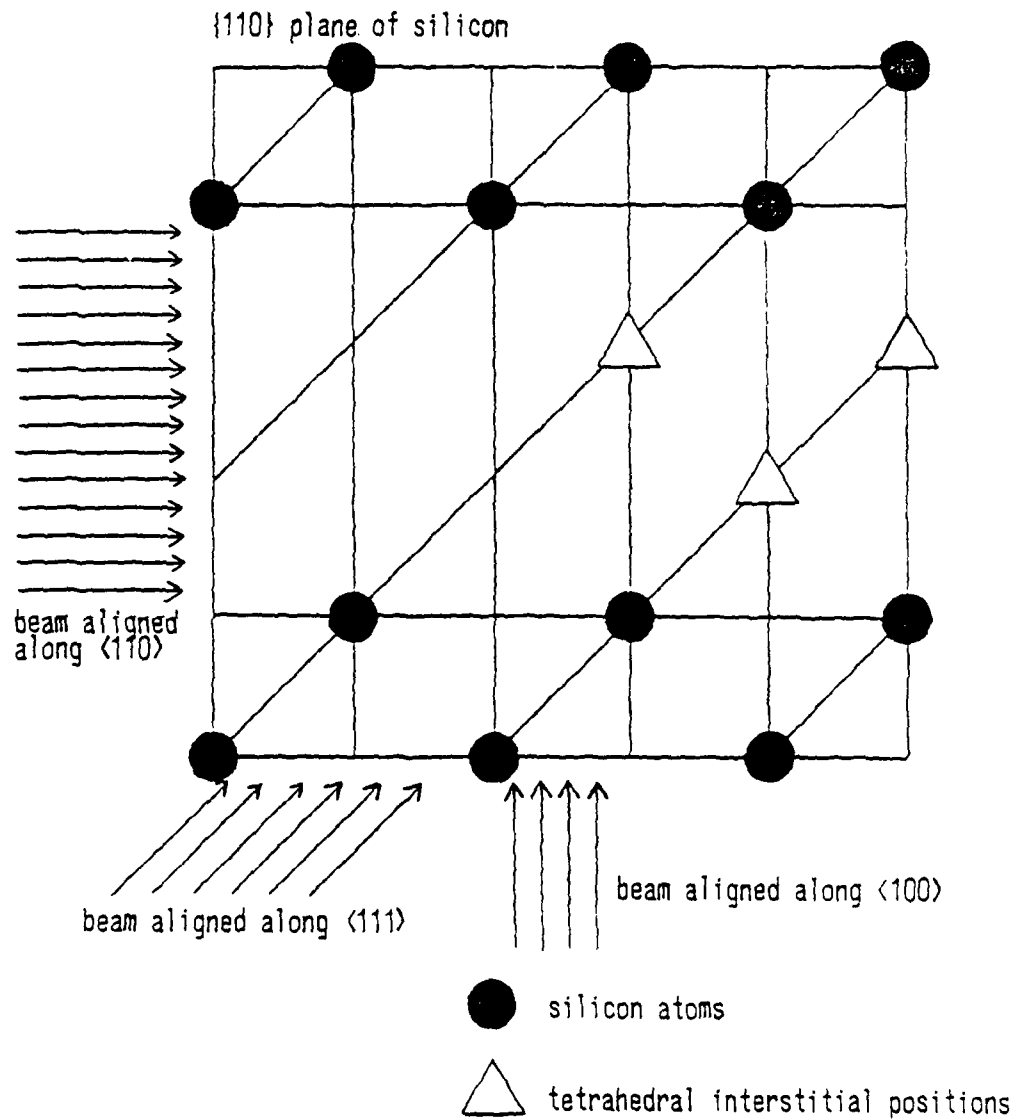


Figure 46. The  $\{110\}$  Plane of Silicon Showing the Locations Seen by a Channeled Probe Beam Along the Major Crystalline Directions  $\langle 110 \rangle$ ,  $\langle 111 \rangle$ , and  $\langle 100 \rangle$

Unfortunately, recent experiments have shown that the probe beam is not uniformly distributed between the rows (Reference 10) and this makes quantitative determination of the impurity atoms by this technique very difficult. The flux can be enhanced ("flux peaking") in the central region of the channel by as much as 100% above that in a random direction (References 10 and 11).

d. Previous RBS Studies of Si:Tl

Several RBS studies (References 79, 111-117) were conducted on Tl implanted Si during the 1968-1970 time frame. By channeling 1 MeV He ions along  $\langle 111 \rangle$  and  $\langle 110 \rangle$  directions, Tl was found to be 30% substitutional, 30% interstitial and 40% located in random positions (Reference 111) for hot implants ( $450^{\circ}\text{C}$ ). For room temperature implants of  $10^{13}$  ions/cm<sup>2</sup> or less (Reference 114) atoms were found to be 80% on substitutional sites, with the substitutional component decreasing with dose. For both hot and room temperature implants, the Tl atoms moved from substitutional to interstitial sites (Reference 112) for anneal temperatures from  $500$ - $600^{\circ}\text{C}$ . They then moved to some sort of nonregular precipitation center at temperatures above  $650^{\circ}\text{C}$ . Implanting Tl into Si which was previously implanted with group V atoms was found to increase the substitutional component of Tl. When Tl implanted Si was bombarded with a  $1.8$  MeV  $^{12}\text{C}$  beam, Tl moved from substitutional sites to interstitial sites (Reference 115). Fladda et al. (Reference 115) hypothesized that Si interstitial atoms created during bombardment diffuse to substitutional Tl atoms and displace them into interstitial sites.

Domeij et al. (Reference 116) published the last article in this 1968-1970 series. They measured the yield of scattered  $1.8$  MeV  $^{12}\text{C}$ -ions as a function of the angle of incidence. Around the  $\langle 111 \rangle$  direction, the normal channeling dip was observed. Around the  $\langle 110 \rangle$  direction, either a narrow peak or a narrow peak superimposed on the channeling dip were found. Their conclusion was that the peak was due to the interaction of the probe beam with Tl atoms located in the tetrahedral interstitial sites (see Figure 46). The probe beam would not see these atoms when

aligned along the  $\langle 111 \rangle$  direction. The  $\langle 110 \rangle$  aligned yield for interstitial Zr atoms in Si was over twice the Zr atom random yield. This can be explained by the flux peaking within the central region of the channel. As a result, the substitutional determinations found in the previous work needs to be corrected for this flux peaking effect. For example, assuming the yield from tetrahedral interstitials is twice the random yield, a Tl sample that previously had been assigned 0% substitutional and 45% interstitial would really have 22.5% and 22.5%, respectively (Reference 116).

All of these studies were done with implantation energies of 40 keV ( $R_p = 214 \text{ \AA}$ ) or less and on (111) silicon. Anneal times were typically for 10 minutes which would correspond to an epitaxial regrowth of only  $30 \text{ \AA}$  at  $550^\circ\text{C}$ . Consequently the high temperature anneals would result in a polycrystalline layer with extended defects (References 14 and 15) allowing all of the Tl to escape to the surface. With a typical depth resolution of  $300 \text{ \AA}$ , the depth location of the Tl could not be determined. Blood et al. (Reference 15) found that 80% of the In escaped to the surface for high temperature anneals of 100 keV implants in (111) Si. Tl has a lower solubility than In which would probably result in an even higher loss.

Hirvonen (Reference 11) also studied 200 keV Tl implants in Si with RBS and channeling. He measured the disorder generated by room temperature and hot implants. For low doses ( $< 10^{13} \text{ Tl/cm}^2$ ), the disorder increased linearly with dose and then saturated for doses greater than  $4 \times 10^{13} \text{ Tl/cm}^2$ . Isochronal (10 min) anneal treatments showed little annealing of an amorphous layer for temperatures below  $500^\circ\text{C}$ . A sharp reduction in disorder was seen between  $500^\circ\text{C}$  and  $600^\circ\text{C}$  followed by a further decrease at  $700^\circ\text{C}$ . Subsequent annealing above  $700^\circ\text{C}$  showed little decrease in the disorder. The lattice location of the Tl atoms was also determined for one  $10^{14} \text{ Tl/cm}^2$ , 200 keV room temperature implant. Thermal annealing produced the following components:  $650^\circ\text{C}$ , 42% substitutional/15% interstitial;  $700^\circ\text{C}$ , 0% substitutional/45% interstitial; and  $800^\circ\text{C}$ , 5% substitutional/36% interstitial. After 11 days at room temperature, the interstitial component had decreased to 12%

while the substitutional component remained constant. This implies a room temperature diffusion and precipitation of interstitial Tl. The sample orientation was not specified, but if it were  $\langle 111 \rangle$ , the layer would regrow as polycrystalline Si at these annealing temperatures with grain boundaries and extended defects for the Tl to precipitate at. Hirvonen notes that the interstitial component may be overestimated due to the flux peaking effect but does not make a correction for this. A larger substitutional component would then also be expected.

#### e. RBS Results

RBS data were taken and analyzed at the University of Salford, Salford, England. The experimental apparatus for the results reported here is given by Christodoulides (Reference 118). The samples were analyzed by RBS in both random and channeling modes with 2 MeV  $^4\text{He}^+$ . In addition to the typical RBS configuration (Figure 44), the glancing angle configuration (Figure 45) was also used which gives a depth resolution of approximately  $30 \text{ \AA}$  with  $\theta_1 = 80^\circ$  and  $\theta_2 = -68^\circ$ .

The unannealed energy spectrum for Si implanted at room temperature to a dose of  $1 \times 10^{14}$  Tl ions/cm<sup>2</sup> at 280 keV is shown in Figure 47 using high resolution. The energy spectrum has been converted to depth and the Tl spectrum is shown on the same depth scale as the silicon spectrum. The resulting amorphous layer extends well beyond the mean ion range  $R_p$ .  $R_p$  for 280 keV implants was approximately  $1000 \text{ \AA}$  with a standard deviation  $\Delta R_p$  of  $215 \text{ \AA}$ . From Equation 2, the peak concentration was then  $1.86 \times 10^{19}$  atoms/cm<sup>3</sup>. The depth of the amorphous layer was approximately  $1750 \text{ \AA}$ . The mean range,  $R_p$ , for the 560 keV room temperature implants was estimated to be approximately  $1800 \text{ \AA}$  while the amorphous layer extended to a depth of  $2800 \text{ \AA}$ . Similar results were obtained from both (100) and (111) substrates for the same implant energies.

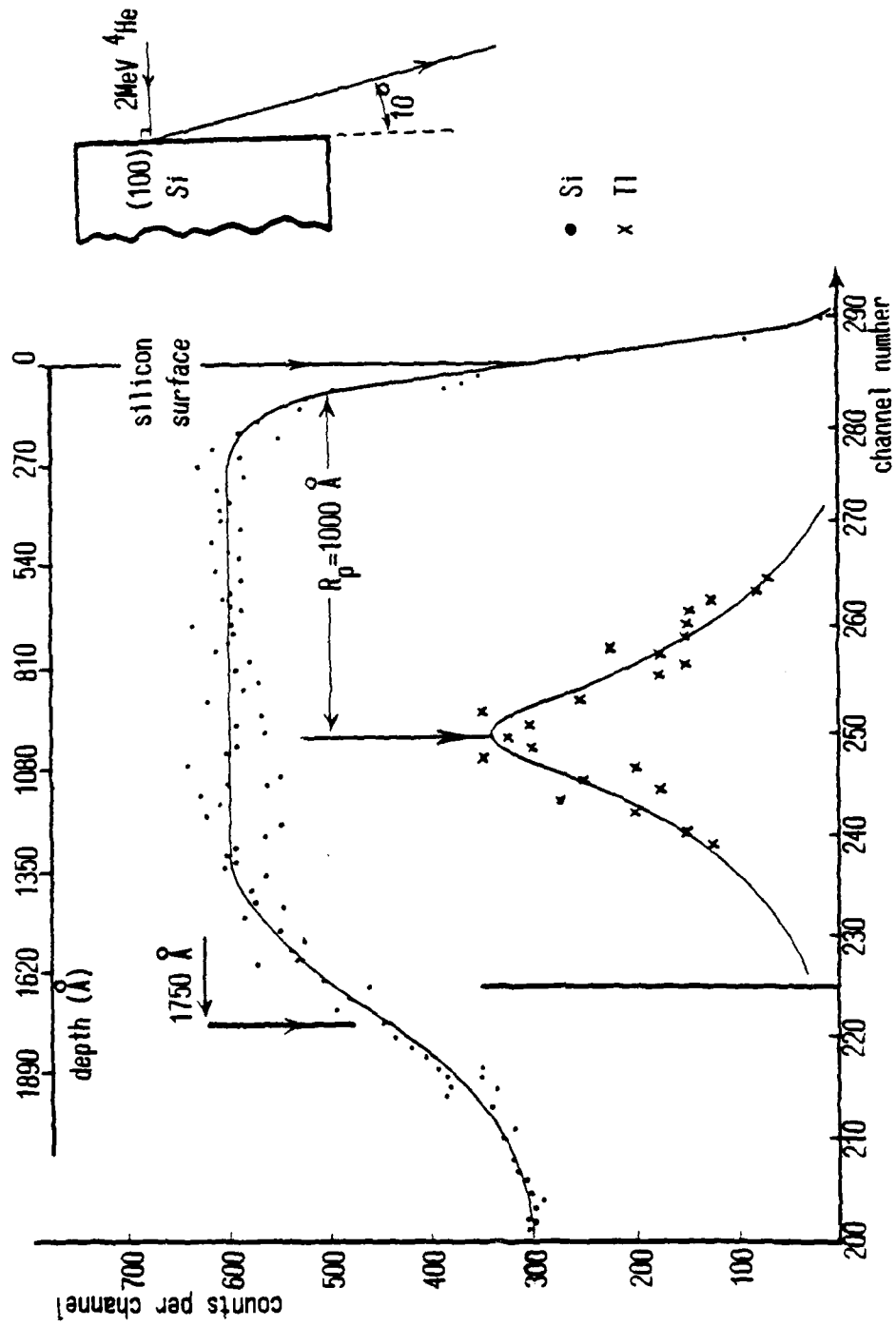


Figure 47. Low Angle Exit Aligned  $\langle 100 \rangle$  RBS Spectra from  $(100)$  Silicon Implanted with  $1 \times 10^{14} \text{ Tl/cm}^2$  at 280 keV, sample 293

The spectra for the probe beam aligned along the  $\langle 100 \rangle$  direction in (100) Si implanted at 280 keV is shown in Figure 48 using the typical RBS configuration. Plots are given for as implanted, annealed at 550°C, and annealed at 550°C plus a 940°C anneal. From this figure it can be seen that after annealing, a substantial reduction in the damage peak areas takes place. Data for the samples analyzed with RBS is presented in Table 8. The values of  $x_{\min}$  show that nearly all the disorder was removed for the (100), 280 keV sample after the 550°C anneal. However, for the (111) sample considerable disorder remains after the 550°C anneal. A possible explanation is that the sample was not completely regrown after the first anneal. Assuming a regrowth rate of 180 Å/hr for (111) Si, only 1080 Å of the 1750 Å amorphous layer would be regrown in 6 hrs. The disorder has been removed, however, after the high temperature anneal (Reference 15).

The Tl distribution has shifted toward the surface after the annealing; however, a large percentage of the Tl remains in the Si after the two-step anneal (550°C + 940°C), Figure 48. Additionally, the surface disorder is greater after the 940°C anneal than after the 550°C anneal. The backscattered spectrum for the same samples as in Figure 48 with the probe beam aligned along the  $\langle 100 \rangle$  direction but with the detector at an angle  $\theta_2 = 80^\circ$  is shown in Figure 49. The greatly improved resolution shows an oxygen peak located at the surface. This suggests that an oxide layer may have been grown on the surface during the high temperature anneal. This amorphous oxide layer could account for the larger surface disorder.

The attenuations (the percentage decrease in the area under the Tl peak in going from a random to an aligned direction) in Tl backscattered ions for a channeled probe beam are also given in Table 8. The attenuation percentage corresponds to the minimum percentage of Tl atoms located in the row of atoms with which the probe beam is aligned ( $\langle 111 \rangle$  or  $\langle 100 \rangle$ ). It is impossible to determine if the Tl atoms in the row are located at substitutional or interstitial sites from measurements along only the  $\langle 111 \rangle$  or  $\langle 100 \rangle$  directions.

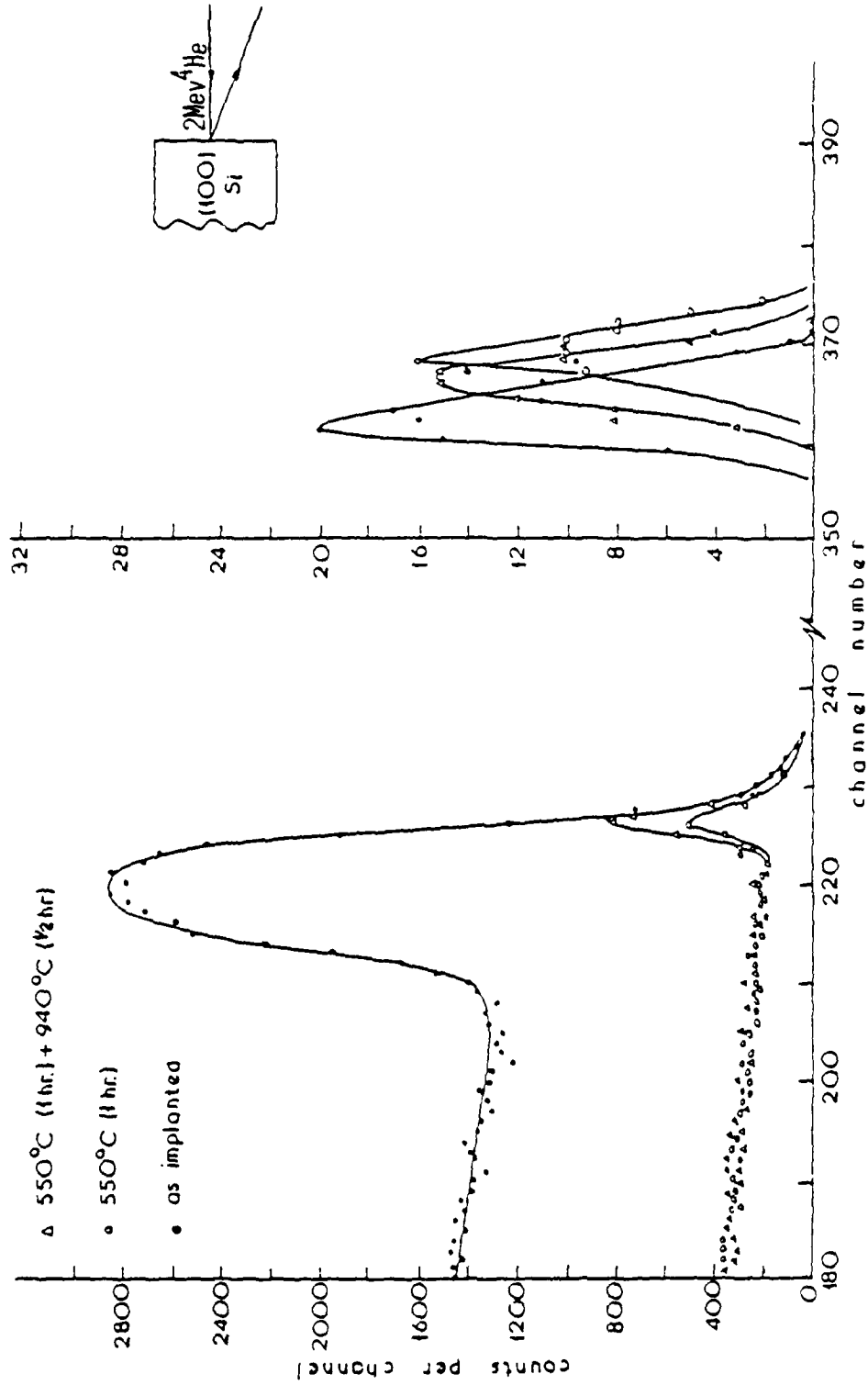


Figure 48. Aligned  $\langle 100 \rangle$  RBS Spectra from (100) Silicon Samples Implanted with  $1 \times 10^{14}$  Tl/cm<sup>2</sup> at 280 keV and then Annealed

TABLE 8

RBS RESULTS OF SAMPLES IMPLANTED WITH A DOSE OF  $10^{14}$  Tl/cm<sup>2</sup>

Sample	Energy (keV)	Substrate Orientation	Anneal (°C)	Si random height	Si max Aligned Yd	Si min Aligned Yd	X <sub>min</sub> (%)	Area under random Tl Signal	Area under Aligned Tl Signal	Attenuation
293	280	(100)	R.T.	2850	2850	1260	44	197	161	18
300	280	(111)	R.T.	2840	2800	820	29	183	156	15
307	560	(100)	R.T.	2820	2850	1600	57	216	172	20
345	560	(111)	R.T.	2800	2850	1440	51	181	162	10
393	280	(100)	550(1h)	2750	500	190	7	179	93	48
394	280	(100)	550(1h)+ 940(1/2h)	2750	810	190	7	135	99	27
397	280	(111)	550(6h)	2750	1050	570	21	155	118	24
398	280	(111)	550(6h)+ 940(1/2h)	2700	510	150	6	140	117	16

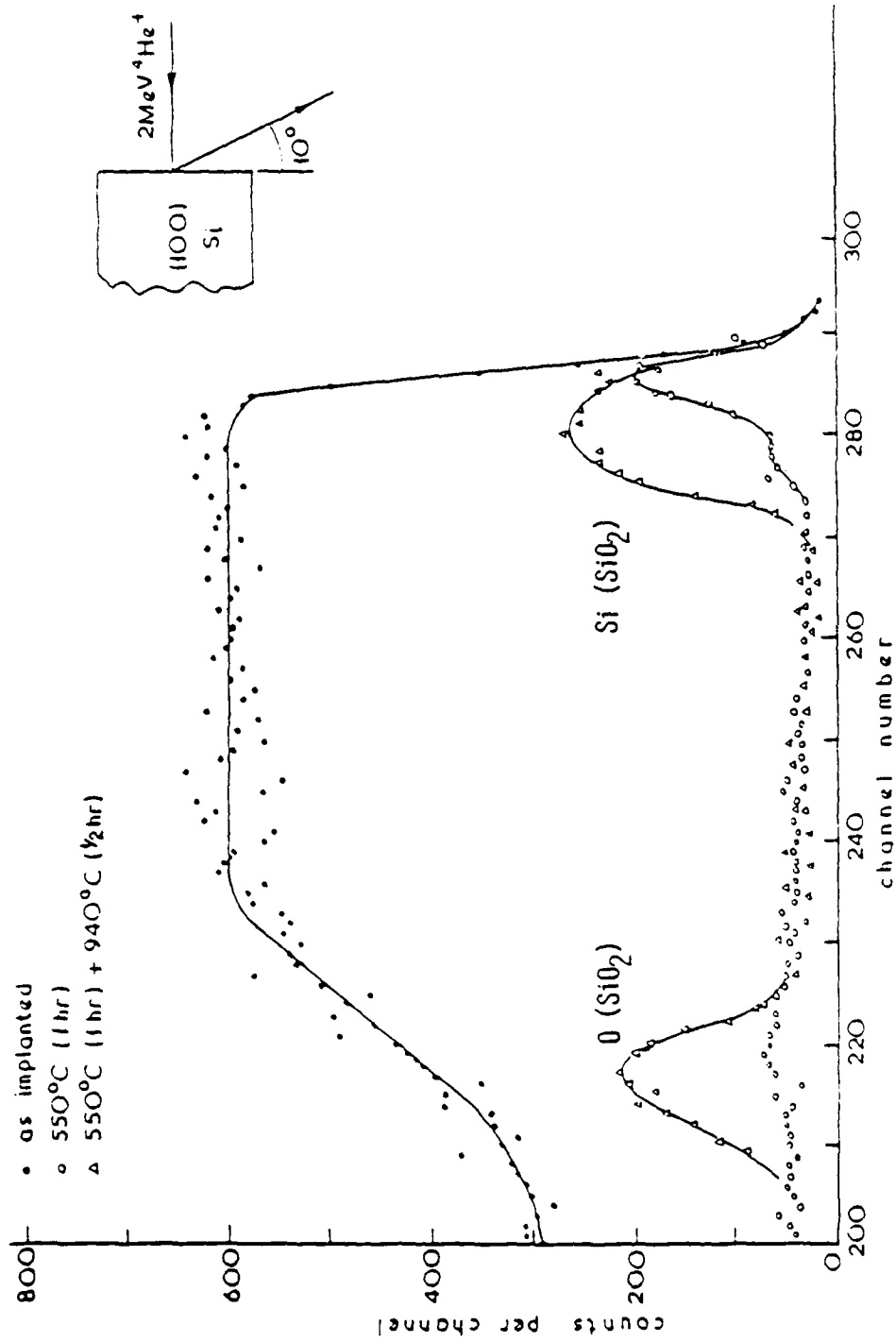


Figure 49. Low Angle Exit Aligned  $\langle 100 \rangle$  RBS Spectra from (100) Silicon Samples Implanted with  $1 \times 10^{14}$   $\text{Tl}/\text{cm}^2$  at 280 keV and then Annealed

The lower Tl attenuation percentages for the (111) samples, nearly one half, may again be accounted for by the amorphous layer not being completely regrown at 550°C. This might allow the aggregation of Tl atoms in extended defects created by the high temperature anneal of the remaining amorphous region. All (111) samples annealed after the RBS study were annealed at 550°C for over 14 hrs to insure the amorphous layer was epitaxially regrown.

## 2. SECONDARY ION MASS SPECTROMETRY

The secondary ion mass spectrometry (SIMS) technique employs a focused primary ion beam to bombard the sample and analyzes the small fraction of sample atoms that leave the surface as ions. A certain percentage of the sputtered particles (secondary ions) will be ionized. These secondary ions are then swept away by an electric field and passed through a mass analyzer. If the secondary ion signal of an element of interest is monitored as a function of time, a depth profile of the element will be produced (Reference 119). If the total depth is measured for a uniform sputtering rate, the sputtering time can be translated to depth.

SIMS profiles for different energy Tl implants in (111) Si were furnished by Dr. R. G. Wilson of Hughes Research Laboratories, Malibu, CA. The as implanted depth profiles are shown in Figure 50. The profiles are nearly Gaussian and the peaks for 300 keV and 600 keV closely match the projected ranges of 1000 Å for 280 keV and 1800 Å for 560 keV determined by RBS. The maximum Tl concentration for the 300 keV implant is  $5.5 \times 10^{18} \text{ Tl/cm}^3$ . This is in close agreement with the peak concentration of  $1.86 \times 10^{19} \text{ Tl/cm}^3$  estimated for 280 keV implants (subsection 1e) when allowance is made for the fact that its dose was 2.5 times the SIMS sample dose. Depth profiles after a 20 min 800°C anneal are given in Figure 51. The bulk of the Tl remains in the Si in agreement with the RBS results. Note that the tail of the Tl distribution extends out to 8000 Å for the 300 keV annealed sample and beyond 10,000 Å for the 600 keV annealed sample.

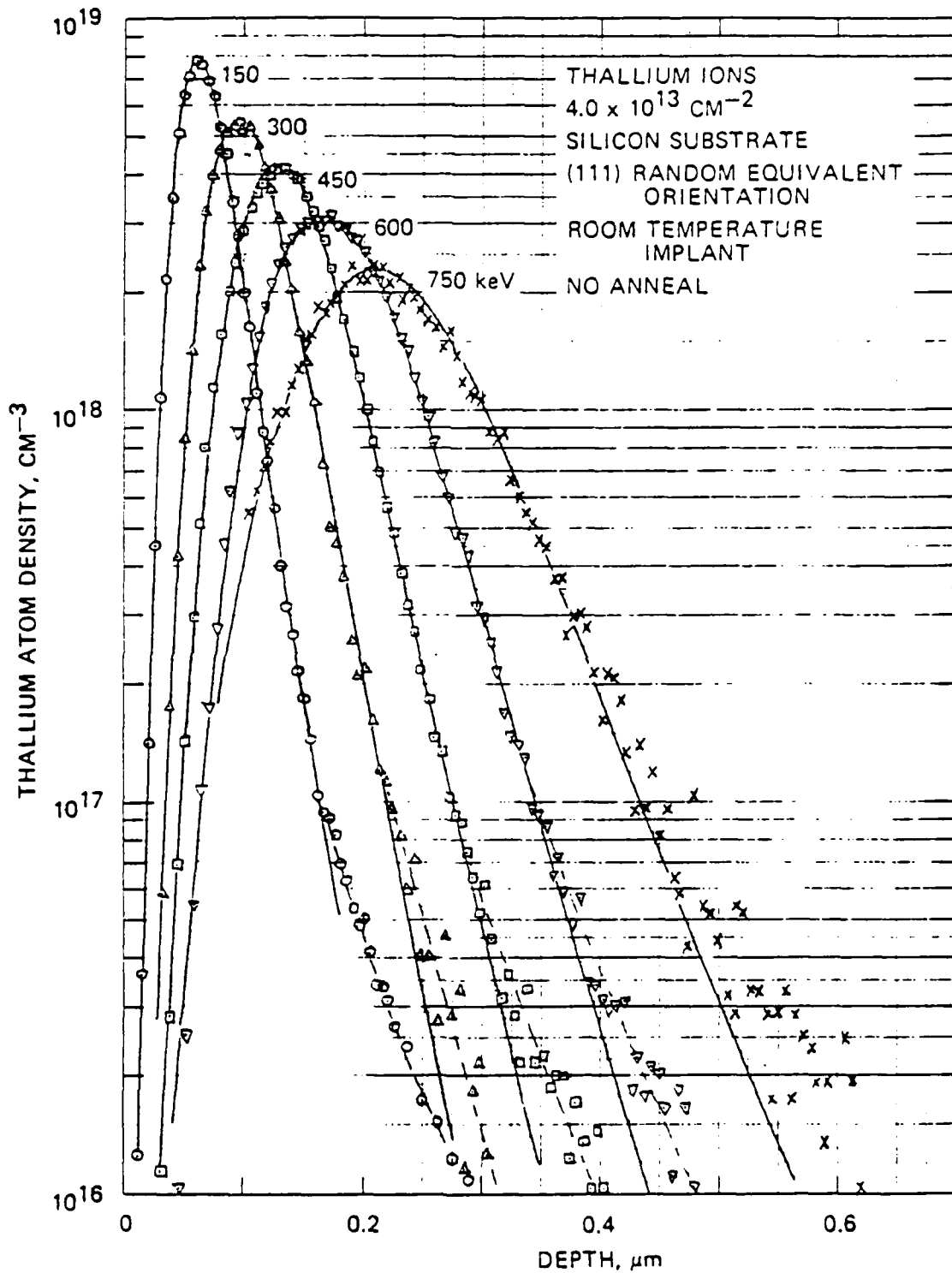


Figure 50. SIMS Depth Profile from Unannealed Silicon Implanted with  $4.0 \times 10^{13} \text{ Tl/cm}^2$

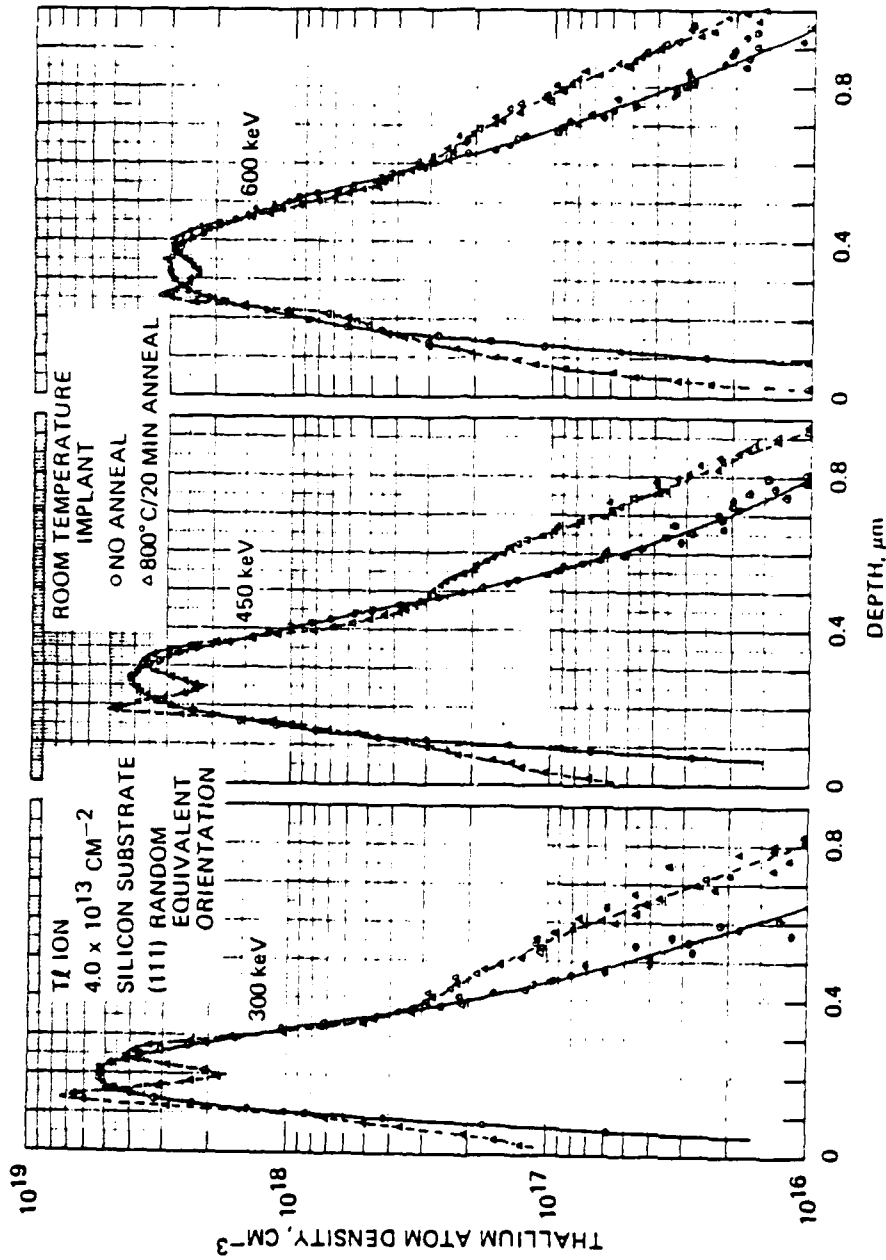


Figure 51. SIMS Depth Profile from (111) Silicon Implanted with 4.0 x 10<sup>13</sup> I<sup>+</sup>/cm<sup>2</sup> and then Annealed at 800°C for 20 Min

## SECTION VI

## CONCLUSIONS

The feasibility of using ion-implanted Si:Tl as a photoconductor material has been established. The implanted Tl has been shown to be both optically and electrically active. Further research is necessary to establish if high enough concentrations of active implanted Tl can be attained in Si to use it in an operational detector. The purpose of this research was not to fabricate an operational detector but to characterize the implanted layer. In addition to successfully characterizing implanted Si:Tl, this study established techniques for evaluating implanted layers in Si. The specific conclusions determined concerning Si:Tl are listed below followed by the techniques developed during this study.

1. Previous Si:Tl luminescence results were confirmed with better resolution in both bulk doped and implanted samples. The BE localization energy was determined to be 44.3 meV which is consistent with previous measurements of 43.8 meV (Reference 4) and 44.2 meV (Reference 33). The BE(TA) phonon replica was observed for the first time. The four excited states (Reference 33) of the BE(NP) were also resolved in the annealed implanted Si:Tl layer indicating a high quality regrown lattice structure.

2. A new unidentified transition U was observed 33.9 meV below the BE(NP) peak. Temperature and pump power characteristics indicate it has the same initial state as the BE transition. Its characteristics are analogous to those of the line located 4 meV below the BE(NP) in Si:In (References 28, 29 and 31) and it is probably caused by the same mechanism.

3. The electrical and optical activation both increased with increasing temperature of the second anneal of the two-step method. The optical activation was determined qualitatively by the BE(NP):FE(TO) ratio of the luminescence spectra taken at the same temperature for the

same depth implants. Electrical activities were compared qualitatively by sheet carrier concentration measurements. The T1 activation occurred after the epitaxial regrowth at 550°C and increased with the temperature of the second anneal through 940°C. These results do not agree with previous RBS results (Reference 112) that the substitutional component decreases with high temperature anneals; however, the previous studies were for low energy implants for which outdiffusion is expected.

4. RBS and SIMS results confirmed that a high concentration of T1 was retained in the Si after annealing. RBS results in the present study do indicate a decrease in T1 along the  $\langle 111 \rangle$  and  $\langle 100 \rangle$  rows which may indicate that the interstitial component is decreasing by diffusion. This is supported by a decrease in the interstitial component at room temperature reported by Hirvonen (Reference 11). At least 27% of the T1 atoms lie along the  $\langle 100 \rangle$  row for (100) Si after the 940°C anneal; however, the substitutional component could not be determined.

5. The sheet carrier concentration increased with dose at the same implant energy and also with implant energy at the same dose as expected. No differences were seen between (111) and (100) Si substrates. Unfortunately, absolute values for the acceptor concentration could not be determined due to the concentration variation with depth.

6. No significant difference was seen in the sheet carrier concentration between a single temperature anneal of 800°C and two-step anneals of 550°C and 850°C. However, luminescence of single-step annealed samples indicated localized spots with high T1 concentrations and large regions with primarily intrinsic Si luminescence. This can be interpreted as due to the formation of polycrystalline Si with some of the crystals containing high concentrations of T1. This result points out the necessity of using the two-step anneal with long enough 550°C anneals to completely regrow the implant layer epitaxially.

7. The Hall mobility for implanted Si:Tl varies as  $T^{-2.4}$  in the temperature range 135-165 K. The conductivity mobility in the same temperature range varies as  $T^{-1.86}$  corresponding to scattering due to lattice vibrations. This was the first mobility measurement for Si:Tl.

8. The ionization energy was determined to be 229 meV by the first Hall-effect measurements of implanted Si:Tl. This value was confirmed by sheet conductivity measurements. It is comparable to previous electrical measurements of 0.26 eV, 0.21 eV, 0.23 eV, and 0.24 eV; however, it is somewhat smaller than the optical ionization values determined by absorption, 246 meV (Reference 5) and 255 meV (Reference 3).

9. Luminescence is a powerful tool for detecting optically active defects in Si. This was the first luminescence study of defects caused by heavy ion implants in Si. The same sharp line defects were identified as in other studies (References 13, 36, and 38) with light ions. This confirms that the defects are dopant independent. In addition, better resolution was achieved which showed that several of the previously reported lines are split casting doubt on their earlier identification. The following peaks were identified in room temperature anneal implants: 1.034, 1.018, 1.000, 0.996, 0.981, 0.970, 0.967, 0.963, 0.955, 0.951, 0.948, and 0.898 eV. The peaks at 0.970 and 0.898 eV were also introduced by laser irradiation and had previously been reported (Reference 51) for gamma ray and fast neutron irradiation.

10. The defects introduced by ion-implanting can be completely removed by a two-step ( $550^{\circ}\text{C} + 940^{\circ}\text{C}$ ) thermal annealing procedure. The original defect luminescence is replaced by an intense broad peak after the implant layer has been regrown epitaxially at  $550^{\circ}\text{C}$ . This structure is nearly gone after a  $750^{\circ}\text{C}$  anneal and the defect structure is completely annealed out after a high temperature anneal at  $940^{\circ}\text{C}$ .

11. Optical activation of the Tl was observed for all samples after epitaxial regrowth at  $550^{\circ}\text{C}$ . Luminescence of an implanted dopant

in Si has not been previously reported with the exception of Nakashima et al. (Reference 42) who reported P luminescence only as a shoulder of the B BE(NP) peak. Luminescence associated with the implanted species was not observed in the previous luminescence studies of implant defects.

12. The FE spectra from the substrate taken at the same temperature can be subtracted from the combined luminescence to yield only the dopant associated luminescence. This new technique should prove to be useful to study other implants in Si.

13. Leakage currents, which may have a significant effect on electrical measurements, are produced when a p-n junction is used to isolate the implanted layer from the substrate. However, the leakage current can be monitored during Hall-effect and resistivity measurements via a contact to the substrate in order to determine the validity of the measurements. Data was used quantitatively in this study only if the leakage current was less than 1% of the measurement current. Also, the  $R_a/R_b$  ratio needs to be monitored to insure that it remains constant with temperature.

14. The ionization energy of dopants can be determined for implant layers by temperature dependent Hall-effect measurements in the compensated temperature region even though the acceptor concentration varies with depth. The ionization energy can also be determined from temperature dependent sheet conductivity measurements in the compensated temperature region.

SECTION VII  
RECOMMENDATIONS

1. IMPLANTED SI:Tl

Si:Tl remains a very viable candidate for an infrared charge-coupled array detector material as the results of this study indicate. It is a slow diffuser in Si and has a high sensitivity in the 3-5 micron spectral range with a high temperature background limited performance. These characteristics are unmatched by any other known dopant in Si. For this reason further research should be conducted on Si:Tl.

The Si:Tl implants should be studied by photoconductivity and the detectivity for an implant layer determined. A  $10^{14}$  Tl/cm<sup>2</sup> implant at over 500 keV into 100 ohm-cm n-type Si would be a good choice for this study. The p-n junction should be reverse-biased and the leakage current monitored during measurements as described for the Hall-effect measurements in this study. Further RBS studies should investigate the effects of flux peaking in Si:Tl and determine the substitutional component for deep implants accurately. The early RBS results for shallow implants should be repeated for deep implants to see if Tl is indeed 80% substitutional for low dose implants.

Novel techniques should be explored to produce thick enough layers by implanting for use as an operational detector. The state-of-the-art bulk grown Si:Tl sample contain large amounts of Sn, B, and donors. These impurities may lower the operational temperature, decrease the mobility, and affect the long wave characteristics of the spectral response. High energy channeled implants coupled with in situ laser annealing during the implantation is one possibility. Also, multiple layers of Si might be grown epitaxially with each successive layer implanted and annealed.

## 2. IMPLANT TECHNIQUES

The luminescence and Hall-effect techniques developed in this study have important potential for studying implants in Si. Luminescence allows the monitoring of the defects introduced by implantation following each anneal step through to the final doped material. This is particularly important for detectors produced by implantation since the defects will adversely affect the photoconductive properties. Luminescence will also be invaluable in studying laser annealing of implants since laser irradiation introduces defects itself. With luminescence, the defect levels and optical activation could be monitored in situ after each laser annealing pulse. The luminescence technique for implant layers can be improved by using a nitrogen or ultraviolet laser, or a low energy, high current electron beam for excitation which would be absorbed in a thinner surface layer resulting in less interfering FE luminescence from the substrate. Luminescence of implant layers is complemented by temperature dependent Hall-effect measurements.

The ionization energy can be determined for implant layers by temperature dependent Hall-effect measurements in the compensated temperature range providing an easier alternative to tedious and error prone differential Hall-effect measurements. This technique is very important for dopants such as Tl which are not easily introduced by bulk doping or diffusion. Also, room temperature measurements should not be used to evaluate implants, such as in laser anneal studies, unless the temperature dependence of the carrier concentration has been determined.

## REFERENCES

1. N. Sclar, Materials for MOSIS FLIR Phase I, Final Technical under Contract DAAG53-76-C-0208, August 1977.
2. C. S. Fuller and J. A. Ditzenberger, J. Appl. Phys. 27, 544 (1956).
3. J. H. Nevin and H. T. Henderson, J. Appl. Phys. 46, 2130 (1975).
4. M. A. Vouk and E. C. Lightowers, J. Lumin. 15, 357 (1977).
5. Walter Scott and J. L. Schmitt, Appl. Phys. Lett. 33, 294 (1978).
6. R. G. Shulman, J. Phys. Chem. Solids 2, 115 (1957).
7. N. Sclar, Infrared Phys. 16, 435 (1976).
8. James W. Mayer, Lennart Eriksson, and John A. Davies, Ion Implantation in Semiconductors, Silicon and Germanium, (Academic Press, New York, 1970).
9. James F. Gibbons, Proc. IEEE 56, 295 (1968).
10. G. Carter and W. A. Grant, Ion Implantation of Semiconductors, (Edward Arnold, London, 1976).
11. James Karsten Hirvonen, Ph.D. thesis, Rutgers University, 1971.
12. Bernard Smith, Ion Implantation Range Data for Silicon and Germanium Device Technologies, (Research Studies Press Inc., Forest Grove, OR, 1977).
13. Conilee G. Kirkpatrick, Ph.D. thesis, University of Illinois, 1974.
14. S. S. Lau, J. W. Mayer, and W. F. Tseng, in Proceedings of the 1978 Laser-Solid Interactions and Laser Processing Conference, edited by S. D. Ferris, H. J. Leamy, and J. M. Poate, (American Institute of Physics, New York, (1979).
15. P. Blood, W. L. Brown, and G. L. Miller, J. Appl. Phys. 50, 173 (1979).
16. B. C. Dobbs, P. M. Hemenger, and S. R. Smith, J. Electron. Materials 6, 705 (1977).
17. D. E. Schafer, Thallium-Doped Silicon IR Detector Material, Materials Laboratory, Wright-Patterson AFB, Ohio 45433, May 1981.
18. Hall Effect Results Furnished by P. M. Hemenger of the Materials Laboratory, AFWAL, WPAFB, OH.
19. P. Boolchand and P. Hemenger, to be published.

## REFERENCES (Cont'd)

20. J. R. Haynes and W. C. Westphal, Phys. Rev. 101, 1676 (1956).
21. J. R. Haynes, Phys. Rev. 4, 361 (1960).
22. Ya. E. Pokrovskii and K. I. Svistunova, Sov. Phys. Solid State 5, 1373 (1964); 6, 13 (1964); 7, 1478 (1965).
23. P. J. Dean, J. R. Haynes, and W. F. Flood, Phys. Rev. 161, 711 (1967).
24. M. L. W. Thewalt, G. Kirczenow, R. L. Parsons, and R. Barrie, Can. J. Phys. 54, 1728 (1976).
25. M. L. W. Thewalt, Phys. Rev. Lett. 38, 521 (1977).
26. E. C. Lightowers and M. O. Henry, J. Phys. C 10, L247 (1977).
27. M. A. Vouk and E. C. Lightowers, in Proceedings of the Thirteenth International Conference on the Physics of Semiconductors, edited by F. G. Fumi (Rome, 1976) pp. 1098-1101.
28. S. A. Lyon, D. L. Smith, and T. C. McGill, Phys. Rev. B, 17 2620 (1978).
29. R. Sauer, W. Schmid, and J. Weber, Solid State Commun. 27, 705 (1978).
30. G. S. Mitchard, S. A. Lyon, K. R. Elliott, and T. C. McGill, Solid State Commun. 29, 425 (1979).
31. K. R. Elliott, S. A. Lyon, D. L. Smith, and T. C. McGill, Phys. Lett. 70A, 52 (1979).
32. J. Weber, W. Schmid, and R. Sauer, J. Lumin. 18/19, 93 (1979).
33. K. R. Elliott, D. L. Smith, and T. C. McGill, Solid State Commun. 27, 317 (1978).
34. J. R. Noonan, C. G. Kirkpatrick, and B. G. Streetman, Radiat. Eff. 21, 225 (1974).
35. A. V. Mudryi and A. V. Yukhevich, Sov. Phys. Semicond. 8, 875 (1975).
36. C. G. Kirkpatrick, J. R. Noonan, and B. G. Streetman, Radiat. Eff. 30, 97 (1976).
37. D. R. Myers and B. G. Streetman, Solid State Commun. 18, 815 (1976).

## REFERENCES (Cont'd)

38. C. G. Kirkpatrick, D. R. Myers, and B. G. Streetman, *Radiat. Eff.* 31, 175 (1977).
39. J. I. Pankove and C. P. Wu, *Appl. Phys. Lett.* 35, 937 (1979).
40. R. A. Street, N. M. Johnson, and J. F. Gibbons, *J. Appl. Phys.* 50, 8201 (1979).
41. V. D. Tkachev, C. Schrodell, and A. V. Mudryi, *Radiat. Eff.* 49, 133 (1980).
42. Hisao Nakashima, Yasuhiro Shiraki, and Masanobu Miyao, *J. Appl. Phys.* 50, 5966 (1979).
43. M. A. Vouk and E. C. Lightowers, *J. Phys. C* 10, 3689 (1977).
44. Jacques I. Pankove, *Optical Processes in Semiconductors*, (Dover, New York, 1971).
45. P. J. Dean, in *Applied Solid State Science*, edited by Raymond Wolfe, (Academic Press, New York, 1969), Vol. 1, pp. 1-151.
46. R. B. Hammond, T. C. McGill, J. W. Mayer, *Phys. Rev. B* 13, 3566 (1976).
47. M. A. Lampert, *Phys. Rev. Lett.* 1, 450 (1958).
48. P. J. Dean, in *Luminescence of Inorganic Solids*, edited by Paul Goldberg (Academic Press, New York, 1966), pp. 119-203.
49. M. L. W. Thewalt, U. O. Ziemelis, and R. R. Parsons, *Phys. Rev. B* 24, 3655 (1981).
50. Paul Voisin, Bernard Etienne, and Michel Voos, *Phys. Rev. B* 22, 1117 (1980).
51. Robert J. Spry and W. Dale Compton, *Phys. Rev.* 175, 1010 (1968).
52. M. L. W. Thewalt, *Can. J. Phys.* 55, 1463 (1977).
53. N. O. Folland, *Phys. Rev. B* 1, 1648 (1970).
54. K. Kasai and M. Gershenzon, *Phys. Rev. B* 9, 723 (1974).
55. M. O. Henry and E. C. Lightowers, *J. Phys. C* 11, L555 (1978).
56. Y. C. Chang and T. C. McGill, *Phys. Rev. Lett.* 45, 471 (1980).
57. David H. Brown and S. R. Smith, *J. Lumin.* 21, 329 (1980).

## REFERENCES (Cont'd)

58. R. W. Martin and R. Sauer, *Phys. Status Solidi B* 62, 443 (1974).
59. A. S. Kaminskii, Ya. E. Pokrovskii, and N. V. Alkeev, *Sov. Phys. JETP* 32, 1048 (1971).
60. L. J. van der Pauw, *Philips Res. Rep.*, 13, 1 (1958).
61. P. M. Hemenger, *Rev. Sci. Instrum.* 44, 698 (1973).
62. T. M. Baleshta and J. D. Keys, *Am. J. Phys.* 36, 23 (1968).
63. K. Seeger, *Semiconductor Physics* (Spring-Verlag, New York, 1973), p. 69.
64. R. F. Webber, R. S. Thorn, and L. N. Large, *Int. J. Electronics* 26, 163 (1969).
65. C. Wagner and F. Burkhardt, *Phys. Status Solidi A* 47, 131 (1978).
66. Patrick M. Hemenger, private communication.
67. A. C. Beer, in *Solid State Physics*, edited by F. Seitz and D. Turnbull, (Academic Press, New York, 1963), Suppl. 4.
68. N. G. E. Johansson, J. W. Mayer, and O. J. Marsh, *Solid-State Electron.* 13, 317 (1970).
69. Richard L. Petritz, *Phys. Rev.* 110, 1254 (1958).
70. P. Blood and J. W. Orton, *Rep. Prog. Phys.* 41, 11 (1978).
71. David Richard Meyers, Ph.D. thesis, University of Illinois, 1974.
72. A. E. Michel, F. F. Fang, and E. S. Pan, *J. Appl. Phys.* 45, 2991 (1974).
73. P. Kramer and L. J. van Ruyven, *Solid-State Electron.* 20, 1011 (1977).
74. John P. McKelvey, *Solid State and Semiconductor Physics*, (Harper and Row, New York, 1966).
75. Richard D. Pashley, Ph.D. thesis, California Institute of Technology, 1974.
76. E. H. Putley, *The Hall Effect in Semiconductor Physics*, (Dover, New York, 1968).
77. J. S. Blakemore, *Semiconductor Statistics*, (Pergamon Press, New York, 1962).

## REFERENCES (Cont'd)

78. F. L. Madarasz, J. E. Lang, and P. M. Hemenger, *J. Appl. Phys.* 52, 4646 (1981).
79. R. Baron, G. A. Shifrin, O. J. Marsh, and J. W. Mayer, *J. Appl. Phys.* 40, 3702 (1969).
80. S. D. Brotherton and A. Gill, *Appl. Phys. Lett.* 33, 953 (1978).
81. T. E. Seidel and A. U. MacRae, *Trans. Metall. Soc. AIME* 245, 491 (1969).
82. D. I. Tetel'baum, *Sov. Phys. Semiconc.* 1, 593 (1967).
83. W. M. Gibson, F. W. Martin, R. Stensgaard, F. Palmgren-Jensen, N. I. Meyer, G. Galster, A. Johansen, and J. S. Olsen, *Can. J. Phys.* 46, 675 (1968).
84. E. I. Zorin, P. V. Pavlov, and D. I. Tetel'baum, *Sov. Phys. Semicond.* 2, 111 (1968).
85. E. I. Zorin, P. V. Pavlov, D. I. Tetel'baum, and A. F. Khokhlov, *Sov. Phys. Semicond.* 6, 344 (1972).
86. A. V. Zastavnyi, V. M. Korol, A. N. Mikhaleva, and V. D. Prozorovskii, *Sov. Phys. Semicond.* 13, 580 (1979).
87. C. MacDonald and G. Galster, in *Ion Implantation*, edited by Fred H. Eisen and Lewis T. Chadderton, (Gordon and Breach, New York, 1971), pp. 173-185).
88. A. H. Clark and K. E. Manchester, *Trans. Metall. Soc. AIME* 242, 1173 (1968).
89. T. E. Seidel and A. U. MacRae, in *Ion Implantation*, edited by Fred H. Eisen and Lewis T. Chadderton, (Gordon and Breach, New York, 1971), pp. 149-154.
90. W. Stumpfi and S. Kalbitzer, in *Ion Implantation*, edited by Fred H. Eisen and Lewis T. Chadderton, (Gordon and Breach, New York, 1971), pp. 155-160.
91. K. V. Anand, M. I. Sobhy, A. H. G. El-Dhaher, *Int. J. Electron.* 40, 169 (1976).
92. N. G. E. Johansson and J. W. Mayer, *Solid-State Electron.* 13, 123 (1970).
93. P. Bergamini, G. Fabri, and F. Pandarese, *Appl. Phys. Lett.* 17, 18 (1970).

## REFERENCES (Cont'd)

94. J. M. Shannon, R. A. Ford, and G. A. Gard, in Ion Implantation, edited by Fred H. Eisen and Lewis T. Chadderton, (Gordon and Breach, New York, 1971), op. 167-171.
95. J. Suski, J. Krynicki, H. Rzewuski, and J. Gyulai, Radiat. Eff. **30**, 125 (1976).
96. M. Takai, P. H. Tsien, S. C. Tsou, D. Roschenthaler, M. Ramin, H. Rysse, and I. Ruge, Appl. Phys. **22**, 129 (1980).
97. J. Gyulai, O. Meyer, R. D. Pashley, and J. W. Mayer, in Ion Implantation, edited by Fred H. Eisen and Lewis T. Chadderton, (Gordon and Breach, New York, 1971), pp. 297-304.
98. R. Bader and S. Kalbitzer, in Ion Implantation, edited by Fred H. Eisen and Lewis T. Chadderton, (Gordon and Breach, New York, 1971), pp. 161-166.
99. M. Y. Tsai and B. G. Streetman, J. Appl. Phys. **50**, 183 (1979).
100. M. Y. Tsai, B. G. Streetman, V. R. Deline, and C. A. Evans, Jr., J. Electron. Mater. **8**, 111 (1979).
101. P. D. Goode, M. A. Wilkins, and G. Dearnaley, in Ion Implantation, edited by Fred H. Eisen and Lewis T. Chadderton, (Gordon and Breach, New York, 1971), pp. 187-195.
102. A. V. Dvurechensky, N. N. Gerasimenko, S. I. Romanov, and L. S. Smirnov, Radiat. Eff. **30**, 69 (1976).
103. T. Inada, T. Sugiyama, N. Okano, and Y. Ishikawa, Electron. Lett. **16**, 54 (1980).
104. D. K. Sadana, M. Strathman, J. Washburn, C. W. Mager, M. Maenpau, and G. R. Booker, Appl. Phys. Lett. **37**, 615 (1980).
105. A. Lietoila, J. F. Gibbons, T. J. Magee, T. Peng, and J. D. Hong, Appl. Phys. Lett. **35**, 532 (1979).
106. P. H. Tsien, H. Rysse, D. Roschenthaler, and I. Ruge, J. Appl. Phys. **52**, 4775 (1981).
107. AFWAL/MLPO computer program.
108. Philip R. Bevington, Data Reduction and Error Analysis for the Physical Sciences, (McGraw-Hill, New York, 1969).
109. Patrick M. Hemenger, Gallium Diffusion in Silicon Dioxide, Rutherford Backscattering Analysis of Thin Films, Materials Laboratory, Wright-Patterson AFB, Ohio, AFML-TR-75-55, May 1976.

## REFERENCES (Concluded)

110. Wei-Kan Chu, James W. Mayer, and Marc-A. Nicolet, Backscattering Spectrometry, (Academic Press, New York, 1978).
111. L. Eriksson, J. A. Davies, N. G. E. Jonansson, and J. W. Mayer, *J. Appl. Phys.* 40, 342 (1969).
112. J. A. Davies, L. Eriksson, and J. W. Mayer, *APPL. Phys. Lett.* 12, 255 (1968).
113. L. Eriksson, G. Fladda, and K. Bjorkqvist, *Appl. Phys. Lett.* 14, 195 (1969).
114. L. Eriksson, G. R. Bellavance, and J. A. Davies, *Radiat. Eff.* 1, 71 (1969).
115. G. Fladda, P. Mazzoldi, E. Rimini, D. Sigurd, and L. Eriksson, *Radiat. Eff.* 1, 249 (1969).
116. B. Domeij, G. Fladda, and N. G. E. Jonansson, *Radiat. Eff.* 5, 155 (1970).
117. I. Bergstrom, K. Bjorkqvist, G. Bjarnolt, B. Domeij, L. Eriksson, G. Fladda, N. G. E. Johansson, and D. Sigurd, Research on Ion Implantation in Semiconductors, AFAL-TR-70-186, Avionics Laboratory, Wright-Patterson AFB, Ohio 45433, June 1970.
118. C. E. Christodoulides, Purity and Stoichiometry of Optical Coatings and Indium Implantation of Silicon, AFOSR-77-3197, January 1978.
119. J. A. McHugn, in Secondary Ion Mass Spectrometry, edited by K. F. J. Heinrich and D. E. Newbury, (NBS Special Publication 427, 1975).

**MEL**  
**8**